2015-04-06

Mechanisms of central axon and myelin injury using advanced morphological and biochemical characterization

Teo, Wulin

UNIVERSITY OF CALGARY

Mechanisms of Central Axon and Myelin Injury Using Advanced Morphological and Biochemical Characterization

by

Wulin Teo

A THESIS

SUBMITTED TO THE FACULTY OF GRADUATE STUDIES

IN PARTIAL FULFILMENT OF THE REQUIREMENTS FOR THE

DEGREE OF DOCTOR OF PHILOSOPHY

GRADUATE PROGRAM IN NEUROSCIENCE

CALGARY, ALBERTA

MARCH, 2015

Abstract

In the adult nervous system, white matter connecting brain, spinal, and peripheral regions is essential for neuron communication. In the white matter, the axon plays an essential role in transmitting nerve impulses, while myelin facilitates conduction through rapid propagation and optimal energy-consumption. White matter injury in the central nervous system, leading to the degeneration of axons and myelin, is commonly found in multiple sclerosis, anoxia, ischemic stroke, and traumatic brain and spinal cord injury. These lead to cognitive impairment, sensori-motor disability or death. During white matter injury, axonal spheroid formation (ASF) and demyelination are the pathological hallmarks of white matter degeneration. However, the mechanism by which this occurs is unknown. I hypothesize that focal spheroids are induced by activation of glutamate receptors and lead to local calcium overload in axons. To test this hypothesis, I established an *ex vivo* imaging model of central white matter dorsal column using two-photon microscopy to investigate this phenomenon. *Ex vivo* imaging of the white matter dorsal column with high-spatial resolution was achieved, which allowed the observation of morphology of axon and myelin before and during injury. The dynamic imaging of live myelinated axon response to injury suggests that axons and myelin are not as passive as previously thought. The data presented in this thesis support the notion of over-activation of glutamate receptors inducing ASF and a calcium rise leading to axonal transection. In addition, I established a novel method using solvatochromic dyes to investigate the biochemical property of myelin in which changes in the lipid composition served as a health indicator of myelin. The study of live myelin with solvatochromic dyes to stain myelin lipids could report different stages ranging from development, maturity, injury, and repair of myelin.

Acknowledgements

First and foremost, I would like to thank my supervisor Dr. Peter Stys who has offered invaluable and constructive advice, and guidance to make this Ph.D. study and dissertation come to fruition. He is extremely supportive and patient, and for that I am truly grateful.

Thank you to my supervisory committee, Drs. V. Wee Yong and Minh Dang Nguyen for their guidance over the course of my Ph.D. Special thanks go to Drs. Gerald Zamponi and Michael Colicos for participating in my candidacy exam. I also thank Drs. Shalina Ousman and Naweed Syed for giving me advice throughout the years.

I would like to express my appreciation towards Karen Cummins, Craig Brideau, Drs. Ileana Micu, Tak-ho Chu, Li Lu, Hugo Tedford, Joe Sparling and Jason Plemel for providing expertise and advice in various areas of my research. I also thank the people in my lab for their kind support.

I also thank my closest friends, especially Dr. Sompong Vongpunsawad, for being there every time I need his advice and Dr. Nicole Welch for providing valuable input on thesis writing.

Lastly, I would like to thank my family and siblings who always supported me in all my pursuits. Finally, I am forever appreciative of my loving wife, who has been exceptionally patient, supportive and encouraging throughout my studies, and my sons who kept me smiling during tough times in the Ph.D. pursuit.

Dedication

To my late mother Lee Lay Eng.

Her words of inspiration and encouragement guided me throughout my life.

To my late sisters Yoke Shien and Yoke Feng.

They inspired me to stay focused on getting goals accomplished while maintaining positive spirit.

Table of Contents

List of Tables

List of Figures and Illustrations

List of Symbols, Abbreviations and Nomenclature

Symbol	Definition
aCSF	Artificial cerebrospinal fluid
ASF	Axonal spheroid formation
AR	Axoplasmic reticulum
ATP	Adenosine triphosphate
βAP	Beta amyloid protein
Ca^{2+}	Calcium ion
CARS	Coherent anti-Stokes Raman scattering
CNS	Central nervous system
CFP	Cyan fluorescent protein
CW	Continuous wave
DAWM	Diffusely-abnormal/Dirty-appearing white matter
DMSO	Dimethyl sulfoxide
EDTA	Ethylenediaminetetraacetic acid
EGTA	Ethylene glycol tetraacetic acid
EM	Electron microscopy
ER	Endoplasmic reticulum
FRET	Förster resonance energy transfer
GFP	Green fluorescent protein
GP	Generalized polarization
HPLC	High-performance liquid chromatography

Symbol	Definition
IR	Infrared
KA	Kynurenic acid
LPC	Lysophosphatidyl choline
MS	Multiple sclerosis
Na^+	Sodium ion
NaN_3	Sodium azide
NR	Nile red
NRSSA	Nile red solvatochromic shift assay
NAWM	Normal-appearing white matter
OGD	Oxygen-glucose deprivation
PBS	Phosphate buffered saline
PFA	Paraformaldehyde
PNS	Peripheral nervous system
PPMS	Primary progressive multiple sclerosis
PLP	Proteolipid protein
RRMS	Relapsing-remitting multiple sclerosis
SHG	Second harmonic generation
ROS	Reactive oxygen species
SLI	Schmidt-Lanterman incisures
SPMS	Secondary progressive multiple sclerosis

Symbol	Definition
TBOA	Threo-beta-benzyloxyaspartate
TLC	Thin-layer chromatography
Wlds	Wallerian degeneration slow
YFP	Yellow fluorescent protein

Chapter One: Summary

In the adult central nervous system (CNS), axons of neurons and myelinating oligodendrocytes intimately contact one another and play a pivotal role in connecting neural pathways and transmitting information via saltatory conduction- fast nerve impulses conducted with high fidelity and reliability. Despite its special role as a conducting unit, the central myelinated axon is highly vulnerable to energy deprivation injury such as ischemia and hypoxia. Indeed, its unusual long and slender structure intimately wrapped by myelin sheaths and high energy demands for electrochemical activities render it susceptible to the irreversible effect of immune responses[1,2], energy deprivation[3–5], virus infections[6,7]. Accordingly, it is thought that loss of axons is a key predictor of clinical disability[8]. Hence, slow conduction velocity or conduction failure resulting from myelin breakdown and/or axonal loss are the common denominator of a number of different white matter disease processes in the CNS and the determinant of irreversible neurological disability in most patients. Examples include multiple sclerosis (MS)[9], ischemic[10] and traumatic brain injury[11], and spinal cord injury[12].

Axonal spheroid formation is a hallmark of many white matter disorders in human. The axonal swellings often lead to axonal transection, culminating in irreversible clinical disability. Previous studies have shown that white matter injury triggered by glutamate-mediated excitotoxicity pathways and followed by internal calcium rise in axons results in impaired conduction in isolated dorsal column[13]. Thus, I set out to explore the mechanism of axonal spheroid formation (ASF). I started by 1) Developing *ex vivo* model for the study of ASF; 2) Investigating ASF via energy deprivation; 3) Exploring glutamate-mediated excitotoxicity injury model and calcium imaging using förster resonance energy transfer (FRET) transgenic mice; 4) Characterizing the

morphology of axonal spheroids; 5) Studying biochemical pathology of myelin and introducing a completely new technique based on solvatochromism of fluorescent probes to investigate the biochemistry of pathological myelin.

In summary, this thesis explores mechanisms of how abnormal morphological changes are induced in axons and myelin. For the morphological study, ASF and transection are key events, indeed possibly the most important phenomenon that occurs in white matter injury due to the irreversible transection leading to clinical disability in human. For the biochemical study, change of lipid composition in myelin might signal early signs of myelin breakdown. Therefore, by understanding the molecular mechanisms of spheroid formation and biochemical changes in abnormal myelin, we may better prevent this phenomenon, and hopefully by extension, arrest the progression to transection and irreversible nerve fiber degeneration in the CNS.

1.1 Hypothesis

Axon spheroid formation/transection, the cardinal feature of irreversible white matter pathology, is driven by glutamate-mediated excitotoxicity and local dysregulation of calcium homeostasis. This leads to focal structural changes in axons and lipid biochemical changes in myelin that can be detected using novel spectroscopic techniques based on solvatochromic fluorescent probe.

1.2 Specific aims

1.2.1 To develop an ex vivo system for high-resolution imaging in dorsal column

Fine imaging of live adult CNS axons is the key to understanding how and where axonal spheroids form. The first aim is to develop a live imaging system to allow stabilization of axons with high spatial resolution while preserving their physiological integrity.

1.2.1.1 Sub-aim: to demonstrate high-resolution imaging of live myelinated axons, glial cells and subcellular mitochondria

This aim is to demonstrate the capability of high-resolution imaging.

1.2.1.2 Sub-aim: to label myelin via genetic vs. exogenous probes

I use two approaches: transgenic mice expressing green fluorescent protein in myelin via proteolipid protein promoter and myelin labeling with lipophilic fluorescent dyes.

1.2.2 Axon pathology

My second aim is to study the progression of ASF and transection via glutamate-mediated excitotoxicity and calcium imaging in focal spheroids.

1.2.2.1 To study energy deprivation-mediated ASF

The Stys lab has been studying energy deprivation-mediated injury mechanisms for many years. Hence, I will apply this injury mechanism as positive control group for the study of ASF.

1.2.2.2 To measure axonal calcium using transgenic mice expressing FRET

Previously, our lab and others have shown the impact on axonal function and calcium activity induced by glutamate. I asked whether the downstream effect of such injury could lead to ASF, the ubiquitous pathology known to occur in many white matter disorders. I investigated the effect of glutamate-mediated excitotoxicity in adult mouse central white matter. Next, I aimed to study calcium-mediated axonal injury using transgenic mice expressing a calcium sensor-FRET reporter in axons.

1.2.2.3 To analyze morphology of axonal spheroid

Fluorescent protein expression has been widely used to tag specific cells in transgenic animals. I investigated fluorescent-tagged axons as a mean to study axonal morphology.

1.2.3 Myelin pathology

1.2.3.1 Sub-aim: to perform biochemical imaging using solvatochromism

I investigated changes of lipid composition with the solvatochromic dye Nile red.

1.2.3.2 Sub-aim: to validate quantitative and qualitative assay

I introduced a new quantitative method of study solvatochromic shift.

1.2.3.3 Sub-aim: to induce demyelination and remyelination via LPC agents

I applied this demyelinating agent on dorsal column and imaged the structure of myelin.

Chapter Two: Introduction to white matter and injury

2.1 Definition

The central nervous system (CNS) of vertebrates consists of the white and grey matter, originally defined by the colors of the tissues examined by the naked eye. The whitish appearance of the lipid-rich myelin contrasts with the grayish dense neuronal cell bodies. Specifically, the CNS white matter consists of two major cellular processes: axons of neurons and myelin of oligodendrocytes. The interaction between myelinating glia and axons results in myelination of the axon tracts, which fundamentally affects how nerve impulses propagate, supporting saltatory conduction[14]. Saltatory conduction may have been selected for in response to predation pressure during evolution[15]. Rapid, reliable and energy efficient saltatory conduction allows a new kind of survival behavior with the rapid coordination of sensory inputs, cognitive processes, and motor responses.

The exact mechanisms of axon and myelin interaction resulting in myelination are still elusive, but axon and myelin both play a role in distribution and registration of specific ion channels and adhesion molecules into specific membrane domains[16]. During myelination, the axon is successively covered by the myelin sheaths from different oligodendrocytes at different internodes, and conversely each oligodendrocyte can myelinate up to forty axons in optic nerve of the rat[17]. Each myelinated segment forms four domains including the node of Ranvier, paranode, juxtaparanode and internode.

Evidence using immunohistochemistry has shown that voltage gated sodium channels (Na_V 1.6) are mainly expressed at nodes of Ranvier, the region completely devoid of myelin in the CNS.

Perinodal astrocytes extend their processes to make contact with the axon at the nodal region. Next to the unmyelinated node is the paranodal region, where the lateral loops of myelin make contact with the axonal membrane. The lateral loops are not compacted like compact internodal myelin, and are rich in cytoplasmic organelles. Data from electron microscopy (EM) shows that the contact segments by each lateral loops indent the paranodal axolemma and form septate-like junctions. No voltage gated channels are found in this region, instead only adhesion molecules such as junction NF155 (neurofascin 155) that bind to axonal contactin-associated protein. Next to the paranodal region, the juxtaparanode is occupied by voltage gated potassium channels (K_v 1.1 and 1.2)[18]. The function of the paranodal region was shown in transgenic mice with the knockout of NF155. Impaired paranodal regions break the barrier to allow redistribution of potassium channels across to paranodal region[19]. Finally, the region which typically comprises more than 99% of total myelinated axon is called the internodal region[20].

The internodal region is traditionally considered the unspecialized segment of myelinated axons. However, unique spiral structures are found within the internodal myelin of the CNS[21] and peripheral nervous system (PNS)[22], called Schmidt-Lanterman incisures (SLI). It is still unclear whether the SLI in the CNS shares any similarity to the PNS since the presence of SLI in the PNS requires that Schwann cells express P_0 structural proteins in compact myelin[23]. The internodal region has the largest contact area for axon and myelin. Myelination in this area is often the target of immune cells, well exemplified in MS. Demyelinated axons are then left exposed to the extracellular environment with lack of nutrition support from myelin which then results in axonal loss[24,25]. Our understanding of such dynamic changes in the local environment

of axons is limited by a lack of tools for detailed cellular imaging in living white matter. Hence, I developed novel tools to track axon and myelin injury.

2.2 Axonal pathology

One of the pathological hallmarks of axonal pathology is axonal spheroid formation (ASF)[26]. The history of observing axon spheroid can be traced back 150 years when Waller found swelling nerve fibers in injured frog leg in the PNS[27]. Later, this phenomenon was also confirmed by Cajal (Figure 2-1). Axonal spheroids are thought to precede and lead to axonal transection[9,28] and result from the local breakdown of the cytoskeleton by the activation of the calcium dependent protease calpain[29]. In turn, the source of calcium responsible for calpain activation had been reported to originate from the extracellular environment[30,31]. One recent hypothesis is the overactivation of glutamate receptors, causing calcium influx. However, how the morphology of live axons responds to a calcium rise has yet to be elucidated. Glutamate is thought to be the main suspect to induce calcium rise in white matter[13,32,33], with an additional calcium source possibly originating from axonal calcium stores like axoplasmic reticulum[34]. However, the precise mechanism of ASF remains elusive. In view of the axon's morphology, its length and surface area can be as much as 20,000 times larger than the cell body[35]. Its morphology renders it vulnerable to physical, metabolic, viral or autoimmune damage that may lead to spheroid formation. In addition, axonal transection in the CNS white matter is almost impossible to regenerate. This unique vulnerability, together with the axon's critical role in signal transmission, underscores the importance of understanding fundamental mechanisms leading to irreversible injury of this critical structure.

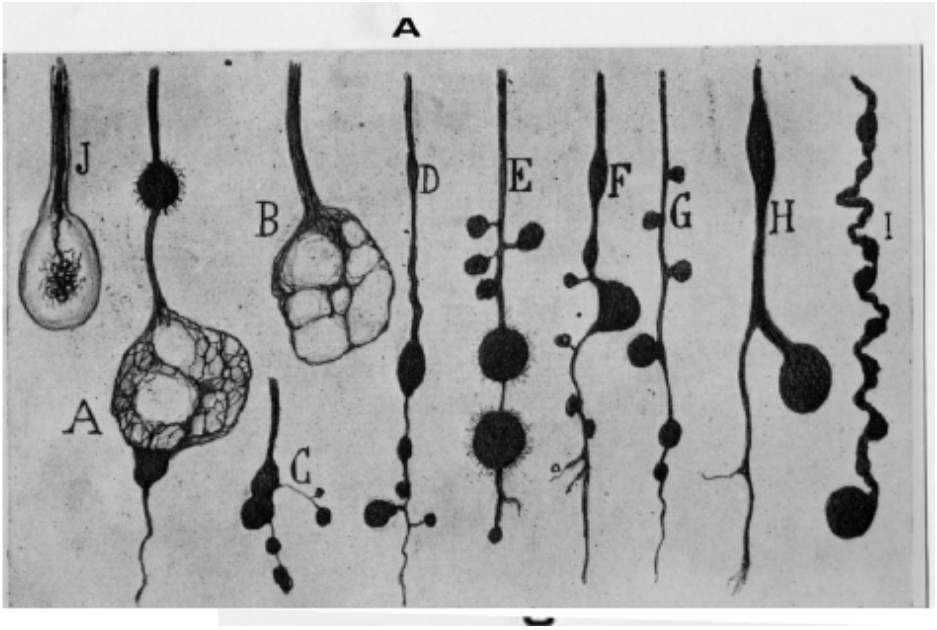

Figure 2-1. A drawing of various forms of axonal spheroid from white matter spinal cord by Santiago Ramón y Cajal, an early pathological hallmark of axonal degeneration[36]

2.3 Myelin pathology

Myelin breakdown directly results in loss of functional conductivity. The prototypical myelin pathology is seen in MS, an inflammatory demyelinating disease where myelin sheaths are attacked by immune cells leading to demyelination of the nerves, eventually forming gliosis. The myelin pathology affects sensory and motor central white matter tracts, and results in clinical disability when eloquent pathways are affected. In addition, recent studies suggest myelin breakdown can also affect cognitive ability. For example, cognitive function has been associated with the development of myelination in neocortex[37]. Conversely, in normal aging, myelin breakdown has been associated with cognitive decline[38,39], with the volume of white matter decreasing in normal aging[40], mainly caused by the alteration of myelin sheaths[41]. These observations suggest that cognitive function not only depends on the grey matter, but also is

affected by white matter pathology, in particular the myelination of axons with changes in conduction velocity, and disruption of normal timing in connecting nerve pathways. Furthermore, myelin associated abnormalities found in persons with schizophrenia using neuroimaging[42] demonstrated the link between myelin and mental illness. Taken together, these results demonstrate the important role of myelin for normal functioning of the mammalian CNS.

2.3.1 Multiple sclerosis (MS)

MS is an inflammatory demyelinating disease of the CNS[43]. The etiology of MS is unknown. It affects mainly young adults[44,45], and females exhibit a rate that is twice as high as males. The resulting human and economic losses are profound. According to the report by The World Health Organization and Multiple Sclerosis International Federation in 2008, MS afflicts 1.3 million people worldwide and Canada has one of the highest rates (133 per 100 000) of MS in the world. More importantly, MS is now considered a global neurological disease due to clinical reports from 112 countries[44]. Based on clinical diagnosis, MS patients are divided into four groups. Approximately 85% of MS patients experience relapsing-remitting MS (RRMS). RRMS is defined by repetitive pattern of acute onset and reversible neurological symptoms. During the acute onset, inflammatory response and cerebral edema[46] results in neurological deficits. Once the inflammatory response and edema resolve, neurological function often recovers. After 20 years, about 90% of patients with RRMS become secondary progressive MS (SPMS)[47]. SPMS is characterized by the absence of acute attacks[48], but starts with persistent neurological symptoms with increasing irreversible neurological disability. The third group is called primary progressive MS (PPMS). About 10% of MS patients present with PPMS is characterized by progressive neurological deficit with no relapsing-remitting stage. The last group of MS is called progressive

relapsing MS. It represents 5% of the MS population and shares a similarity with PPMS at the beginning, but patients experience acute attacks at some point after onset. Despite the fact that symptoms of RRMS can be alleviated by immunosuppressive drugs, progressive forms of MS fail to respond to this treatment[49]. In light of this, the symptoms of progressive forms of MS are independent of inflammatory response. Indeed, the progressive forms of MS have been proposed as the "true" MS[50,51]. Understanding the cause of axon pathology in MS requires detailed knowledge of the affected cells of the disease. The most commonly affected cells are neuronal axons and oligodendrocytes/myelin.

2.3.2 Ischemic stroke

White matter is highly vulnerable to energy deprivation in animals[5,52]. Lack of oxygen or diminished production of adenosine triphosphate in the brain often leads to white matter damaged by infarction in the area of small vessels. Indeed, 80% of stroke are ischemic caused by the interruption of blood flow to the brain due to a blood clot[53]. During decreased blood flow, myelinated axons are subjected to energy deprivation, and hypoxia. It has been shown by EM that myelin and axons in optic nerve are damaged with appearance of ASF and myelin swelling[30].

2.3.3 Traumatic brain injury/spinal cord injury

The annual economic impact of spinal cord injury in Canada is estimated to be $3.6 billion[54] and the main cause is motor vehicle collision due to impaired driving[55]. Traumatic brain injury is estimated to cost $7.3 billion in 2011 and more than 11000 Canadians die each year as result of TBI[56]. Acute transection and/or compression from physical impact to the spinal cord creates

huge challenges for repair and regeneration of the injured white matter tracts. The conduction of nerve impulses fails, followed by transection of myelinated axons in which a hostile environment surrounding the lesion makes it difficult to repair[57]. Furthermore, the impact of traumatic injury leads to diffuse axonal injury, a form of secondary axotomy[58] in traumatic white matter injury[59]. Axonal spheroids have been frequently found and are used to identify nondistruptive axonal injury induced by traumatic forces[59–61]. After axonal transection, the very early repair has been shown by the calcium dependence of membrane sealing[62]. Nonetheless, the transected white matter tracts lead to irreversible clinical disability.

2.3.4 Alzheimer's diseases

Alzheimer's disease is defined by the progressive deterioration of cognitive abilities such as memory, language and cognition. It was described by a German neuropathologist Alois Alzheimer in 1906. There is a clear relationship between white matter injury and cognitive impairment[63–65]. Evidence from MRI has frequently shown white matter injury in Alzheimer individuals[66]. Volume of corpus callosum and other white matter regions in the brain was found to be significantly decreased[66,67]. The exact cause remains unknown. One of the hypotheses is that, in the aged brain, there is accumulation of toxic by-product called beta amyloid protein (βAP). Thus, this leads to the accumulation of βAP and eventually damages white matter tracts[67]. One study using transgenic mice with presenilin-1 mutation found that oligodendrocytes were susceptible to βAP toxicity. βAP disrupts calcium homeostasis via the pathway of glutamate toxicity[68].

2.3.5 Schizophrenia

About 1% of the world's population develops schizophrenia[69], and 300,000 Canadians are affected[70] with an estimated $6.85 billion of economic burden in 2004[71,72]. Schizophrenia is a severe, disabling mental disorder, characterized by abnormal social behavior with lack of attachment to the physical world, with patients consistently experiencing hallucinations. Although it has been thought that dopamine receptors play a significant role in schizophrenia, recent evidence from MRI indicated that abnormalities of myelination might associate with schizophrenia[73]. Many abnormalities in myelin genes were demonstrated by DNA microarray[74].There is another study that suggests altered myelin production disrupts glutamatergic regulation found in schizophrenia[75]. Taken together, myelin integrity or subtle disruption seems to profoundly affect human behavior[42].

2.4 Current treatment for white matter injury

Diseases involving white matter injury in the CNS are usually untreatable. Firstly, it is because the process of degenerated axons is irreversible due to the inherent property of non-dividing cells. In addition, ASF leads to transection, which is an irreversible process in the CNS. Secondly, there are many axon regeneration inhibitors surrounding the area of white matter injury[76]. For example, myelin debris and the protein Nogo and MAG inhibit axonal regeneration[77]. To treat acute white matter injury such as traumatic brain injury, computed tomography scans or MRI are used to assess the brain injury[78]. Surgical interventions such as hematoma and decreasing pressure from swelling in the brain[79] are generally used to prevent further injury. For the treatment of chronic white matter injury, disease-modifying drugs like interferon beta to suppress the inflammation-mediated symptoms of white matter disease in MS

is the common practice, although this is not a cure for MS. Treatment for progressive MS is not available, although currently there are a few on-going clinical trials for progressive MS patients[80].

In summary, even though white matter injury has been reported since 1824, there is still little progress in the treatment for this condition. This might be in part due to the complexity of the mechanisms in white matter and the attention toward neurocentric rather than axo-glia perspective in CNS injury.

Chapter Three: High-resolution imaging of axo-myelinic dynamics in adult mouse dorsal column white matter: model and protocol

3.1 Abstract

This chapter provides an overall view of the morphology of live intact myelinated axons, glial cells and leptomeninges with high spatial resolution in the fasciculus gracilis of adult spinal cord explants for detailed study of pathological changes when the tissue is exposed to a variety of specific pharmacological insults. It also provides detailed protocols on the preparation and *ex vivo* imaging of the adult spinal cord explants. Understanding the morphology of axon and myelin remains a major challenge for the study of white matter injury due to the limitation in obtaining high-resolution image of cytoarchitecture of adult white matter in *in vivo* and *in vitro* imaging model. Thus, I set the goals:

1. To describe live imaging of subcellular/cellular morphological details in adult spinal white matter.
2. To use intact tissue and cellular environment that has developed and experienced normal intercellular relationships throughout the life of the animal.
3. To precisely control the extracellular environment when applying agonists, antagonists and enzymatic treatment.

For these experiments, most cellular structures were genetically tagged with fluorescent protein for subcellular/cellular specificity except myelin sheaths, in particular the compact myelin that is labeled by fluorescent lipophilic vital dyes. In summary, the high spatial resolution model is an intermediate between an *in vitro* and *in vivo* imaging platform and represents a balance between whole animal (which lacks precise control of extracellular environment) and in vitro cell culture (which lacks the cytoarchitecture of white matter). More importantly, such an *ex vivo* imaging platform is more flexible than *in vivo* imaging for obtaining high resolution of cellular morphology.

3.2 Introduction

Choosing a model to explore cellular morphological changes and molecular mechanisms of white matter injury is a crucial step for drug discovery of the diseases affecting white matter, such as multiple sclerosis (MS). In MS, axons and myelin sheaths are attacked by immune cells resulting in morphological changes of demyelination and axonal spheroid formation. There are two models to study live mammalian nerve fibers. *In vivo* imaging (Figure 3-1a) of white matter injury can be a good model[81], however many technical limitations hinder such imaging. For example, the respiratory motion in the animal results in poor imaging quality. To solve this problem, primary cell cultures of white matter isolated from an organism and maintained in artificial media that promotes their long-term survival and growth can provide higher quality images. A major disadvantage of this model is that they may not be representative of intact white matter due to the artificial environment and the lack of interaction with other cells.

A better approach is to use an *ex vivo* explant (Figure 3-1b). Intact spinal cord explants are removed from the animal, then perfused with an appropriate buffer solution to maintain physiologic integrity and function. Here, I used adult mouse cervical spinal cord explants to study the living morphology of central axons and glia in physiological and pathological conditions. This allowed for the examination of axonal spheroid formation (ASF) and myelin abnormality found in white matter injury (Figure 3-2).

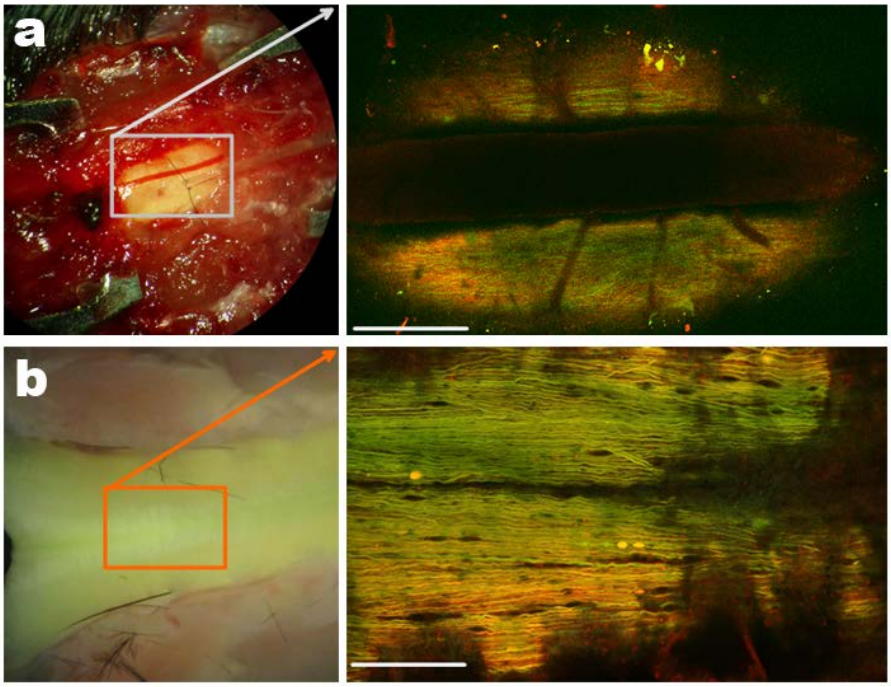

Figure 3-1. Comparison between *in vivo* and *ex vivo* imaging of transgenic mice expressing YFP in dorsal column axons

a, for *in vivo* imaging, a small portion of dorsal column was exposed by laminectomy (white rectangle) and myelin sheaths were labeled by Nile red (NR) via tail vein injection. The dorsal spinal vein staining with NR that resided at the middle of dorsal column blocked the imaging area of white matter. Image of *in vivo* imaging was obtained from Dr. Tak Ho Chu. b, for *ex vivo* imaging, dorsal column (orange rectangle) became visible using intracardiac perfusion (optical clearing technique). Scale bar = 100 μm

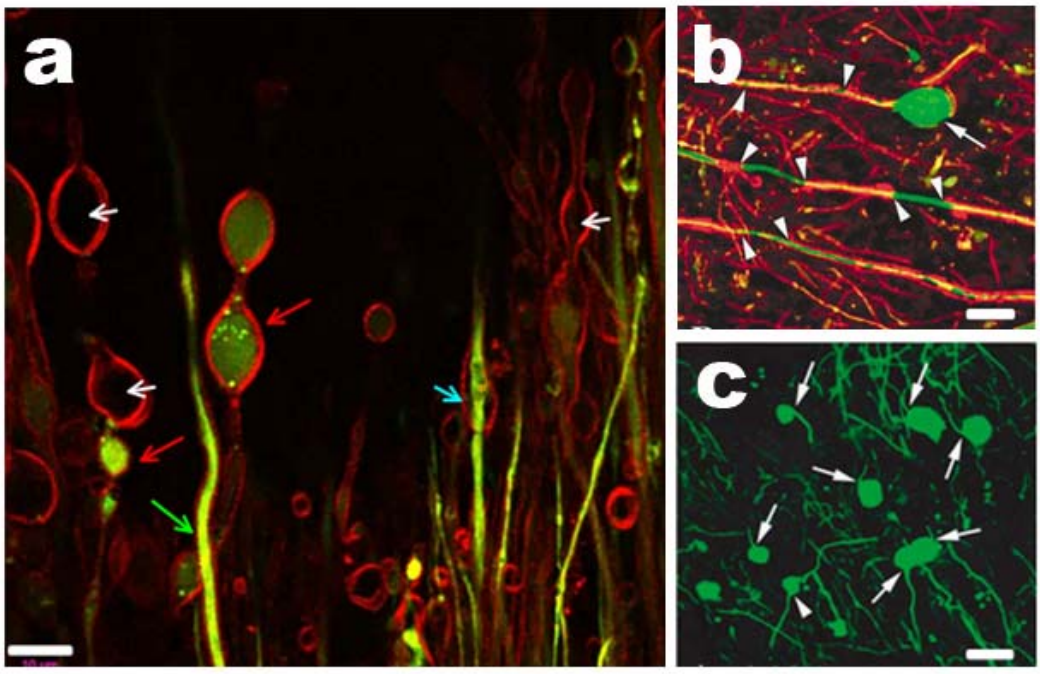

Figure 3-2. The morphological resemblance of ASF in an *ex vivo* model of white matter injury to axonal changes commonly observed in human MS lesions

a, two-photon imaging of myelinated axon abnormality in the fasciculus gracilis of adult spinal cord explant after accumulation of glutamate: (1) an injured axon (in green) formed two spheroids (red arrows) with unspecific YFP-tagged puncta inside the spheroids. (2) Next to the injured axon showed a normal-appearing axon (green arrow) with myelination (in red). (3) Another injured myelinated axon (cyan arrow) displayed myelin splitting with abnormal strucuture of axon. (4) Swellings of myelin occurred with the appearance of axon degeneration (white arrows). b and c, confocal images of myelinated axons abnormality in MS tissue. (Figures adapted from Trapp et al, 1998[9]). a, scale bar = 10 μm; b, scale bar = 65 μm; c, scale bar = 45 μm

Axons and resident glial cells are the major cell types in white matter tracts. Their relationships are highly dynamic during injury[82]. Axons are important in connecting neural pathways and transmitting nerve impulses from neurons, while glial cells (or glia, derived from Greek word meaning "glue") play important roles in providing support. In myelinating glia, oligodendrocytes are intimately associated with axons by their processes of myelin sheaths. They provide insulation, protection and nutrition for the axon[25]. Microglia, the immune cells of the central nervous system (CNS), seek and destroy pathogens, and remove dead cells[83]. Astroglia play multiple roles in maintaining homeostasis of extracellular ions[84], keeping the CNS in isolation and monitoring passages between blood and CNS activity with tight physical barrier of glia limitans[85], providing nutrition and repairing dystrophic cells[86]. Taken together, axons and glial cells form interdependent relationships based on the local environment and their cytoarchitecture. In light of this, the model of spinal cord explant is well suited for the study of axo-glial interaction and glial-glial interaction, as it strikes a compromise between an *ex vivo* preparation where pharmacological control of the extracellular environment is possible, while maintaining many of the tissue relationships that are present *in vivo*. Here I describe a protocol for cervical spinal cord explant and provide methods for high spatial resolution *ex vivo* imaging of axon and glial cells.

3.3 Experimental design

3.3.1 Imaging system

Fluorescent imaging and nonlinear optical second harmonic generation (SHG) were used. In fluorescent imaging system, two major detection methods were: two-photon excited non-descanned detection and continuous wave (CW) excitation using descanned confocal spectral

detection. In the former method, fluorescent cellular objects are excited by two-photon absorption and their fluorescent emission signals are recorded directly by photomultiplier tubes detectors without pinhole. However, if more than two emission spectra are involved and their spectra overlap, this method is not very helpful to distinguish their emission spectra. Hence, the latter method using confocal mode with 32-channel spectral detector was used to distinguish the emission spectra.

3.3.1.1 CW and two-photon laser excitation

The excitation light sources are two-photon mode-locked Ti:sapphire laser with power between 5-40 mW and CW lasers at 405 nm, 476 nm, 488 nm, 514 nm, and 561 nm. Two-photon microscopy with 2-channel nondescanned mode gives the highest signals and is the most sensitive detection method. A summary of emission spectra used in my study is illustrated in Figure 3-3. Here is the summary of excitation wavelengths for specific fluorophores:

Table 1. Summary of excitation wavelengths for imaging experiment

Cellular materials/fluorophores	Two-photon laser	CW lasers
Axon – YFP	900 – 950 nm*	405 nm, 488 nm*, 476 nm, 514 nm
Myelin – Nile red	880 – 900 nm, 750 – 800 nm*	404 nm, 488 nm, 514 nm, 561 nm*
Oligodendrocyte/myelin – GFP	870 – 950 nm	405 nm, 476 nm, 488 nm*, 514 nm
Mitochondria/CFP	850 – 880 nm	405 nm
Astrocyte/Sulforhodamine 101[87]	900 nm	404 nm, 488nm, 514 nm, 561 nm*
Astrocyte/GFP	870 – 950 nm	405 nm, 488 nm*, 476 nm, 514 nm
Microglia/GFP	870 – 950 nm	405 nm, 488 nm*, 476 nm, 514 nm
Fluorescein	780 – 850 nm	404 nm, 476 nm, 488 nm*
DAPI	750 – 780 nm	404 nm
Connective tissue/Collagen**	900 nm	

* Optimal excitation, ** label-free method (SHG)

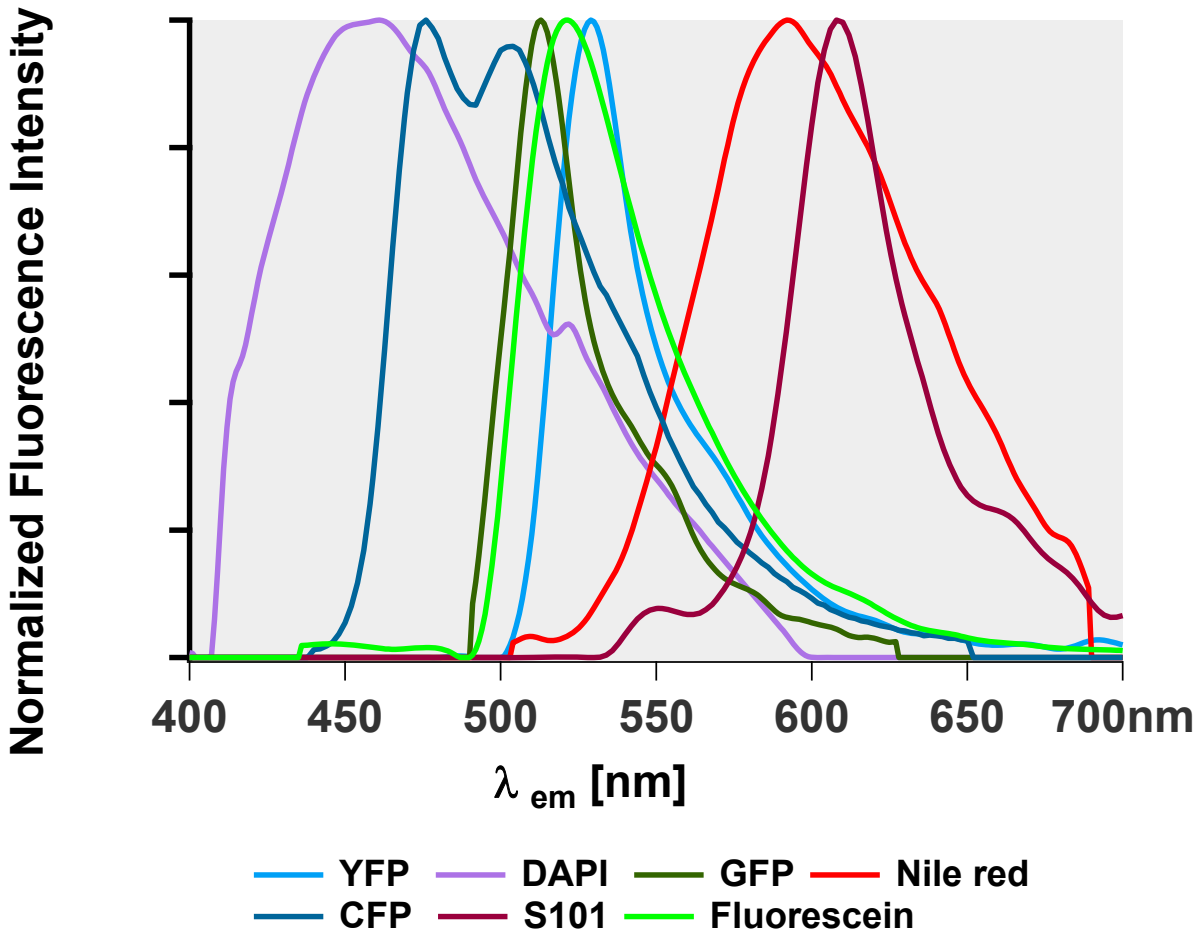

Figure 3-3. The summary of fluorescence emission spectra of various fluorophores from *ex vivo* imaging of dorsal column

After acquiring spectral images, spectral unmixing was used to separate the signals of various fluorophores based on their reference spectra. Each reference spectrum was generated based on experimental values. These reference spectra are YFP in axon, DAPI in cell body, GFP in microglia or astrocyte, NR in myelin sheath, CFP in mitochondrion, S101 in astrocyte/processes, fluorescein in dorsal column.

3.3.1.2 Spectral fluorescent imaging

I used experimental basis emission spectral profiles for linear decomposition (Figure 3-3). These basis spectra included backscattering from the exciting laser, detector noise, background and auto-fluorescent signals.

3.3.1.3 SHG

In addition to the label-dependent fluorescent imaging, label-free imaging with SHG was also applied to the study of collagen distribution in leptomeninges. The use of near IR 900 nm wavelength to interact with collagen would generate new photon half the IR wavelength at 450 nm. To confirm the specificity of SHG signals, I tuned the laser from 840 nm to 900 nm with SHG filter at 450 ± 35 nm. I then observed a clear SHG signal starting from 845 nm to 900 nm and no SHG signals below 845 nm.

3.3.1.4 Subcellular imaging

While comparing sub-cellular structures among optical imaging methods, such result should be interpreted with caution due to diffraction limit[78], although there are some interesting exceptions thanks to recent advances in optical microscopy[89,90]. In brief, any object that interacts with visible light via lenses has the limitation to resolve its true spatial resolution. This has been described as the Rayleigh criterion as shown in (1)[91].

$$d = 0.61\frac{\lambda}{\mathrm{NA}} \quad (1)$$

where d is the spatial resolution of minimum resolving distance, λ is the wavelength of emission light, NA is the numerical aperture of objective lens. It is a simple way to calculate the resolvable distance with the parameters of λ and NA. For example, an objective lens with NA 1.1 that yielded the minimum theoretical resolvable distance for cyan fluorescent protein (CFP)-tagged mitochondria (CFP emission at around 450 nm) was around 250 nm.

3.3.2 Transgenic mouse lines

All animal handling procedures were approved by the University of Calgary Animal Care Ethics Committee following the guidelines by Canadian Council on Animal Care. There were five transgenic mouse lines used to validate the system. All were adults between 1 and 3 months old. I chose B6.Cg-Tg (Thy1-YFP)16Jrs/J mice because they expressed yellow fluorescent protein YFP in most axons[91]. I received green fluorescent protein (GFP)-tagged proteolipid protein (PLP)-driven promoter expression in oligodendrocytes as a gift from Dr. Wendy Macklin[92]. I also received heterozygous Cx3cr1 GFP/+ mice from Dr. Paul Kubes to image microglia expressing GFP[93]. For imaging subcellular structure, thy1-CFP/cox8a-mito expressing CFP in mitochondria[95] and FVB/N-Tg(GFAPGFP)14Mes/J expressing GFP in astrocyte[96] were used.

3.4 Materials

3.4.1 Reagents

1. Fluorescein sodium salt (Fluka #Ra13230/Sigma 518-47-8)
2. Nile red (N-1142, Life Technologies, Inc.)

3. Transgenic mice (section 3.3.2)
4. Sodium pentobarbital (Bimeda MTC, Ontario)
5. Artificial cerebrospinal fluid (section 3.4.3.1)
6. 70% (vol/vol) ethanol solution in spray bottle
7. 4% paraformaldehyde

3.4.2 Equipment

1. Polystyrene snap cap vials 45 ml capacity (66019-108, VWR)
2. A1RMP microscope, Nikon
3. C1 microscope, Nikon
4. Objective lens heater (Bioptechs)
5. Tunable Ti:sapphire laser fs (Millennia X pumped Tsunami 3960, Spectra Physics)
6. Modelocked tunable Ti:sapphire lasers (Chameleon ultra, Coherent Inc. USA)
7. Scissors, mcpherson-vannas (WPI, USA)
8. Dissector scissors (14081-09 F.S.T, Germany)
9. Dual channel peristaltic pump (Gilson minipuls 2)
10. Temperature controller (TC-344B and TC-202A,Warner Instruments, USA)
11. Perfusion independent temperature controller (Delta T4 open dish controller)
12. Modified perfusion/imaging chamber, RC-27L large bath chamber (Harvard Apparatus)
13. SHD-27LP/2 (WI 64-0261, Warner Instruments)
14. Alligator clip
15. Control software (Nikon NIS element, EZ-C1)
16. Image analysis software (ImageTrak)

3.4.3 Reagent setup

3.4.3.1 Artificial cerebrospinal fluid (aCSF)

Once the tissue was isolated from the body, the tissue was submerged in oxy-carbonated aCSF at pH 7.5.

Table 2. The composition of physiological artificial cerebrospinal fluid

Artificial cerebrospinal fluid (aCSF)	mM
NaCl	126
KCl	3
$CaCl_2$	2
NaH_2PO_4 (sodium dihydrogen phosphate)	2
$MgSO_4$	2
$NaHCO_3$ (Sodium bicarbonate)	26
Dextrose	10

3.4.3.2 Myelin labeling

Two methods of myelin labeling by vital lipophilic Nile red (NR) were used. For short period perfusion imaging (1-6 hours), labeling myelin sheaths were achieved by 10 minutes incubation with 50 μM of NR. For imaging beyond 6 hours, 10 μM of NR was further added onto the tissue during the imaging if the signals of NR faded significantly during the perfusion.

3.4.4 Equipment setup

3.4.4.1 The perfusion system

The basic perfusion system contains three main components: 1) monitoring the temperature of the aCSF solution, 2) controlling the flow of aCSF solution with dual channel peristaltic pump system, and 3) setting up the imaging perfusion chamber. The temperature probes were built in with the perfusion system with inline heater (Figure 3-4c2) attached closely to the imaging chamber (Figure 3-4d) and constantly monitored by the controller (Figure 3-4c1). To avoid wasting expensive drugs during perfusion, I used dual-channel peristaltic pump system (Figure 3-4b) to recirculate aCSF solution (red solid line indicates inlet and blue solid line indicates outlet in Figure 3-4d). To prevent the air trap underneath the objective lens during the imaging

time, perfusate was warmed and oxy-carbonated to around 30ºC with a magnetic stirred hotplate (Figure 3-4a).

3.4.4.2 Microscopy setup

Two up-right microscopes equipped with objective heater were used in this study. Both were equipped with excitation CW lasers or pulsed lasers and long working distance water immersion objective lenses. Nikon Eclipse E800 microscope body with C1 controller (C1) mainly used in non-descanned detection with two channel detectors while Nikon A1RMP microscope (A1) used for spectral microscopy.

3.4.4.2.1 Nikon Eclipse E800 microscope body with C1 controller (C1)

C1 is a confocal laser-scanning microscope equipped with 60X 1.0 NA objective lens. It was modified to include two-photon excitation nondescanned detection mode[97]. The light source of two-photon was generated by a Ti:sapphire laser (Tsunami, Spectra-Physics Lasers). Fluorescent samples were recorded by a pair of nondescanned detector units (Hamamatsu R5959). Excitation power was monitored by a power meter (Spectra-Physics 361C). XY motorized stage was controlled by Prior ProScan II (PRIOR Scientific). For SHG imaging, the laser was tuned to 900 nm at 400 mW using an emission filter of 450 ± 35 nm.

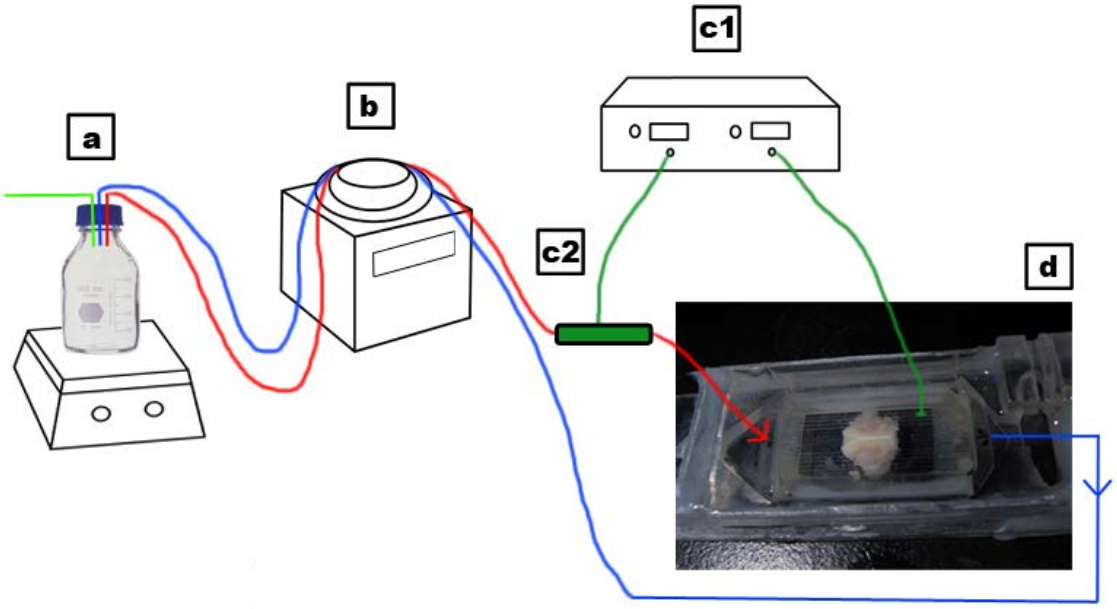

Figure 3-4. Schematic diagram of the circular perfusion system for *ex vivo* imaging of dorsal column

a, a heated magnetic stir plate was used to warm the aCSF solution to prevent air bubbles forming on the tip of the objective lens. b, dual-channel peristaltic pump for recycling the perfusate: red line indicates the inlet of aCSF solution into the imaging chamber (d) and blue line indicates the return of aCSF solution from the imaging chamber. c1, perfusion-dependent temperature controller monitors the physiological temperature of aCSF solution. c2, the inlet of heater is used to heat the aCSF solution and maintain the temperature at 35ºC.

3.4.4.2.2 Nikon A1RMP microscope (A1)

A1 laser scanning microscope was equipped with CF175 Apo 25X 1.1 NA objective lens. The laser of two-photon were generated by auto-tunable Chameleon, Coherent Inc. A1 provided three detection modes: 1) nondescanned detection with 4 channels, 2) confocal spectral detection with 32 channels.

3.4.4.3 Imaging analysis

All images were acquired using Nikon software (EZ-C1 in C1 microscope and NIS-element in A1 microscope). The images were then converted into ImageTrak format (written by PKS, http://www.ucalgary.ca/styslab/imagetrak). The software visualized images with x, y, z, t and λ dimensions and performed spectral decomposition on imaging data. For spectral decomposition, all spectral unmixing references were obtained from experimental single emission sample. In addition, I used WaveMetrics IGOR pro 6 for spectral library management, scientific graphing, programming (Appendix A) and analyzing data.

3.5 Procedure

1. Anesthetize mouse deeply and cut open the chest.

2. Perform intracardiac perfusion with cold oxy-carbonated aCSF solution for clearing out the bloods in spinal cord.

3. After 1 minute of intracardiac perfusion, flip the mouse and incise the skull between frontal and nasal area to open an access line, then make a lateral cut to open the skull.

4. Perform cervical laminectomy by cutting from atlas to T3 area of transverse process.

5. Make a cut to detach entire brain-cervical spinal cord and place it in cold oxy-carbonated aCSF solution.

6. Cut immediately after the brainstem, this end will resemble the top of the “Y” section, and then cut the other end of cervical column to have around 1-1.2 cm long of isolated cervical spine with the attached ventral connective tissue (Figure 3-5).

Before imaging the explant, adding vital dye is an optional step. 10 to 30 minutes of incubation with NR in 10-50 μM is sufficient for 3-8 hours. The duration of tissue staining with vital dye depends on the property of the dye, the tissues and the technique of laminectomy. Lastly, position the core lines on the ventral connective tissue and apply slight pressure to snap the holders onto the imaging chamber to secure the explant (Figure 3-5).

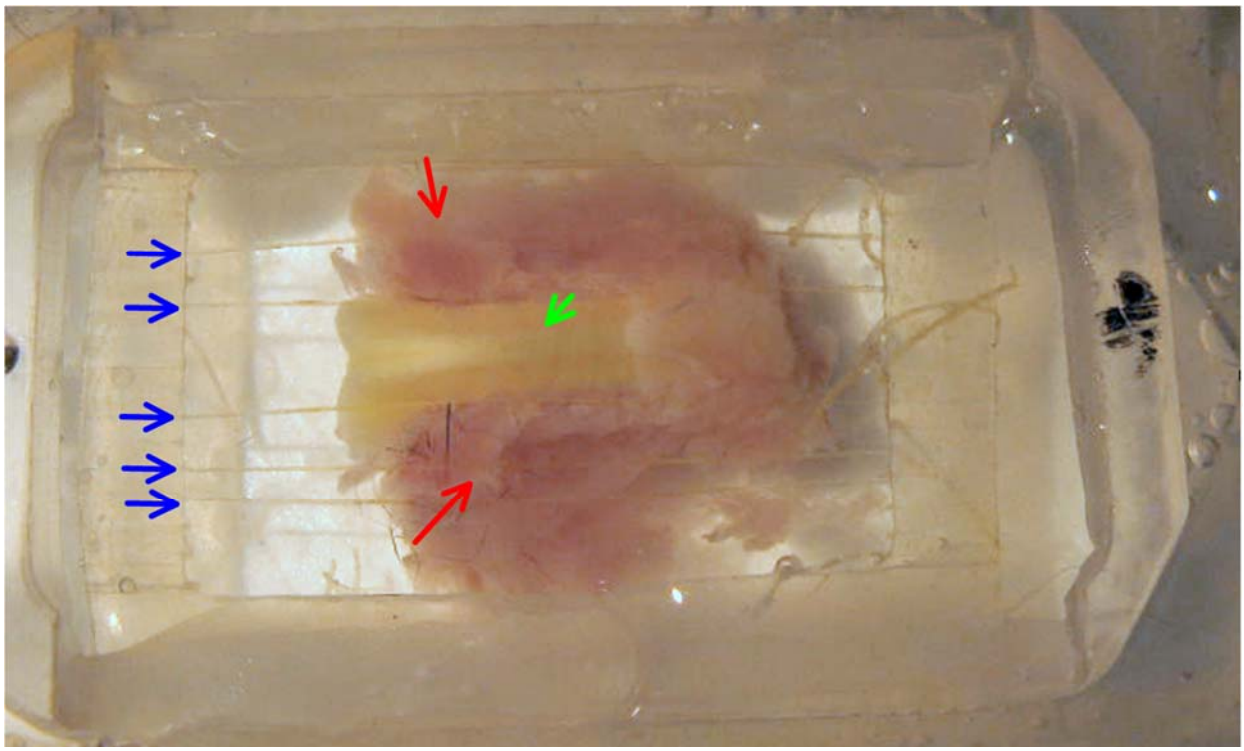

Figure 3-5. The demonstration of contactless technique to immobilize spinal cord explant for *ex vivo* imaging

To immobilize the explant for extended imaging, a modified plastic anchor with specific array of horizontal cord lines (blue arrows) was created. The cord lines were forced onto the ventral connective tissue (red arrows) in order to hold the tissue tightly without making contact with dorsal column. The region of interest was the area of superficial fasciculus gracilis located at the middle region of spinal cord (green arrow).

3.6 Troubleshooting

3.6.1 General live imaging related issues

A good imaging technique depended on balancing 38 parameters in the current standardized microscope with digitization of detectors[98]. Knowing the acceptable minimum threshold of pixel value for data analysis and knowing the maximum capability of optical resolution, light sources, and sampling frequency was important. It was also important to minimize tissue damage by free radical from the adverse effect of optical and light sources by avoiding saturating the intensity of images with excess power and dwell time of light sources.

3.6.2 Spectral imaging

Spectral imaging was used to image multiple fluorescence groups, which also included auto-fluorescence and background noise (Appendix B). The spectra of each fluorescence group can later be separated and assigned into a channel by a linear decomposition algorithm. Imaging multiple groups of fluorescent signals (e.g. YFP, CFP, and NR) required knowledge of adjusting fluorescent intensity. Often, the levels of intensity from each signal are not equal and cannot be excited equally, which could result in poor spectral decomposition. To troubleshoot such issues, start with lower concentration of exogenous vital dye and slowly increase the concentration to achieve similar intensity of intrinsic fluorescent signal.

3.7 Results

3.7.1 Fluorescent imaging of myelinated axons

For imaging of myelinated axons using transgenic mice expressing YFP in axons, I found that there was minimal disruption of cytoarchitecture (Figure 3-6a). I used a vital dye NR, a lipophilic fluorescent dye that specifically labels lipid of myelin, to label myelin in the YFP-tagged axons of transgenic mice. This method reveals internodes, and unequivocally visualized CNS nodes of Ranvier (Figure 3-6b, white arrows). I next asked if such high-resolution imaging could reveal the integrity of myelinated axon. I then use the measurement of the g ratio with optical sectioning.

$$\text{Optical g ratio} = \frac{The\ axon\ diameter}{the\ fiber\ diameter} \quad (2)$$

Optical g ratio is the measurement of the axonal diameter divided by the diameter of myelinated axons (aka fiber diameter); both diameters obtained from the X-Z projection of 3D images. I found 0.587±0.084 of the g ratio (n = 20 axons in three mice) is very close to the previously reported light microscopy measurement in rabbit fibres[99] (Figure 3-7). The measurement of g-ratio from electron microscopy image shows that there is no differences between rabbit fibres and mouse[100].

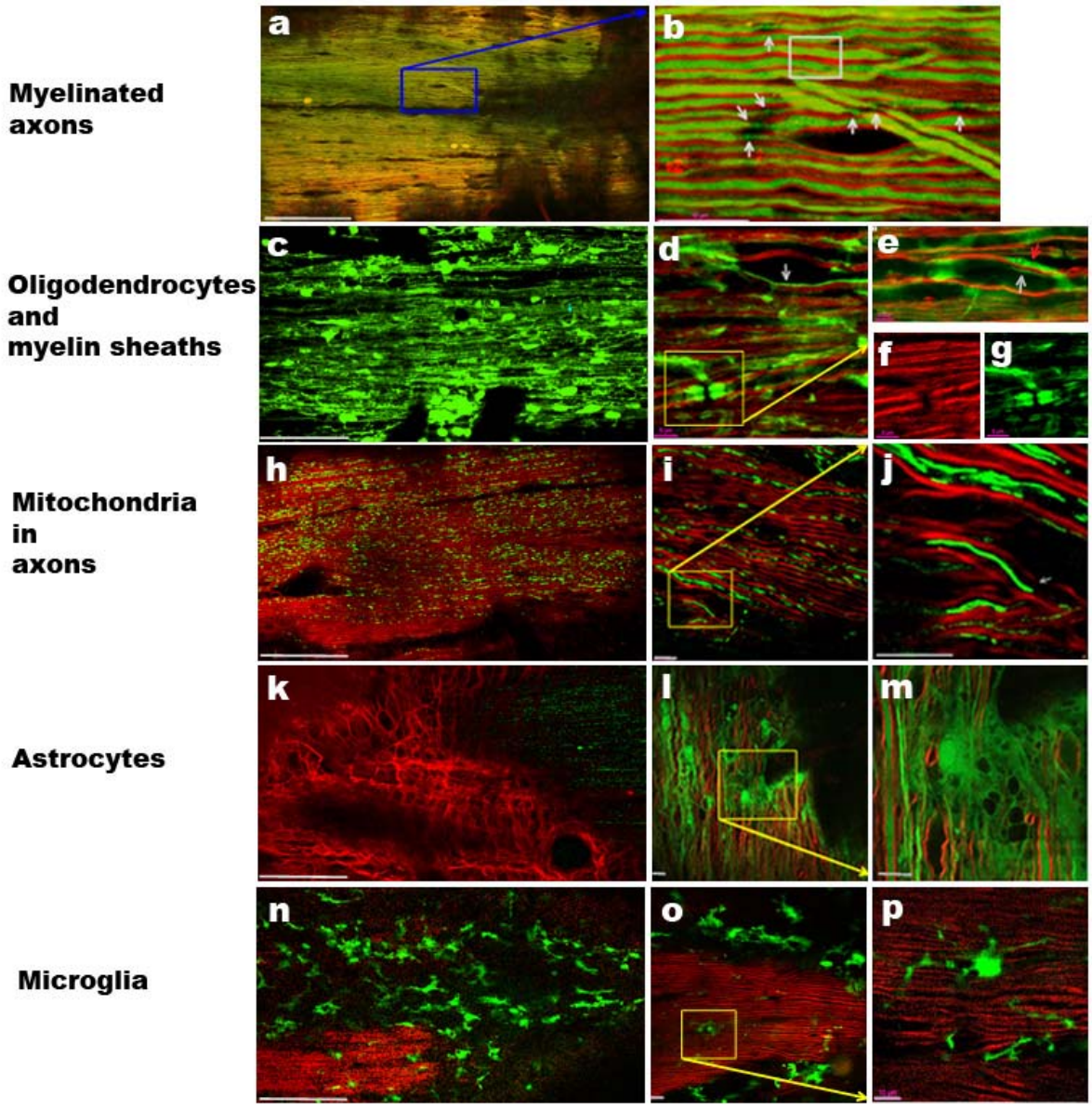

Figure 3-6. High spatial resolution of *ex vivo* imaging in dorsal column of spinal cord explant

Myelinated axons (a and b), oligodendrocytes and myelin sheaths (c-g), axonal mitochondria (h-j), astrocytes (k-m), and microglia (n-p) in high spatial resolution images were obtained from spectral confocal microscopy and nondescanned detection of two-photon microscopy. Large areas (500 µm x 250 µm) of dorsal column in a, c, h, k, and n represented the surface of fasciculus gracilis. Scale bars = 100 µm. a, myelin (red) labeled by NR in transgenic

mice expressing YFP in axons (green). b, the structures of internodes (white box) and a total of 7 nodes of Ranvier (white arrows) in a small area of 30 μm x 20 μm was revealed. c, the distribution of myelin (green) was imaged in dorsal column of transgenic mouse with GFP-tagged PLP-driven promoter in oligodendrocytes. d, high expression of GFP labeled paranodal region in green, compact myelin in red, inner loop of myelin sheath (grey arrow). e, inner loop (grey arrow) and outer loop (red arrow) of myelin sheath was imaged clearly. f and g, close-up view from yellow box in (d) showed myelin in red (f) labeled by NR and myelin in green (g) tagged by GFP expression. (d-g, scale bars = 5 μm). h, the distributions of axonal mitochondria (green) in dorsal column axons was imaged. The structure of axonal mitochondria in general was elongated with averaging 5 μm or above of length, and some mitochondria (i) were extremely elongated with incredible length of 16 μm (j). k, astrocytes surrounding the blood vessels were labeled by sulforhodamine 101[87] in transgenic YFP-tagged axons mice. m, zoom-in view of yellow square in (l) using transgenic mice GFP-tagged astrocytes showed large astrocyte resided next to the blood vessel. n, major distribution of microglia was shown as GFP expression (green) on the surface of dorsal column. o, there were fewer microglia on the surface of myelinated axons. p, close-up view of single microglial cell on the surface of myelinated axons.

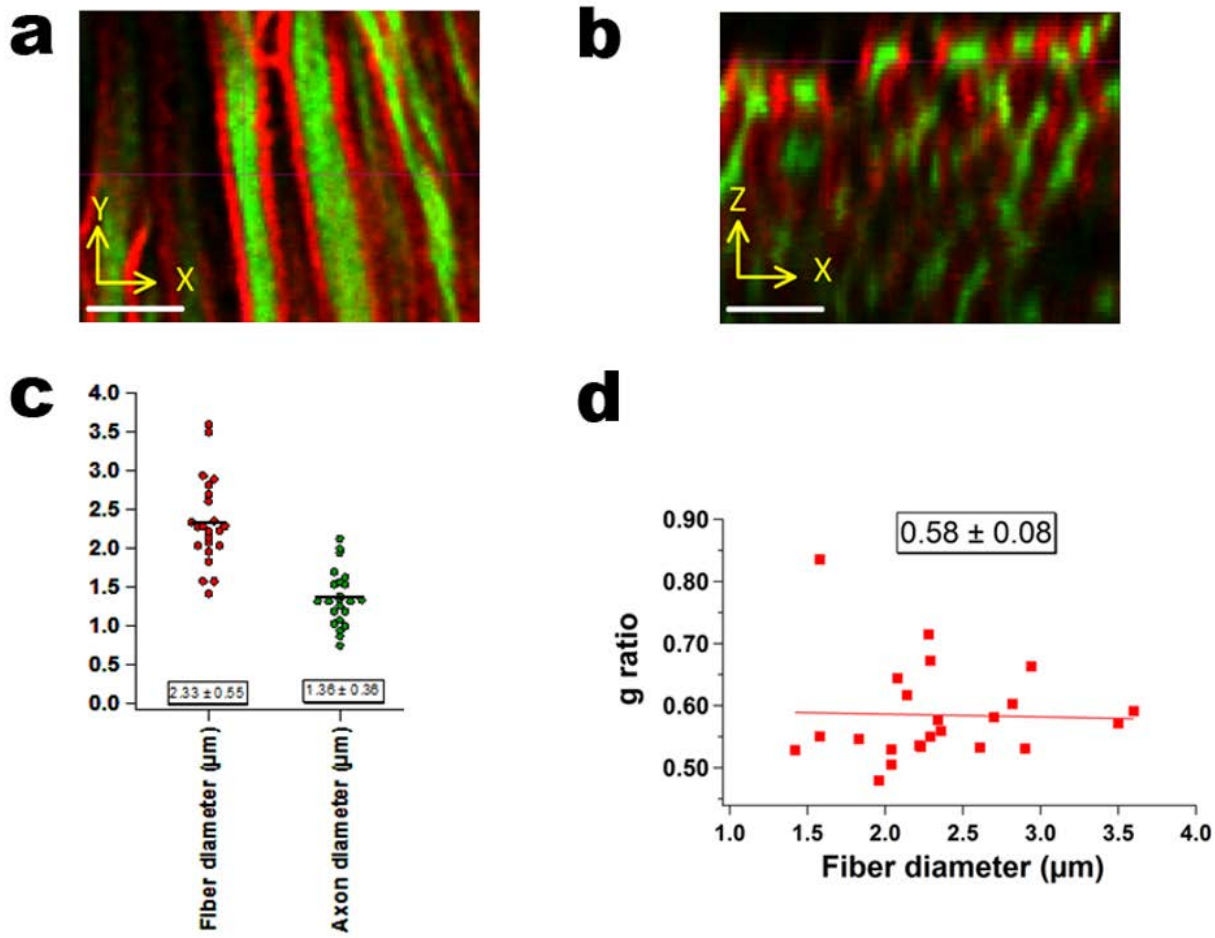

Figure 3-7. Measurement of g ratio from 3D images of live longitudinal myelinated axons

Combining the methods of NR stained myelin sheaths and YFP tagged axons allows the measurement of g ratio. a and b, deconvolved 3D image of myelinated axons (myelin in red and axon in green) in X-Y and X-Z projection. c, dot plot shows the total populations of fiber and axon diameters. Horizontal bars indicate the median of each population. d, quantification of g ratio from myelinated axons in X-Z projection (b) in which their fiber diameter was larger than 1.5 µm because this population can be resolved by optical microscopy. Horizontal bar indicates the average g ratio.

3.7.2 Fluorescent myelin imaging revealed compact myelin, inner loop, outer loop and lateral loop.

Using transgenic mice or vital dye, both methods showed different morphology of myelin sheaths and their distribution (Figure 3-8a-b). Transgenic mice (using GFP-tagged PLP-driven promoter in oligodendrocytes) showed disorganized myelin sheaths (Figure 3-8a). In contrast, NR labeled myelin showed highly order myelin sheaths (Figure 3-8b).

The use of combined transgenic labeling and vital dye labeling of myelin detailed in Figure 3-9b (schematic illustration in Figure 3-9a). I observed that the distribution of GFP in these transgenic mice was mainly in the region of non-compacted myelin. A clear paranodal region with high intense GFP labeling were seen (Figure 3-9c) and the distribution of GFP did not fully fill the regions of compact myelin. The compact myelin was labeled by NR in red (Figure 3-9c, d and e). Fine details of compacted and non-compacted lateral, inner and outer loop of myelin sheath was shown in Figure 3-9d. NR clearly labeled the compact myelin (Figure 3-9e, two orange asterisks), and GFP tagged in the inner (Figure 3-9c-d, grey arrows) and outer (Figure 3-9d, red arrow) loop of myelin sheaths.

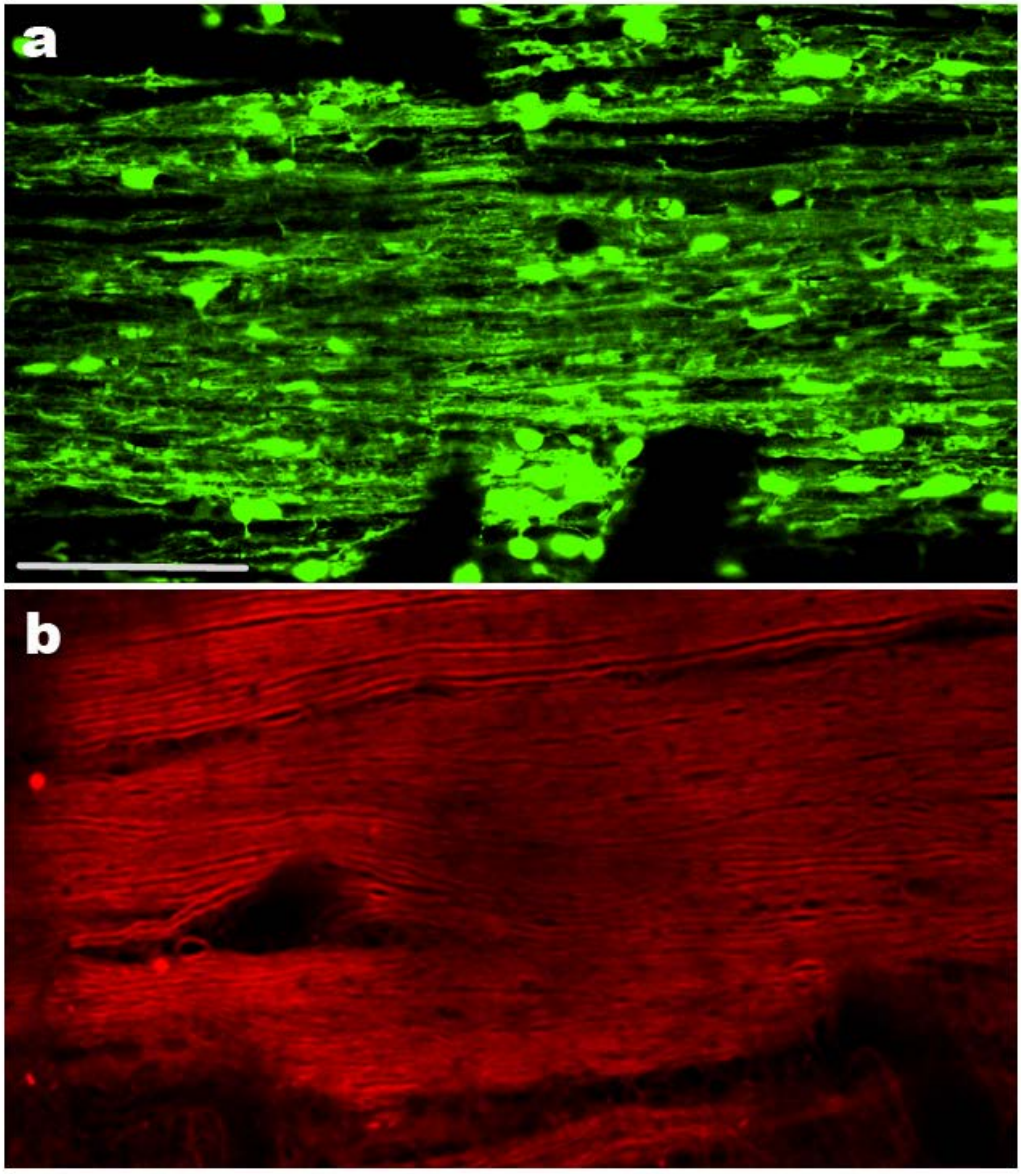

Figure 3-8. Comparison of myelin distribution between transgenic mice (a) and exogenous dye-NR (b) labeling myelin sheaths

a, disorganized myelin sheaths were shown in transgenic mice with GFP-tagged PLP-driven promoter in oligodendrocytes. b, myelin sheaths stained by NR appear as highly order structures. Scale bar = 100 μm

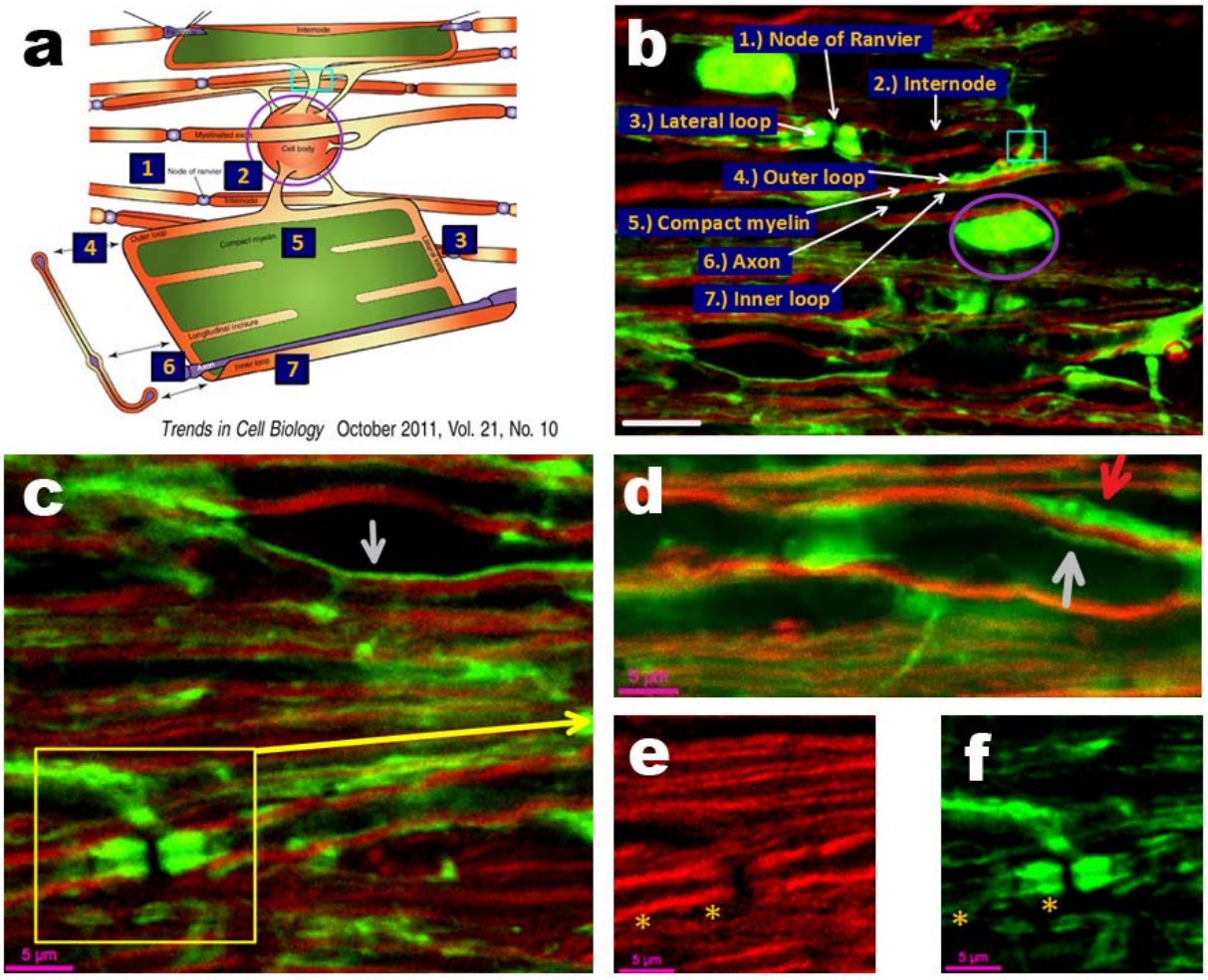

Figure 3-9. The cellular features of myelinated axons and oligodendrocytes

a, schematic illustration of the cellular features of myelinated axons (adapted from Aggarwal et al. 2011[101]) compared to the *ex vivo* image (b) of myelinated axons using NR-stained myelin in transgenic mice expressing PLP-GFP in oligodendrocytes. Purple circle was the cell body of an oligodendrocyte. c, high expression of GFP labeled paranodal region in green, compact myelin in red, inner loop of myelin sheath (grey arrow). d, inner loop (grey arrow) and outer loop (red arrow) of myelin sheath (c). e, NR labeled myelin in red (orange asterisks). f, lower expression of GFP (right orange asterisk) and higher expression of GFP (left orange asterisk) in myelin.

b, scale bar = 10 µm; c, d, e and f, scale bar = 5 µm

3.7.3 Imaging subcellular mitochondria in axons

Using an intact explant of transgenic mouse expressing CFP driven byThy1-Cox8-promoter, I showed that the distribution of axonal mitochondria was approximately 11,000 mitochondria per mm^2 in dorsal column (Figure 3-6h, pseudocolor in green). Elongated mitochondria were most common, which unexpectedly can be over 16 μm long (Figure 3-6j).

3.7.4 Imaging of astrocytes and microglia

Transected spinal cord without the disruption of its cellular integrity allowed high spatial resolution imaging of astrocytes (Figure 3-10) and microglia (Figure 3-6n-p). These two groups of glia cells showed distinct population distribution. The imaging also showed projections of their processes. The astrocyte was adjacent to the blood vessel and with its processes "glued" onto the surface of myelinated axons and formed presumably glia limitans (Figure 3-10). Microglial cells rarely resided close to axons, but they surrounded the dorsal column (Figure 3-6n and o).

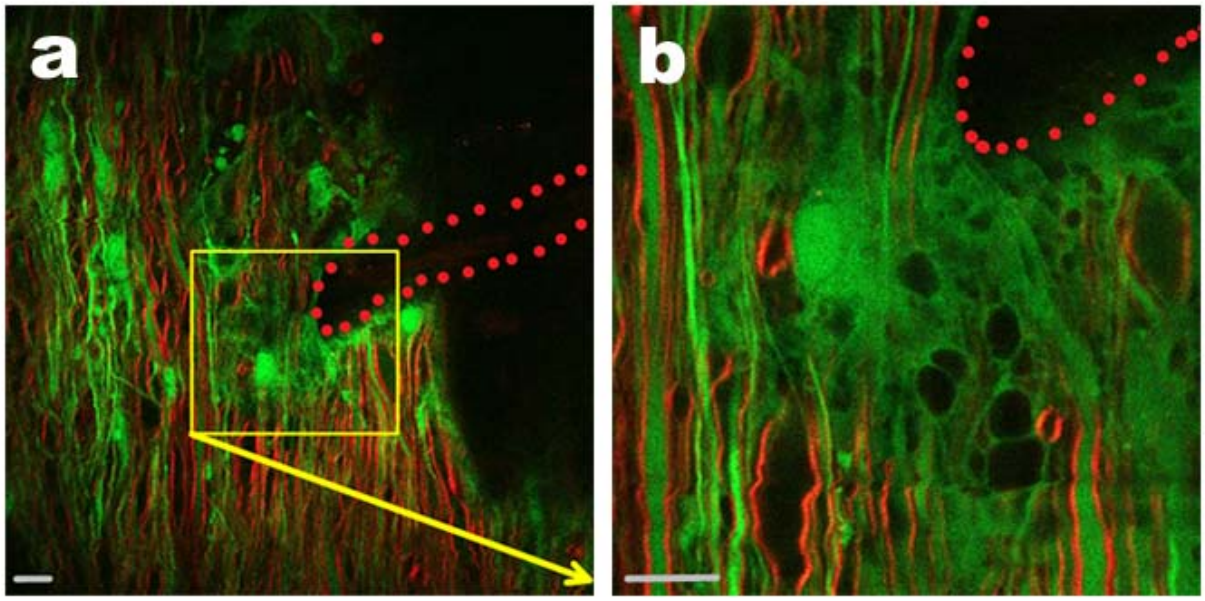

Figure 3-10. The distribution of astrocytes in dorsal column

a, an astrocyte distributed around blood vessel (yellow box) in transgenic mice expressing GFP in astrocytes and YFP in axons. The image was taken by two-channel two-photon microscopy, hence both axons and astrocytes were shown in green color. Blood vessel is labeled by the red dotted line. b, close-up view from (a, yellow box). The cellular processes of astrocyte contacted the blood vessel and superficial area of myelinated axons. Scale bars = 10 μm

3.7.5 The diffusion rate of fluorescein in the explant

Unlike *ex vivo* model, *in vivo* models are more complex and difficult to control. For example, systemic administration of drugs is subject to metabolism by the liver and may be restricted from the CNS by the blood brain barrier. The effect of drugs is diminished by tight environmental control[102]. A major advantage of using *ex vivo* model is that it reliably provides control of the extracellular milieu. In this model however, intact leptomeninges[103] might pose a problem for diffusion. To address this, I applied fluorescein, a polar tracer to record the timing of the penetration. Upon entering the perfusion chamber, fluorescein diffused to most of the structures including dura and arachnoid mater (Figure 3-11a) within a second, and subsequently diffused into subarachnoid space (Figure 3-11b, red asterisk) after 30 seconds. About a minute later, subarachnoid space was filled completely with fluorescein, as shown in area where the blood vessels were located (Figure 3-11b, grey arrows). In dorsal column spinal cord, axons are distributed underneath the subarachnoid space[104]. My result cannot determine when the dye diffused into the axons because the YFP-tagged axons mice and the fluorescein share similar emission spectra. To address this, I used wild-type mice to determine when the dye diffuses to the axons. SHG imaging was used to locate the subarachnoid space so that the exact location of axons can be determined. Axons were labeled by fluorescein (Figure 3-12) after 30 minutes. Taken together, the results likely indicated that the diffusion first passed through the subarachnoid space, and subsequently diffused through glia limitans and paranodal region of myelin sheaths[105] before finally accessed axons. Here I demonstrated that the structure of leptomeninges could be the diffusion barrier and the diffusion barrier slow down the penetration.

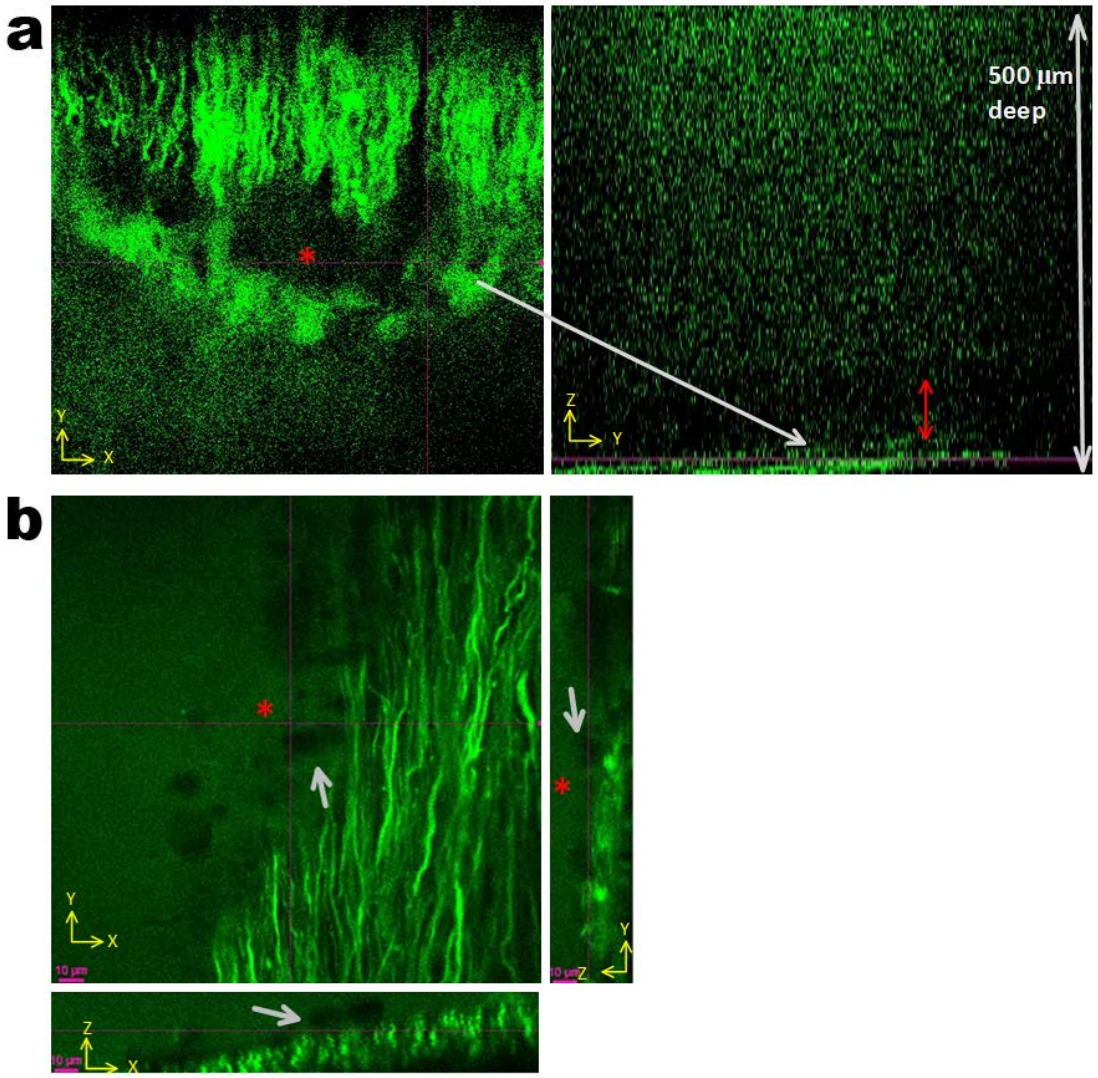

Figure 3-11. Confocal imaging of fluorescein diffusion into dorsal column of transgenic mice expressing YFP in axons

a, (left panel) arachnoid membrane (grey arrow) was labeled instantly but not in subarachnoid space (red asterisk). a, (right figure) the fluorescein diffusion was imaged with optical sectioning of 500 µm thicknesses with 5 µm interval (grey double-headed arrow). The gradual decrease of fluorescein intensity was imaged from top to bottom (Y-Z plane). b, fluorescein diffused to the surface area of axons (green, long slender structure) within a minute. The area included subarachnoid space (red asterisk). The black hollows (grey arrows) in the subarachnoid space were big and small blood vessels that were not labeled by fluorescein.

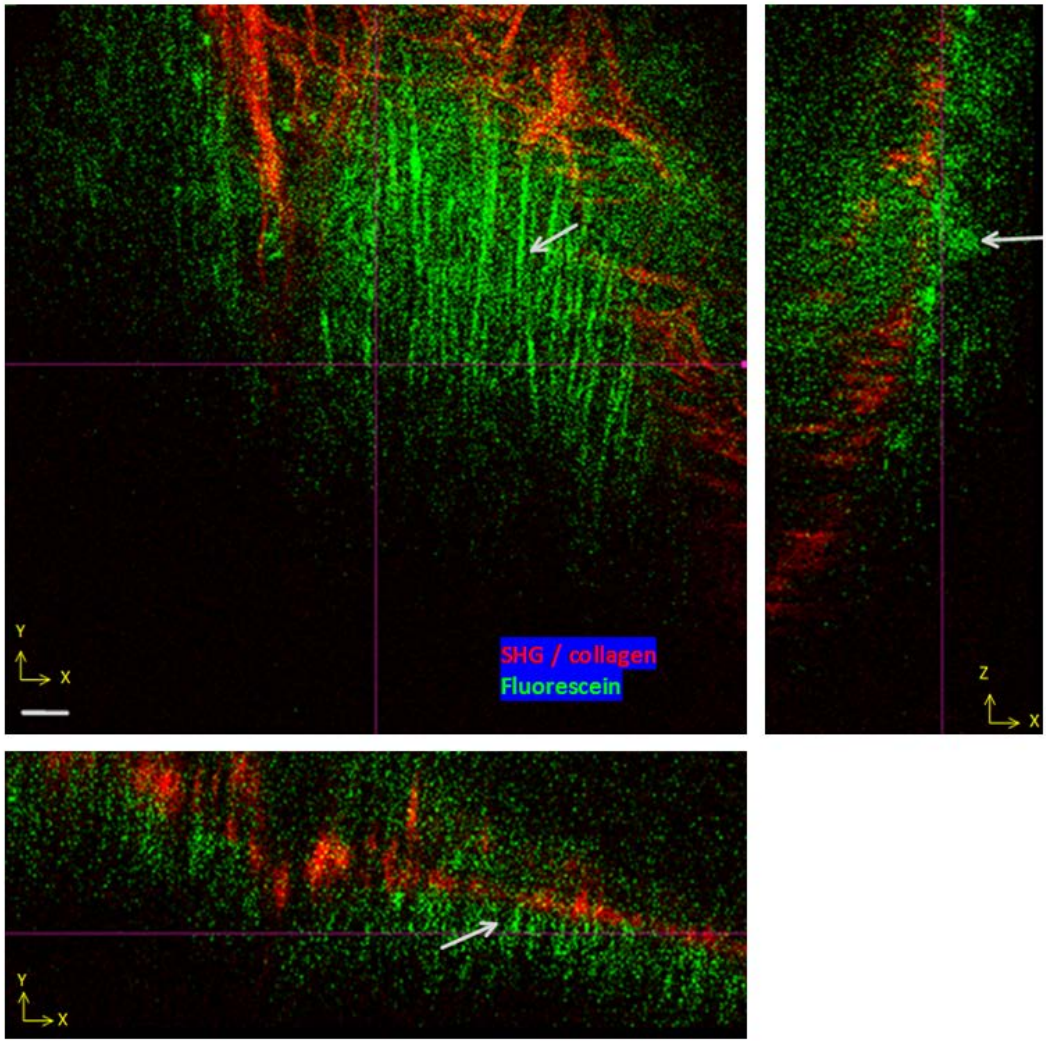

Figure 3-12. Optical sectioning with SHG imaging of collagen and fluorescein dye in the dorsal column of wild-type mice

Wild-type mice were used to trace the fluorescein dye in the axons that cannot be achieved using transgenic mice expressing YFP in axons (because the color of YFP is similar to fluorescein dye). SHG imaging of collagen (red) on superficial dorsal column was performed to position the unstained axons before adding the dye. After more than 30 minutes of perfusion with 10 µm of fluorescein dye (as shown in the figure), the dye tracer accessed to axons (grey arrows). Axons (green) were labeled by fluorescein. Scale bar = 10 µm

3.7.6 The effect of Wallerian degeneration

The transected cervical spinal cord explant will induce Wallerian degeneration of ascending and descending tracts. The dissected dorsal roots were affected sooner than the dissected dorsal columns (Figure 3-13b and c). Since the distal portions of dorsal roots were very close to the dorsal root ganglion, the effect of Wallerian degeneration appeared earlier than the dorsal column and it can be observed during the first 8 hours of imaging. The distal portions of fasciculus gracilis and fasciculus cuneatus in dorsal column was unaffected by Wallerian degeneration during first 8 hours of imaging because fasciculus gracilis and fasciculus cuneatus were far away from their cell bodies.

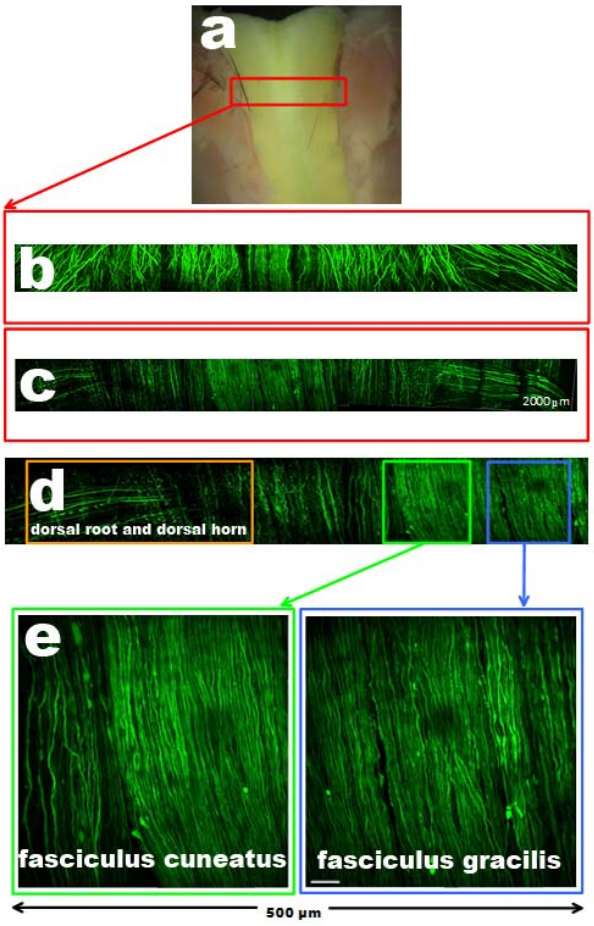

Figure 3-13. Eight hours of perfused dorsal column of cervical spinal cord explant in oxy-carbonated aCSF solution at 35°C shows minimal pathology

The explanted tissue (a) showed the surface of longitudinal axons (green) with the presentation of stitched maximum intensity projection by two-photon microscopy (b). After 8 hours of perfusion, I imaged the same entire section of dorsal column (c). The distance from left to right dorsal root was about 2,000 μm. Both contralateral dorsal roots were perpendicular to dorsal column nerves with much structural alteration (d, orange box). The distal portions of dorsal roots that were located closest to their own cell body were most susceptible to the Wallerian degeneration. In contrast, the fasciculus cuneatus (e, green box) and gracilis (e, blue box) showed minimal disruption from the effect of Wallerian degeneration because the distal portion of gracilis and cuneatus are located furthest from their cell bodies. Scale bar = 10 μm

3.7.7 Limitation of the model

Any explanted tissues are limited by time for good experiment imaging. Experiments intended for longer imaging or long incubation requiring gene expression will not work in my model. The live myelinated axonal imaging offers about 8 hours (Figure 3-13) of morphologically stable imaging. Beyond 12 hours, ASF could occur. Unlike other organotypic spinal culture models[106–108] and *in vivo* spinal cord imaging model[109–111], the main advantage of my model is for relatively long-term (many hours) high-resolution imaging of fine structure of CNS axons and their myelin.

3.8 Discussion

The adult spinal cord explant is beneficial in many ways for white matter imaging experiments. First, spinal cord explants have been vigorously tested and used for functional study of white matter by electrophysiologists for many decades[112,113]. Isolation of axonal function in complex tissue like spinal cord explants was made feasible by using pharmacological approaches and quantifiable measurement of compound action potential. The published model is useful to study energy deprivation-mediated white matter injury[114–116] and to dissect molecular mechanism of white matter injury[13,32,33,82,117]. In my study, the detailed cellular morphology of white matter was demonstrated. Imaging of inner loop and outer loop allows the study of detailed myelin pathology. The cytoarchitecture of adult white matter resembles the *in vivo* state, in contrast to cell culture model and organotypic spinal cord slice culture where glial cells and myelinated axons lack physiological cytoarchitecture[106–108,118].

Second, axons have been proposed to have the ability to perform local cellular activity without regulation by their cell body and they are in intimate contact with myelin sheaths[119]. Glia and myelin communicate with local axons to provide long-term integrity and survival of axons[120,121]. In my model, the cervical fibers of superficial fasciculus gracilis belong to dorsal root ganglia located inferiorly[122]. The fibers were completely devoid of neuronal cell bodies after explant and the axon can survive up to 8 hours without sign of injury (Figure 3-13). Hence, the model is an advantage for the study of axonal interaction with myelin or local glia and local pathological progression in white matter such as ASF.

Third, most of the nerves in dorsal column form the vertical ascending tract which originated from horizontal dorsal root ganglia (Figure 3-13e). This might facilitate the study of orientation dependent axoplasmic transport, such as anterograde or retrograde live imaging, and the use of polarized light interaction with myelin[85].

Fourth, activated immune cells in central white matter injury that caused inflammatory reaction must pass a barrier of connective tissue (comprised of type IV collagen) before they damage the myelinated axons[124,125]. To penetrate the barrier, production of matrix metalloprotease are activated by the cells. Once barrier is breached, some inflammatory cells infiltrate into the white matter of the CNS via glia limitans superficialis[126]. My results showed that the surface area of dorsal column was completely covered by the collagen. The model might be ideal for the study of connective tissue injury of white matter such as the process of breaking down the tissue by the immune cell. This process is similar to my study of breaking down the diffusion barrier by collagenase using SHG imaging in Chapter 4 (Figure 4-12).

Finally, myelination takes years to be developed[127] and accurately mimicking the myelination process in cell culture model is not possible. The maturation of myelinated axons is significantly different from the development of myelinated axons in cell culture as compared to the biochemical properties of myelin[128] and their interaction with other glial cells. This might suggest that use of intact adult white matter as a model is clinical relevance to study adult white matter injury.

3.9 Conclusion

Axons and glial cells in white matter have close intimate relationship. Here, I provided the protocol and validation of the cervical spinal cord explant as a more representative white matter imaging model than neuron-oligodendrocyte myelination co-culture. The explants allowed high-resolution imaging of myelinated axons and its glial cells, which now allowed me to carry out a detailed study of subcellular morphological changes during a variety of pathological insults.

Chapter Four: Morphological characterization and molecular mechanism of axon spheroid formation

4.1 Abstract

Recent studies have implicated glutamate-mediated excitotoxicity in the degeneration of white matter elements in multiple sclerosis (MS) patients[1,129–131] and in animal models of MS[132]. Axonal spheroid formation precedes transection has also been reported in MS tissue[9]. In white matter injury, glutamate-mediated excitotoxicity leads to calcium rise has been reported[32–34]. However, whether glutamate-mediated excitotoxicity would induce axonal spheroid formation (ASF) is unknown in *ex vivo* model. I set to hypothesize that glutamate-mediated excitotoxicity is one of the mechanisms to induce ASF. I adapted an *ex vivo* imaging model of mouse spinal cord explant for the study of ASF and utilized two transgenic mouse lines to address this hypothesis. Mice expressing yellow fluorescent protein (YFP) from the Thy1 promoter allowed the visualization of axonal structures and were used to study axonal morphological changes. Transgenic mice expressing a calcium biosensor were used to detect and quantify calcium activity in the axon. Activation of glutamate receptors caused calcium overload in the axon, and ASF and transection ensued, which was blocked by glutamate antagonists. Furthermore, intracellular calcium release triggered by the activation of ryanodine receptor in axoplasmic reticulum contributed equally to ASF as did excitotoxicity. Taken together, the results closely resembled those of lesion in MS. Thus, using a well-controlled *ex vivo* model mimicking axonal injury in MS, I demonstrated the temporal relationship of ASF and axonal transection in the living white matter tissue, a model that could help better define cellular target for the pathogenesis of MS lesions and in particular the non-inflammatory progressive MS[51].

4.2 Introduction

Axonal loss resulting from axon injury is the common denominator of a number of different disease processes in the central nervous system (CNS) and the determinant of irreversible neurological disability in most patients. Examples include MS[44] and spinal cord injury[133,134]. Since the fragile axon structure is slender and requires high energy for electrochemical activities, it susceptible to the irreversible effect of axonal transport disturbances[135,136], inflammatory responses[24], energy deprivations[137], virus infections[6]. Many researchers believe that a wide range of insults to the axon can trigger active cellular responses particularly ASF and subsequent loss of neuronal cell bodies. It is thought that loss of axons is a key predictor of the clinical outcome[8]. Therefore, a better understanding of the underlying mechanisms of ASF can guide improved treatment of many neurodegenerative diseases where myelinated axons are affected.

4.3 Axonal spheroids in Wallerian degeneration

Axonal spheroids were observed in the peripheral nervous system (PNS) by Waller in 1850 who later described the degenerative process of distal portion of axons with swelling "tubes" after the nerves were cut or crushed. This process has been called Wallerian degeneration[27]. Later in 1928, such structures were further described by Cajal[26] in the CNS. These observations describing the phenomenon of ASF are a cardinal pathological feature of axonal degeneration. However, the precise mechanisms of ASF are still unclear. A wide range of insults to the axon can trigger ASF and several parallel injury mechanisms might be involved[138]. For example, ASF found in chronic MS brains might be caused by relative energy deprivation due to demyelination[24,139] or glutamate-mediated excitotoxicity[140], while traumatic spinal cord injury may be Wallerian degeneration resulting from crushed nerves[141–146]. Furthermore, studies from

traumatic injury in the CNS showed that the mechanism of ASF requires loss of nicotinamide mononucleotide adenylyltransferase2, an axonal survival signal[138]. This was demonstrated by the Wallerian degeneration slow (Wlds) mutant mice. The Wlds mice expressing chimeric fusion gene Nmnat1 (Ube4b +NAD)[147] significantly delayed Wallerian degeneration[124] and inhibited axonal spheroids formation[148]. However, non-traumatic injury resulting in ASF and degeneration such as MS is being neglected[149]. In this chapter, I investigate non-traumatic white matter injury of ASF in MS.

4.4 Axonal spheroid in MS

The first observation of axon spheroid in MS patient was reported by Jean-Martin Charcot in 1868[150] and later studies by Frommann and Bielschowsky[151,152]. Ultrastructural analysis of axonal spheroid was performed in an EAE model by Lampert in 1967[153,154]. He reported that reactive axonal enlargement (axonal spheroid) consisted of axon associated with an accumulation of mitochondria, membranous dense bodies, vesicular elements, and neurofilaments. Lampert also observed that demyelinated axons and spheroids appeared frequently surrounding the lesion. Using confocal microscopy and immunohistochemistry, Trapp et al. showed and quantified axon spheroids and transections in MS brain[9]. Case-controlled post-mortem examinations using either immunohistochemistry (against NF, SMI-32[9] or NAA[155]) or Palmgren's silver staining method[28] showed strong correlation among the frequent axonal swelling, numerous axonal transection, a high degree of inflammatory demyelination and the severity of disability[156–161]. One study found axonal abnormalities in normal-appearing white matter by electron microscopy and confocal microscopy[162]. More recent studies showed that axonal loss occurred as early as 7 days post-immunization in EAE model[163] and axonal debris

such as neurofilament can trigger MS-like symptom in autoimmune animal model of MS[164–166]. Axonal injury could precede demyelination early in the course of MS and activate the immune response. Thus, axonal injury could be the underlying mechanism that contributes to the effects of MS[167]. These results strongly suggest that MS might be a neurodegenerative disorder with the convolution of inflammatory reaction[51].

4.4.1 Role of calcium in ASF

The mechanism of axonal degeneration was first proposed by Schlaepfer and Bunge in a culture model of dorsal root ganglion. They found that low calcium or calcium free media reduced axonal injury with no ASF[168]. In addition, energy deprivation and glutamate-mediated excitotoxicity models of white matter injury suggest the role of calcium in axon pathology[13,169,170]. In the energy deprivation pathway, interruption of adenosine triphosphate (ATP) production from mitochondria in hypoxic injury arrested the function of ATPases. Na/K ATPases are affected the most due to their role in maintaining the resting membrane potential throughout the entire axon[171,172]. The loss of function of this pump will induce aberrant depolarization. Na^+ eventually accumulates in the axon and triggers reversed function of Na-Ca exchanger (NCX) by pumping a Ca^{++} ion in and releasing 3 Na^+ out, leading to the accumulation of Ca^{++} in the axon[173,174]. Axonal depolarizing induced by the influx of Na^+ current via $Na_{v1.6}$ and efflux of potassium triggers release of glutamate and activation of glutamate receptors leading to more calcium influx[175,176]. Hence, in the condition of energy deprivation, calcium rise accompanies glutamate-mediated excitotoxicity. Glutamate-mediated excitotoxicity is therefore one of the major mechanisms of axonal degeneration in a hypoxic injury model[177]. To directly address the role of glutamate and calcium activity in axons, Ouardouz et al. used calcium

imaging in isolated dorsal column explant and perfused with glutamate receptor agonists/antagonists[32,33]. They found a correlation between calcium rise and glutamate receptor activation. Over-activation of glutamate receptors leading to calcium rise in axons was a surprising discovery[178] because such mechanisms were previously thought to be unique to grey matter injury where glutamate-mediated excitotoxicity was well-established[179]. Based on these previous studies, and the pathological importance of axon spheroid formation seen in many diseases, I therefore set out to study in mechanistic detail the molecular pathways and receptors responsible for a variety of spheroid pathology seen in myelinating fiber tracts. I developed a very stable and precise *ex vivo* imaging model as described in Chapter 3, which allowed me to precisely observe and follow development of pathology in real-time, and to control the extracellular environment of the cells and tissue during application of various agents.

4.5 Method

4.5.1 Animals and group assignments

Animals in these studies were handled in accordance to the guidelines of the Canadian Council on Animal Care and all animal procedures were also approved by the University of Calgary Animal Care Ethics Committee. Transgenic mice were bred and cared in-house in the animal care facility. Experiments were conducted with specific pathogen-free transgenic mice with the genetic background of C57BL/6 line. Two transgenic mouse lines were used for the explant imaging studies (1-3 months old). To examine axonal distribution and morphology, B6.Cg-Tg(Thy1-YFP)16Jrs/J mice (The Jackson Laboratories, Bar Harbor, ME) expressing YFP in the dorsal column axons[92] were chosen. Transgenic mice expressing calcium binding gene Troponin-

C (K_d =1.2 μM)[180] with FRET-pair biosensor expressing donor-CFP/cerulean and acceptor-YFP/citrine (CerTnL-15) (a gift from Dr. Griesbeck at Max-Planck-Institute[181]) were also used.

4.5.2 Assessment of ASF and ROI

All the YFP expression axons were imaged by two-photon nondescanned detection at 900-950 nm with power < 10 mW. The ROIs was the superficial dorsal column (Figure 3-5). All the ROI data consisted of 3D images projected in the xy, xz, and yz planes for counting the distribution of spheroids in total volume of 400 x 400 x 40 um^3 (x,y,z) in each animal. Average intensity for morphological study was based on the contrast ratio between the ROI and the background at 50-100:1. If the diameter of and axonal swelling was at least twice that of the parent axon, it was counted as a spheroid. Spheroid counts were performed by scanning through the 3D data.

The structures of sub-micron puncta in spheroids were examined using deconvolution. The 3D-blind (adaptive point spread function) deconvolution algorithm from AutoQuant X version x2.1.2 was applied and did not require the calibration and measurement of the point spread function. Blind deconvolution required the following parameters: x, y, and z dimension, emission light (YFP), modality of microscope (laser scanning confocal), immersion media (water = 1.33), numerical aperture and magnification of objective lens (NA1.0, 60x). Images were processed with 10 iterations and medium noise value.

4.5.3 Baseline study

Cervical spinal cord explant preparation was performed as described in Chapter 3. Each dissection took less than 30 minutes. Over the period of my study, ASF were observed after

dissection and the spheroid were subsequently reversed within one hour (Figure 4-1). To eliminate the variation from spontaneous primary injury, all treatments were started at least 1-2 hours after the dissection. The remaining time-slot allowed the tissue to settle down as a reset cycle. Thirteen Thy1-YFP mice were used for the baseline study (range: 7-12 hours, 1 hour per time point) after excision.

4.5.4 Pharmacological application and imaging

4.5.4.1 Chemical anoxia and glutamate-mediated excitotoxicity

Sodium azide (NaN_3) was used to induce energy deprivation-mediated ASF because NaN_3 inhibits the production of ATP in mitochondria[182]. A total of 24 mice were used, two or three mice per study: 2.0 mM NaN_3 alone, 0.5 mM NaN_3 with 0.2 mM glutamate, 2.0 mM NaN_3 with 0.2 mM glutamate, 0.5 mM NaN_3 alone, 10 mM glutamate alone, 0.5 mM NaN_3 with 10 mM glutamate, 0.5 mM DL-threo-beta-benzyloxyaspartate (TBOA) alone, 0.5 mM TBOA with 10 mM glutamate, and finally combination of 0.5 mM TBOA, 10 mM glutamate and 0.5 mM NaN_3. The treatment remained on the spinal cord for the duration of the entire imaging. Images were recorded immediately after application (every 20-60 minutes for the entire experiment).

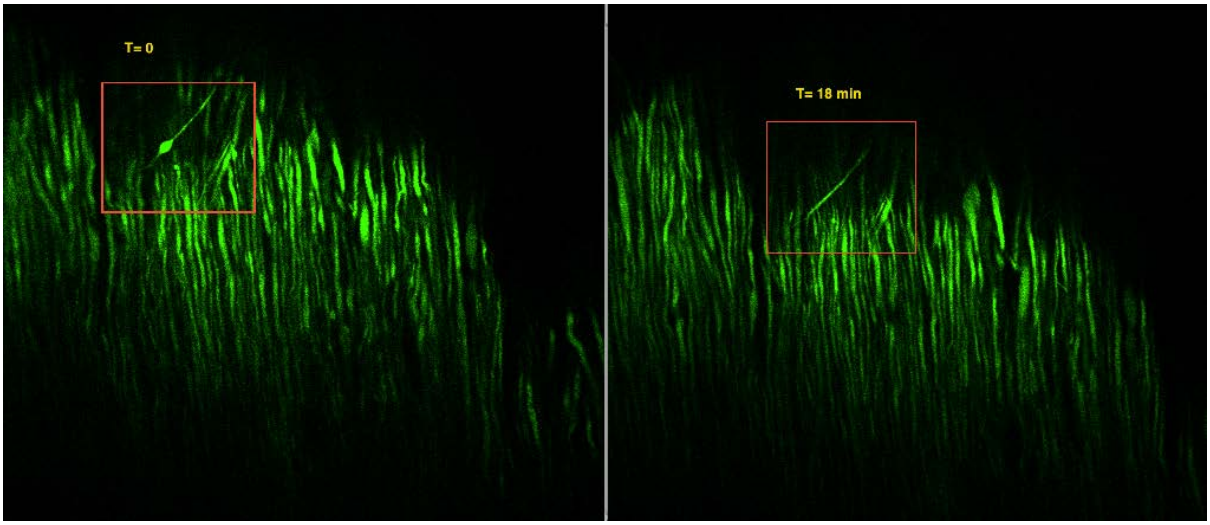

Figure 4-1. An example of a reversible form of axonal spheroid

An axonal spheroid appeared right after dissection during *ex vivo* imaging of transgenic mice expressing YFP in axon (green). After 18 minutes of perfusion, the spheroid reversed to normal appearance. This is a common observation right after cervical spinal cord dissection. Hence, all the imaging experiments were performed one hour after cervical dissection to reduce the variation in spheroids counting.

4.5.4.2 Glutamate excitotoxicity-mediated ASF after collagenase treatment

For *ex vivo* imaging, I applied 1 mM glutamate to the exposed spinal cords of healthy Thy1-YFP mice (N = 6). Control group was prepared without adding glutamate treatment (N = 4). The treatment remained on the spinal cord for the entire imaging duration. Images were recorded immediately after application and every 60 minutes for entire experiment. ROIs were collected as described in section 4.5.2.

For the antagonist experiments, cross-sectional study was performed. Three groups (3 mice per group) of treatments were prepared: 1 mM glutamate, 1 mM kynurenic acid (KA), and combined 1 mM glutamate and 1 mM KA. Note that the combined KA and glutamate experiment was prepared by first adding KA, followed by glutamate after 30 minutes. For all the experiments, the treatment of the explants incubated for 5 hours and then fixed by 4% paraformaldehyde for spheroid counting next day.

4.5.4.3 Calcium imaging in glutamate or caffeine treatment

Twenty CerTnL-15 transgenic mice were used to image calcium activity with spectral laser-scanning microscopy. Caffeine was used to induce intracellular calcium release via overactivation of ryanodine receptors[183]. 20 mM of caffeine was added into artificial cerebral fluid (aCSF), which was continued for the duration of the experiment. Glutamate experiment design was same as the *ex vivo* imaging protocol described in section 4.5.4.2.

4.5.4.4 Caffeine-mediated ASF

Three Thy1-YFP mice were used. Experimental design was the same as the *ex vivo* imaging protocol described in section 4.5.4.2. Three mice were used for antagonist experiments. Ryanodine was added in perfusate for one hour followed by caffeine. Ryanodine binds to ryanodine receptors and fully closes them at micromolar concentration to block ryanodine receptor from being activated[184].

4.5.5 Spinal lysate preparation for in vitro förster resonance energy transfer (FRET) analysis

To inhibit protease activity, spinal lysate was prepared by adding cOmplete ULTRA Tablets, EDTA free (Roche) in isolated dorsal column explant and dissolved in 1X phosphate buffered saline (PBS) solution. To chelate calcium, EGTA was dissolved in NaOH and the pH was adjusted to 7.2.

4.5.6 Imaging experiment for collagenase treatment

To break down the diffusion barrier of collagen in explants, collagenase was used. After laminectomy and before the cervical spinal cord was transected, the entire spinal cord was submerged in oxygenated aCSF solution with 300 unit/ml of type IV collagenase (Sigma-Aldrich) for 10 minutes at 35ºC. Tissue was slowly rinsed three times with aCSF for 5 minutes at room temperature. The cervical spinal cord was then transected and put onto imaging/perfusion chamber.

Label-free imaging with second harmonic generation imaging (SHG) was used to study collagen distribution in leptomeninges. SHG is a nonlinear optical effect whereby two near-infrared

photons interact with the sample to generate a new photon with twice the frequency (typically blue). Accordingly, the use of near IR 900 nm wavelength to interact with collagen would generate new photon half the IR wavelength at 450 nm. To confirm the specificity of SHG signals, I tuned the laser from 840 nm to 900 nm with SHG filter at 450 ± 35 nm. I then observed a clear SHG signal starting from 845 nm to 900 nm and no SHG signals below 845 nm.

4.5.7 Calcium imaging with spectral laser-scanning microscopy

405 nm was used to excite the donor-CFP[181] of FRET biosensor attached to troponin-C calcium binding protein. The emission of FRET signals was captured by spectral detector. The spectral resolution was set to 10 nm.

4.5.7.1 Calcium measurement in axons

The FRET consists of a pair of fluorescent proteins called donor and acceptor. The donor is cerulean derived from cyan fluorescent protein (CFPc) and acceptor is citrine derived from yellow fluorescent protein (YFPc). Troponin-C is a calcium-binding protein. When enough Ca^{2+} ions bind to troponin-C, the resting conformation of troponin-C changes the space between the donor and the acceptor, from cis- to trans- position, bringing them closer to less than 10 nm and generating FRET (Figure 4-2a)[185]. The advantage of laser-scanning spectral microscopy is the ability to directly record the FRET activity, and in turn measure cellular calcium changes. Here, the entire emission spectrum from donor and acceptor fluorescence was imaged with 32-channel detector and the spectrum enabled the measurement of relative FRET efficiency using spectral peak ratio (acceptor divided by donor). Spectral imaging also allows the background to be independent of FRET measurement. For example, a time-lapse calcium imaging of axons with

the treatment of 1 mM glutamate showed that though the baselines of each timepoint were different, their spectral peak ratio are independent of their baseline (Figure 4-2b). The spectral peak ratio can later be processed into emission ratio change (Figure 4-2c). Thus, calcium imaging with laser-scanning spectral microscopy is a powerful way to assess FRET activity.

Due to the possibility of expression instability of the transgene in the transgenic animal[186], FRET activity from CerTN-L15 line was validated *in vitro.* Cell lysate from dorsal column of the transgenic mice was collected and the FRET activity of lysate was excited and measured in cuvette by a 433 nm laser. 10 μM, 1 mM and 25 mM of $CaCl_2$ were added to lysate[187] and the result showed that FRET activities correlated to the concentration of calcium (Figure 4-2c). To deplete calcium *in vitro*, two concentrations of EGTA (6 mM and 25 μM) were added to the lysate containing 1 mM $CaCl_2$. FRET activity dropped to baseline.

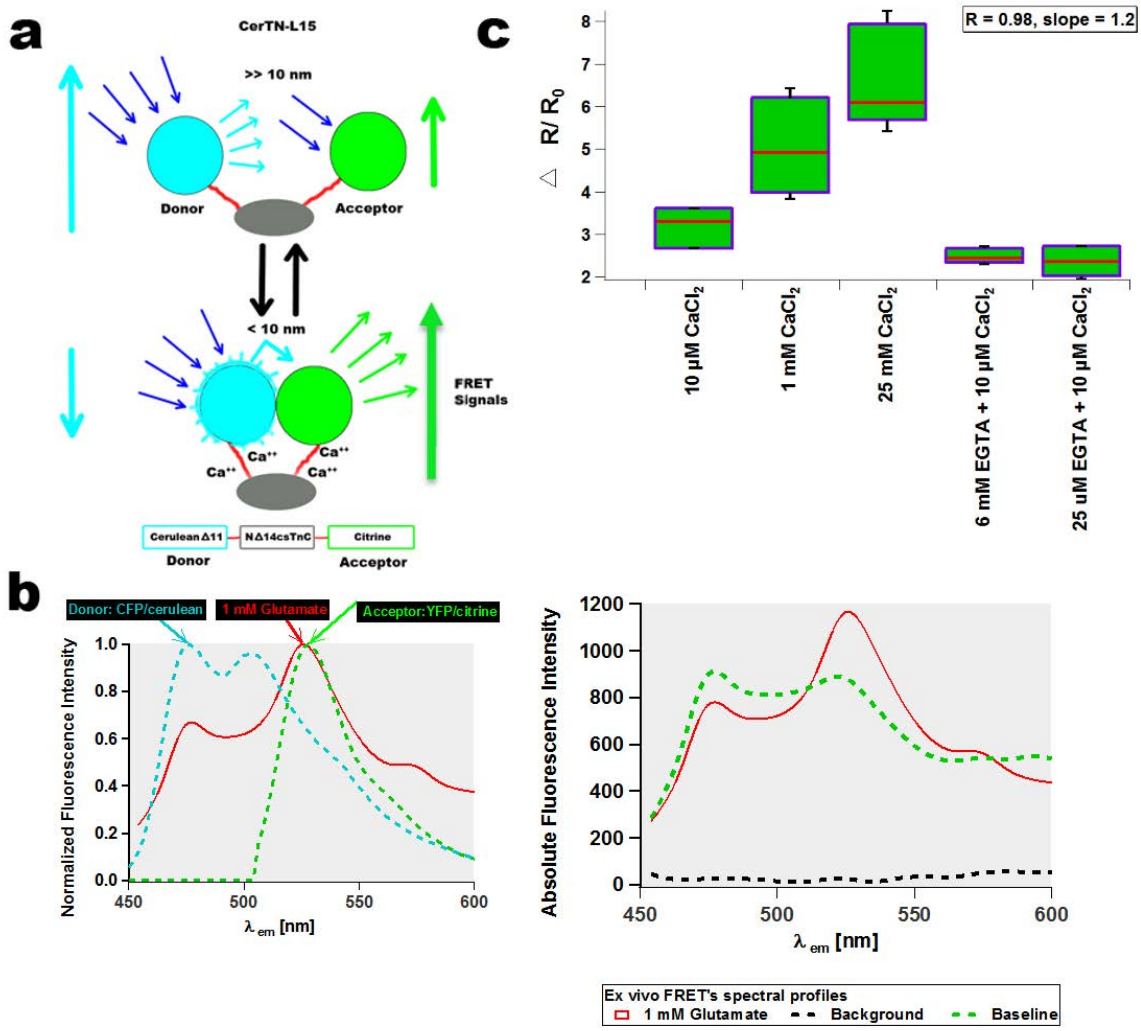

Figure 4-2. Spectral profile of cerTN-L15 mice and *in vitro* validation of FRET activity

a, schematic diagram of interaction between the calcium sensor with FRET detector. FRET occurs when the donor and receptor are in close proximity (< 10 nm). Resonance energy is transferred from the excited donor to acceptor. Acceptor behaves as a quencher of the donor's fluorophore, and emitted light of acceptor[188]. Calcium binding troponin C-based domain (grey) is cloned with FRET pair, sitting between donor and acceptor. FRET pair: donor is cerulean fluorescent protein, improved version of CFP; acceptor is improved version of YFP called citrine. b, (left figure) the individual spectrum of the donor (blue dotted line) and the acceptor (green dotted line) corresponds to the FRET spectrum (red solid line) during calcium rise in *ex vivo* imaging. b, (right figure) FRET before (green dotted

line) and after (red solid line) binding to calcium with its background in absolute intensity. c, *in vitro* quantification of FRET in brain lysate. FRET was detected between 10 μM to 25 mM of $CaCl_2$. When EGTA was added, FRET was diminished. The linear relationship between peak ratio of FRET and concentration of calcium in this study was $Y = 1.23X + 2.36$ with $R = 0.98$.

4.5.7.2 Spectral data analysis

One dimension spectral data were obtained with acquisition software LabView for *in vitro* quantification of FRET study. Excitation laser to generate 433 nm from 866 nm was from coherent Chameleon via doubling Crystal. The data were processed by IGOR for smoothing (algorithm: Binomial with 20). Raw format was converted to 400 points with linear interpolation, normalization, and plotted in IGOR for analysis. For spectral data sampling, all of the spectral data were presented in three animals with two ROIs per animal. For FRET study, ratio of acceptor or donor was used to map FRET efficiency in pseudocolored images with NIS-Element.

4.5.8 Statistical analysis

The analysis of time-lapse studies was performed using IGOR Pro (WaveMetrics Inc., Oregon, CA, USA) with one-way repeated measure ANOVA, followed by Dunnett's post hoc test. Student's t-test was used to compare means of two groups. The significance value of all experiments was taken as $p < 0.05$ ** or $p < 0.001$ ***. N is the number of animals used to repeat the experiment.

4.6 Results

ASF was assessed in spinal cord explant by exposure to glutamate, mild or severe energy deprivation, or a combination, or release of intracellular calcium induced by caffeine treatment.

4.6.1 Baseline assessment of axonal morphology in spinal cord explant

First, I asked how long the intact axons without their cell bodies could maintain their structure in perfused spinal cord explant in oxy-carbonated aCSF at 35°C. I determined the baseline of the

explants by counting the number of ASF over time in normal perfused YFP-tagged axons. The ROIs were collected from the region of superficial fasciculus gracilis in which the areas were at approximately half of the length of the entire explants (≥ 1.2 cm long) and at least 6 mm away from cut end. Minimal ASF was detected during 10 hours of imaging (Figure 4-3a), and only began to occur after 11 hours (Figure 4-3b). This is consistent with previous report in optic nerve explant[189], indicating that the timing of injury in response to the transection was similar in white matter tissues.

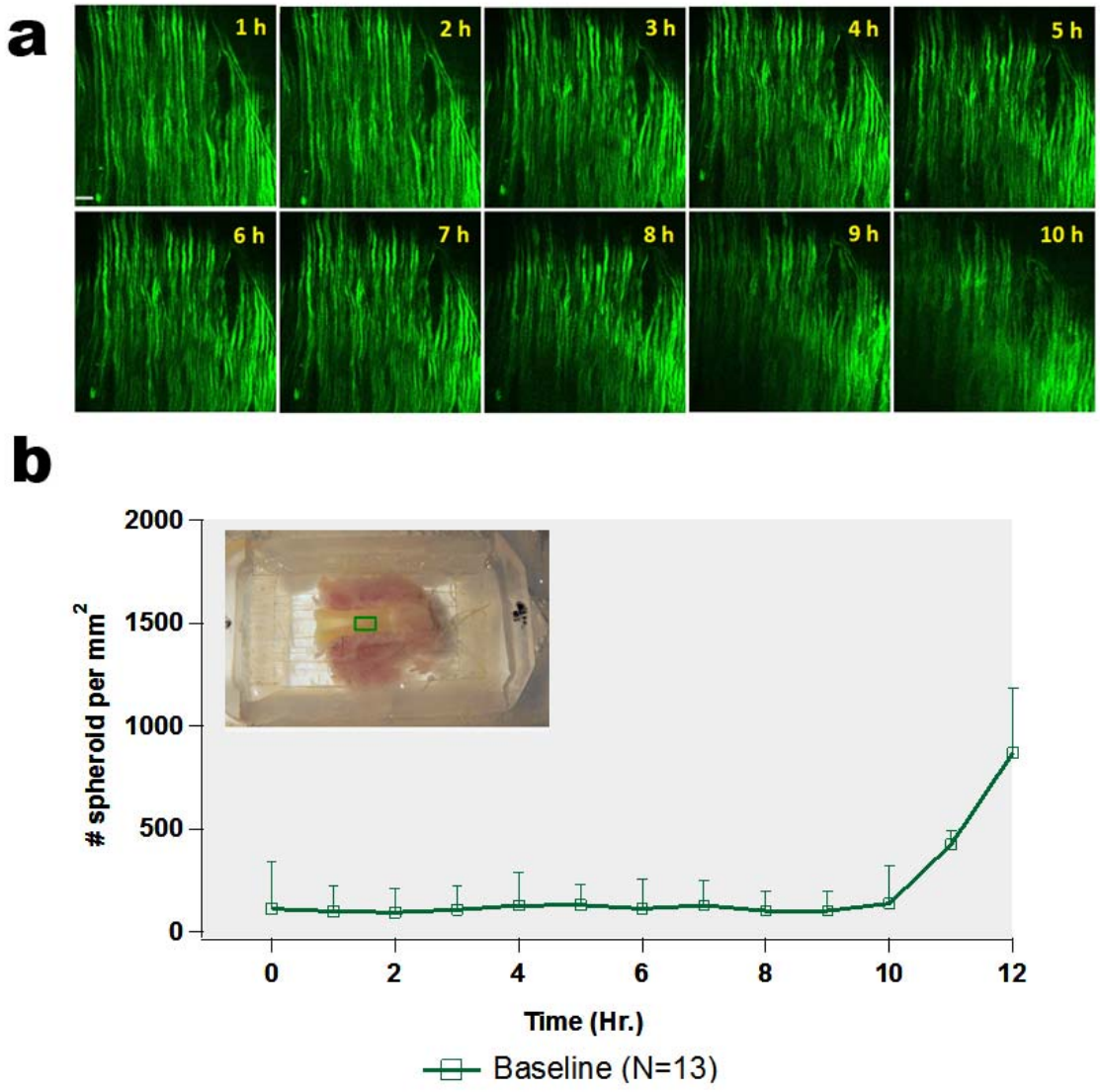

Figure 4-3. Baseline of axon spheroid formation in cervical spinal cord explant

a, two-photon, z-stacks as maximum intensity projection, time-lapse imaging of YFP-tagged axons mice showed that axonal structures were preserved throughout the first 10 hours of imaging. Images are presented as maximum intensity projection. Scale bar = 10 µm. b, number of axonal spheroids (y-axis) were counted over 12 hours (x-axis) in normal perfused explants. The green rectangle in the image is the ROI where spheroids were counted.

4.6.2 Effect of energy deprivation

I next assessed the effect of energy deprivation in white matter for the following reasons. Firstly, the function of white matter is adversely affected during energy deprivation[170,190–192]. Thus, I considered this as positive control for my experiment. Secondly, energy deprivation induced white matter injury accompanies glutamate release[52,174,193]. Disruption of ionic homeostatic concentration due to the loss of function in Na^+/K^+ ATPase pump led to glutamate release via reverse Na^+ dependent glutamate transporter[174]. Aberrant depolarization due to uncontrolled Na^+ influx activated ionotropic glutamate receptors and calcium permeable AMPA receptors would cause calcium release[170]. Thirdly, demyelinated axons demand high energy to maintain their ion gradients via Na^+/K^+ ATPases[24], chronically stressing the mitochondria, leading to sodium channel-mediated axonal injury and glutamate release from immune cells including microglia and/or macrophages[176,194–196], and astrocytes[175,197]. Taken together, these resulted in death of myelinating oligodendrocytes[198,199]. To mimic the effect of energy deprivation, sodium azide (NaN_3) was used to inhibit mitochondrial cytochrome oxidase complex IV[200]. It has been used to induced ASF in the PNS[201] and axonal injury *in vitro*[202]. Two mM of NaN_3 was applied in perfusion. ASF was observed within one hour of perfusion (Figure 4-4a), and it was robustly induced after 3 hours of treatment (Figure 4-4b, $p < 0.001$, $N = 3$).

These results agree with previous study on corpus callosum slice using chemical ischemic method: oxygen-glucose deprivation and reperfusion (OGD)[169]. ASF was observed after 3 hours of reperfusion whereas ASF was observed after one hour using NaN_3 treatment. This indicated that either NaN_3 is more potent than OGD reperfusion or dorsal column is more vulnerable than

corpus callosum to energy deprivation-mediated injury. It is also possible that the mechanism of anoxia is different from ischemia.

After confirming the positive result, I applied high concentration of glutamate (10 mM). This concentration has been reported to cause excitotoxicity in spinal cord injury[203]. Surprisingly, the effect of 10 mM glutamate was not as robust as NaN_3 alone (Figure 4-5). To reach the peak of ASF formation, glutamate alone took 10 hours while NaN_3 took less than 3 hours. ASF was delayed. However, combined NaN_3 and low concentration of glutamate with the concentration of 2 mM and 0.2 mM respectively significantly increased the number of ASF (Figure 4-6, $p < 0.005$, $N = 3$). I concluded that axons are quite resistant to even higher concentration of excitotoxins provided that they are energy replete.

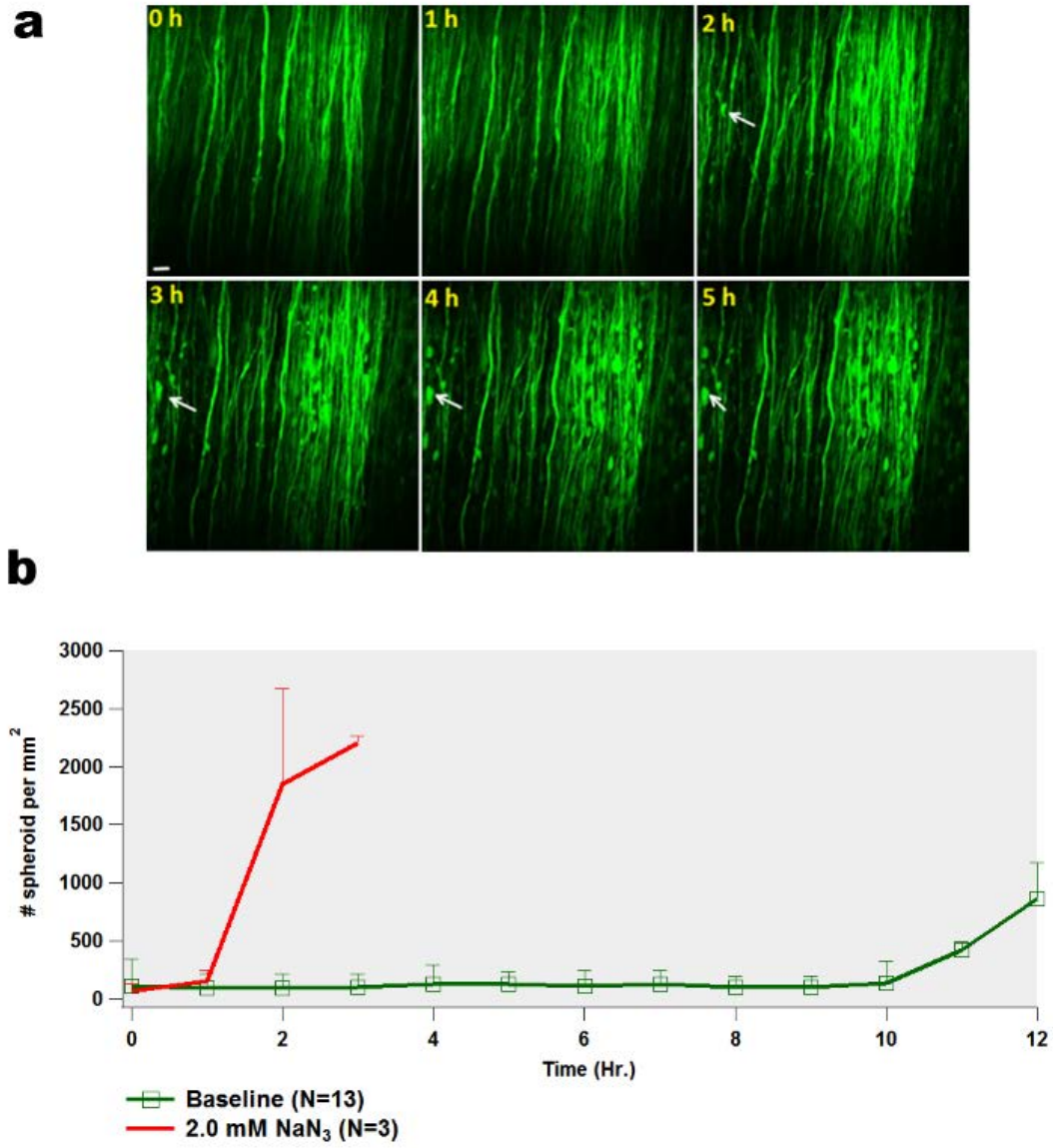

Figure 4-4. Chemical anoxia induced extensive axon spheroid formation

a, ASF was induced by 2 mM NaN_3 for 5 hours. After 2 hours, spheroids were observed (arrow). After 3 hours, transection occurred (arrow). b, quantification of axonal spheroids in ischemic condition compared to baseline. After one hour of treatment, spheroids started to form. After 3 hours, the number of spheroids were too numerous to count.

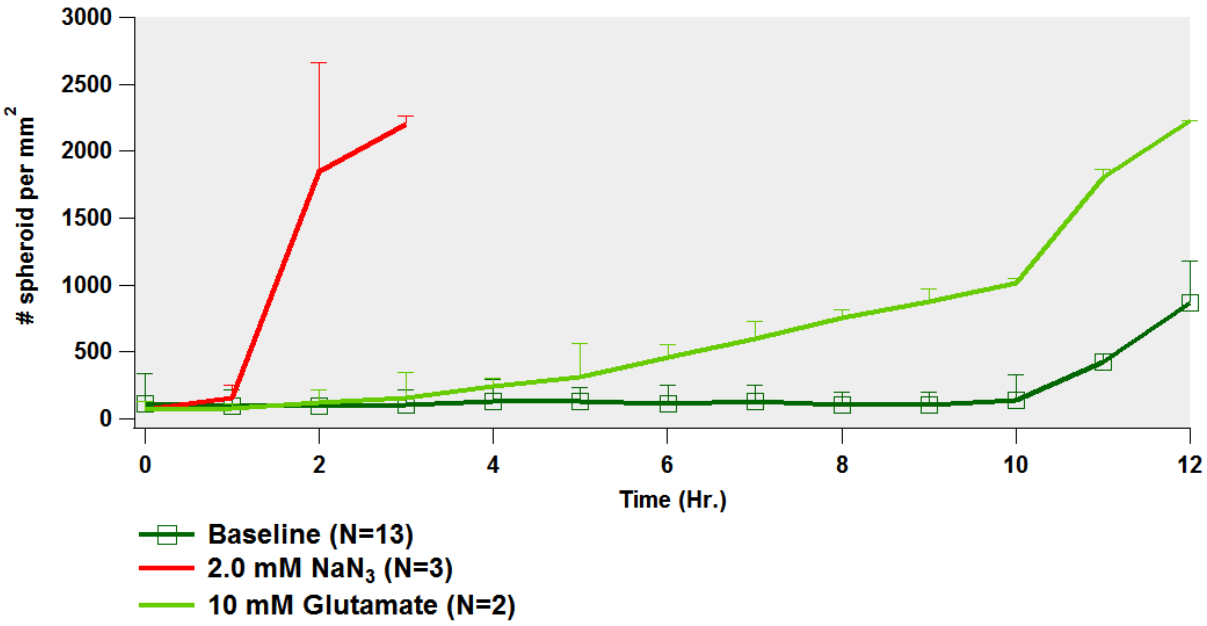

Figure 4-5. High concentration of glutamate delayed spheroid formation

10 mM glutamate exhibited modest effect of ASF by comparing to chemical anoxia. Number of spheroids in 2 mM NaN_3 treatment were too numerous to count after 2 hours whereas number of spheroids in 10 mM glutamate treatment only started to increase after 7 hours.

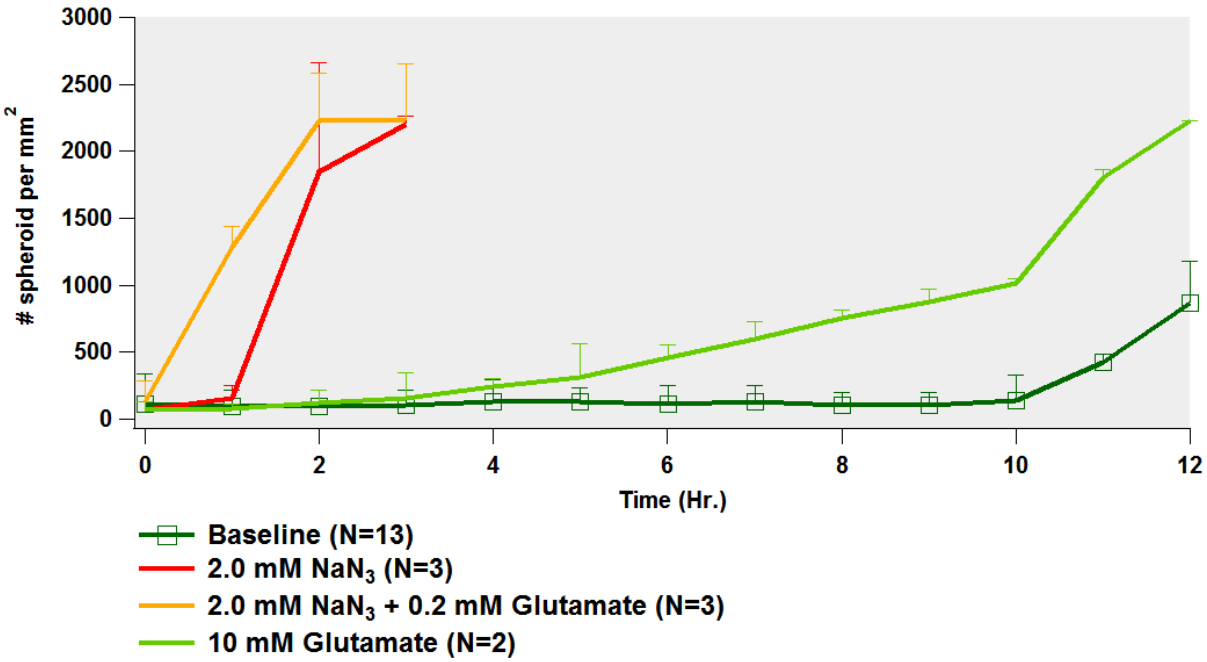

Figure 4-6. Low concentration of glutamate induced ASF in chemical anoxia

Combined treatment of 0.2 mM glutamate and 2 mM NaN_3 induced ASF even faster than 2 mM NaN_3 treatment alone, suggesting energy deprivation facilitates the effect of glutamate-mediated excitotoxicity.

Conversely, use of low concentration of 0.5 mM NaN_3 or combination of 0.5 mM NaN_3 and 0.2 mM glutamate did not generate ASF (Figure 4-6). Interestingly, with low concentration of NaN_3 plus high concentration glutamate induced very robust spheroid formation (Figure 4-7). I concluded that when axons are only modestly deprived of energy, they become exquisitely sensitive to excitotoxicity, even more so than with severe chemical anoxia alone.

The effect of glutamate-mediated excitotoxicity itself might have been altered by other cellular activities in the explant. For example, axons[204] and astrocytes[84] might uptake the glutamate. To address this, 0.5 mM TBOA with 10 mM glutamate was tested in perfused explants. TBOA has proven to be a potent blocker for glutamate uptake[205,206]. Increase in ASF was observed, indicating that the activity of glutamate uptake was inhibited (Figure 4-8). It seems that astrocytes might still be functional in explants, and presumably extracellular glutamate was absorbed by astrocytes' glia limitans in subarachnoid or perivascular space[207].

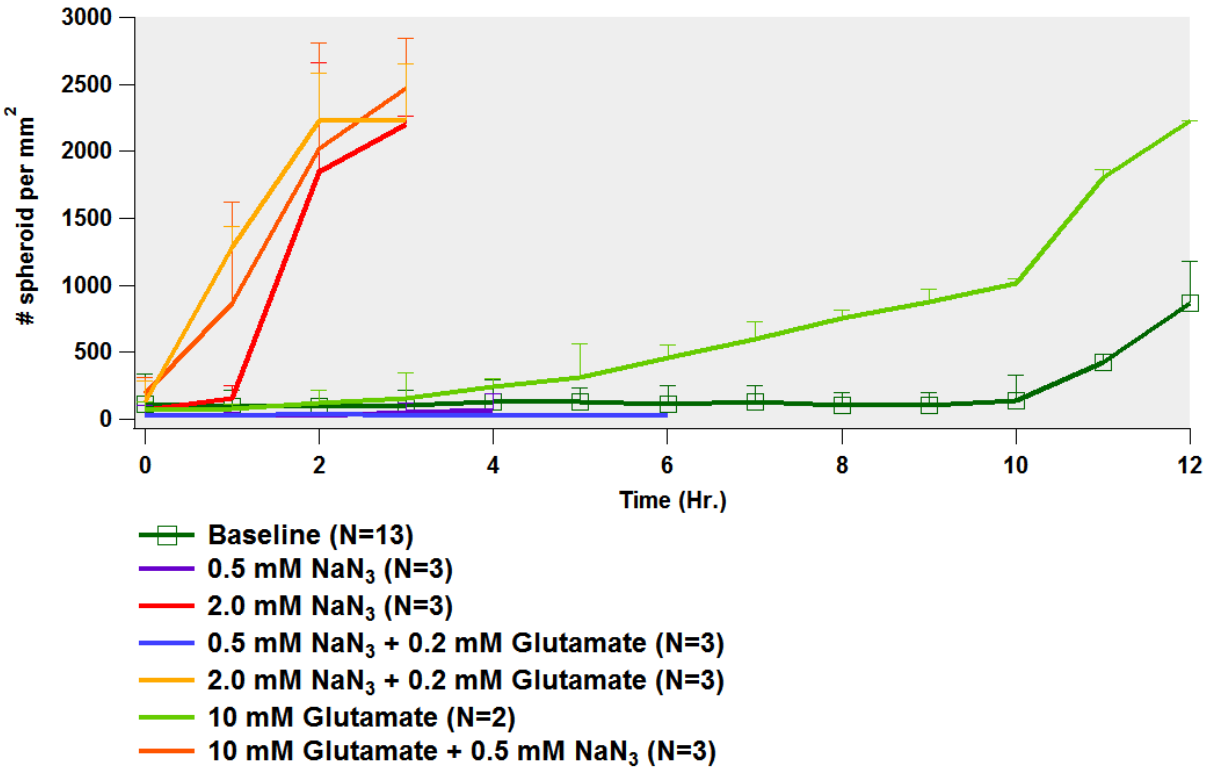

Figure 4-7. High concentration of glutamate induced ASF in mild chemical anoxia

The treatment of 0.5 mM NaN_3 with 10 mM glutamate induced more ASF than chemical anoxia alone (2 mM NaN_3), indicating mild disturbance of cellular energy could disrupt the neutralization of glutamate-mediated excitotoxicity. Negligible ASF was observed in the treatment of low concentration of NaN_3 alone. Adding 0.2 mM glutamate to low concentration of NaN_3 also did not generate ASF, indicating there is a toxicity threshold for the induction of ASF.

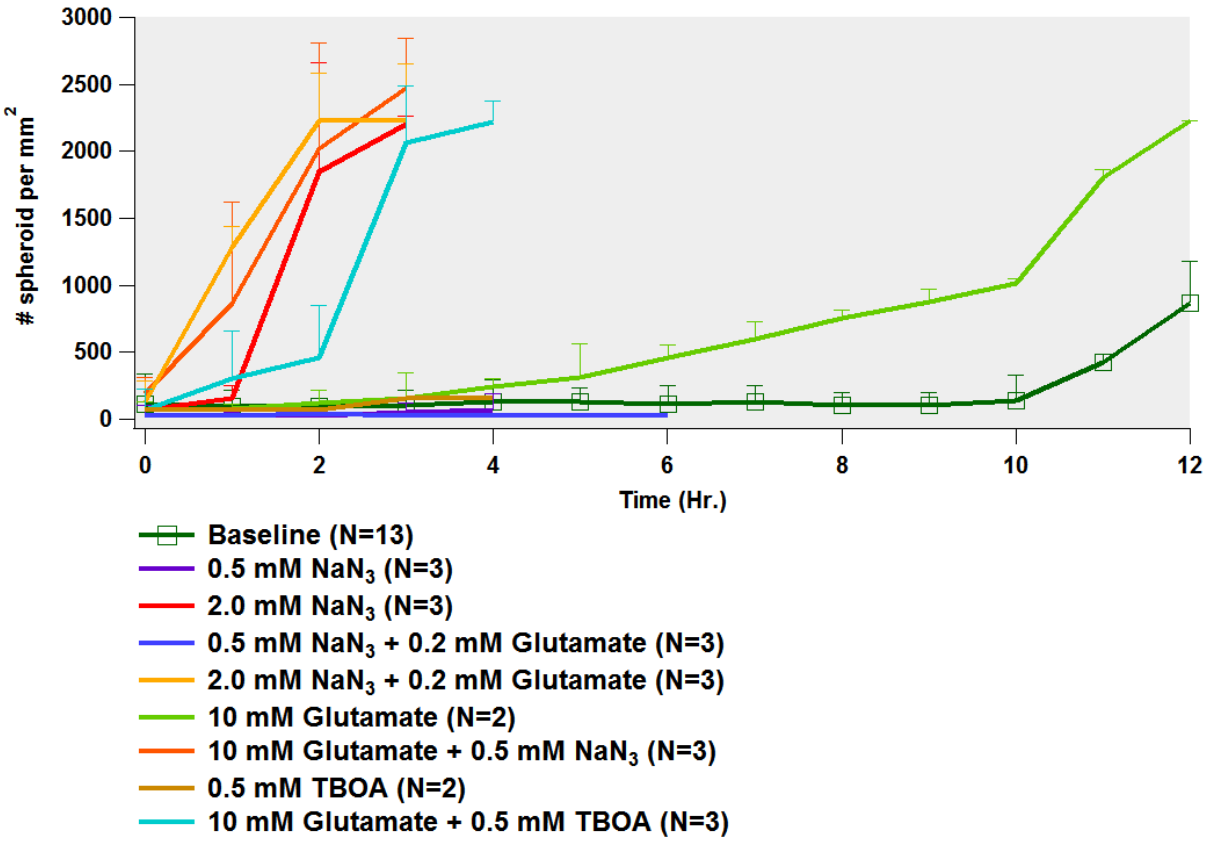

Figure 4-8. The neutralization of glutamate-mediated excitotoxicity was blocked by TBOA

TBOA as the blocker of glutamate transporter was added to the 10 mM glutamate treatment. ASF was generated faster than 10 mM glutamate alone, suggesting glutamate was actively transported and the toxicity was neutralized by the cellular glutamate transporters in the energy-replete explant.

Finally, I tested all three agents (TBOA, NaN_3 and glutamate). The combined agents are to mimic the pathological conditions in MS. I observed the fastest responses of ASF among the treatments without using high concentration of NaN_3 (Figure 4-9, $p < 0.005$, $N = 2$). The data indicated that lower concentration of NaN_3 created the effect of virtual hypoxia[24,139,208], TBOA altered glutamate uptake[176] and addition of glutamate induced the condition of excitotoxicity[129,140].

In summary, treatment with high concentration of glutamate alone and low concentration of NaN_3 alone did not induce early spheroid formation (Figure 4-10). Adding TBOA with glutamate generated more spheroids than glutamate alone, indicating robust glutamate uptake into axon or other glial cells. This activity is also associated with energy deprivation. Indeed, a report showed the effect of glutamate uptake quickly ceased in organotypic hippocampal brain slice during energy deprivation[193].

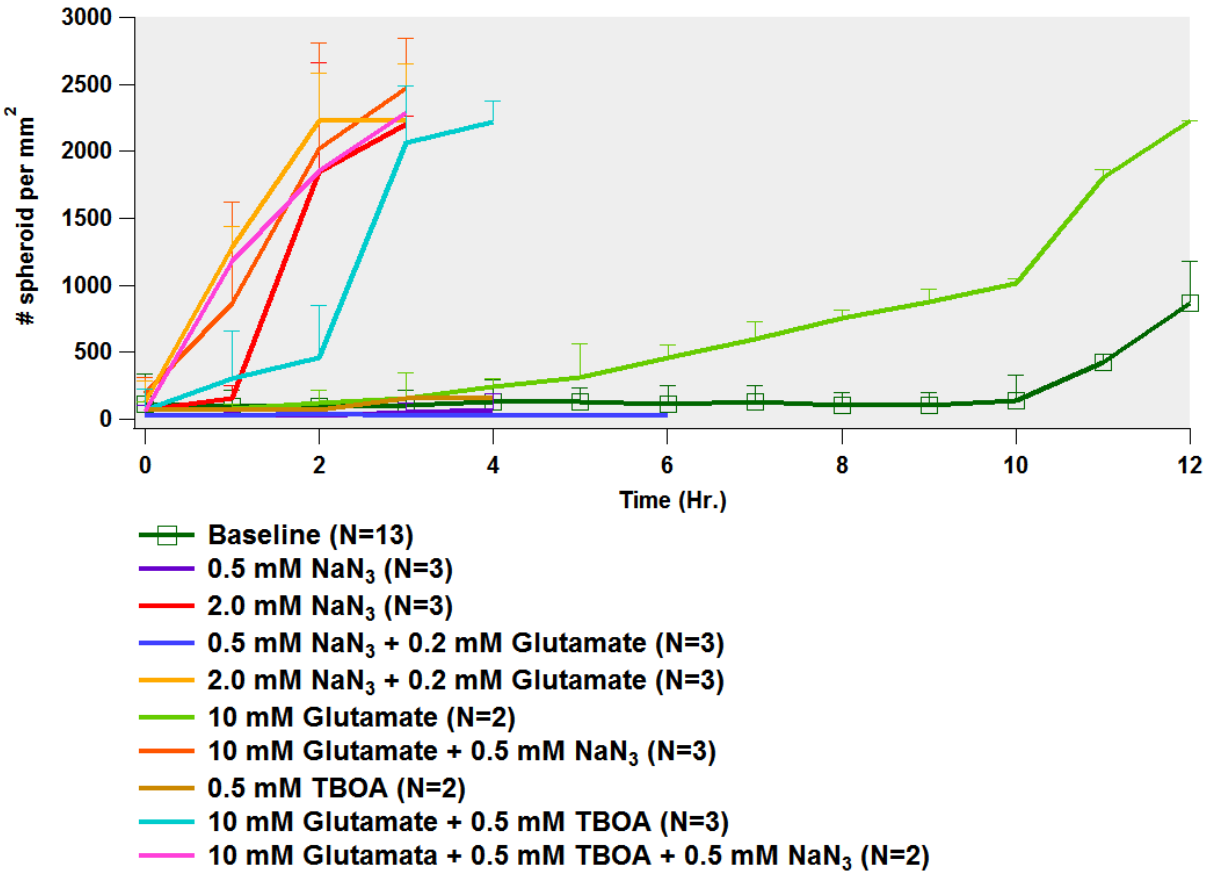

Figure 4-9. Mimicking the pathological condition in MS

Low concentration of NaN_3 was combined with TBOA and glutamate to mimic the pathological condition in MS. Within one hour, a fourfold increase in spheroids was generated compared to TBOA and glutamate, suggesting the pathological environment can be induced in *ex vivo* dorsal column.

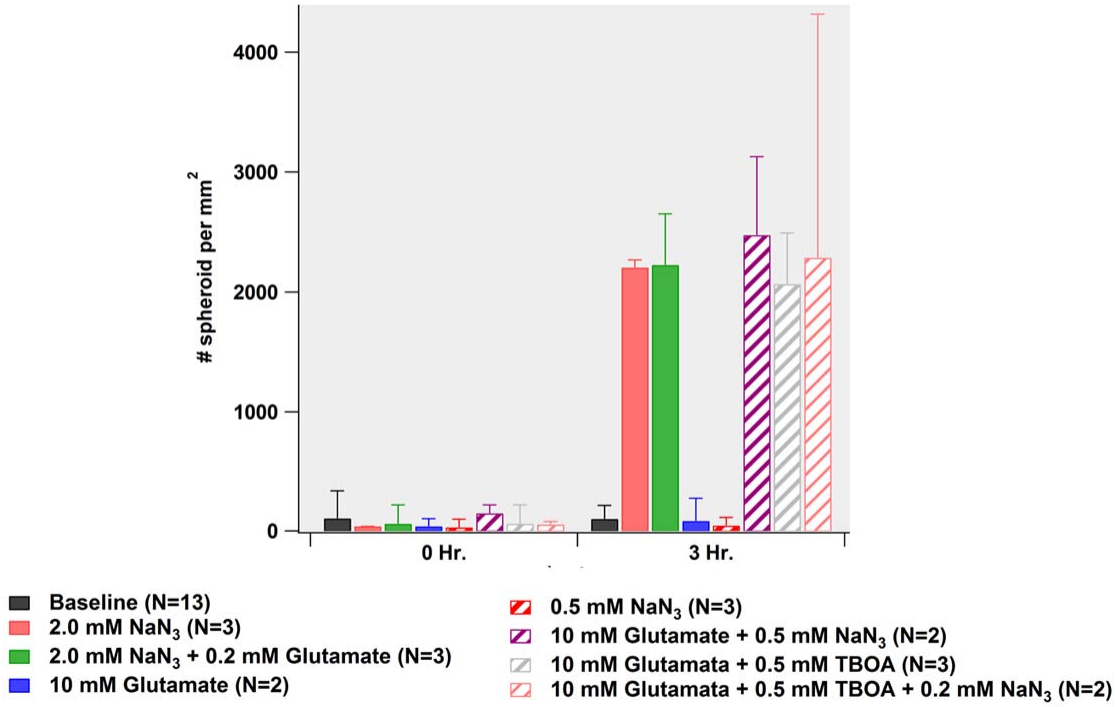

Figure 4-10. Summary of interplay between glutamate-mediated excitotoxicity and energy deprivation-mediated ASF

High concentrations of glutamate did not induce spheroids. Adding either low concentration of NaN_3 or TBOA in high concentration of glutamate induced ASF. Low concentration of NaN_3 did not induce spheroids. High concentration of NaN_3 alone induced ASF. Adding low concentration of glutamate in high concentration of NaN_3 induced about the same numbers of spheroids as high concentration of NaN_3 alone. Combined TBOA, NaN_3 and glutamate also induced significant amount of spheroids.

4.6.3 Glutamate-mediated excitotoxicity induced ASF

Although glutamate-mediated excitotoxicity seems to play a secondary role in the mechanism of ASF, combined TBOA and glutamate induced much more extensive and rapid pathology than glutamate alone (Figure 4-8), indicating that cellular uptake was responsible for the neutralization of glutamate-mediated excitotoxicity. Astrocytes might be responsible for the neutralization of glutamate-mediated excitotoxicity[209–211]. Astrocytes monitor the ionic homoeostasis including glutamate[212]. In additional, the diffusion barrier of subarachnoid mater and pia mater in spinal cord[18,207,213,214] (Figure 4-11) may also be responsible for the surprisingly modest effect of glutamate-mediated excitotoxicity by slowing down the diffusion rate of glutamate on the axons, this phenomenon has been reported in brain slices[206]. To address this issue, collagenase was used to digest the collagen in glia limitans with pia meter[215]. SHG microscopy was used to study collagen distribution and enzymatic activity of collagenase.

The collagenase application was effective in removing glia limitans with negligible toxicity (Figure 4-12). Controls treated with collagenase induced limited ASF (N = 4, imaging for 10 hours with < 1% of ASF) while glutamate induced robust ASF ($p < 0.001$ at 3 hours, N = 6, imaging for 7 hours with > 98% ± 0.5 of ASF) (Figure 4-13). A tenfold lower concentration of glutamate induced injury twice as fast. To test the specificity of glutamate-mediated excitotoxicity, glutamate antagonists - KA was applied. Three different treatments were tested: 1 mM glutamate alone; 1 mM KA with 1 mM of glutamate and 1 mM KA alone. KA inhibited ionotropic glutamate receptors significantly compared to 1 mm glutamate alone ($p < 0.001$, N = 4). The number of spheroids in KA alone compared to the combined KA with glutamate was also significant (Figure 4-14, $p = 0.05$, N = 4), indicating that sub-population of axons was not

protected by KA; this unprotected population might be the metabotropic glutamate receptors[33]. Nonetheless, the results suggest that the effect of ASF is specific to the injury mechanism of glutamate-mediated excitotoxicity.

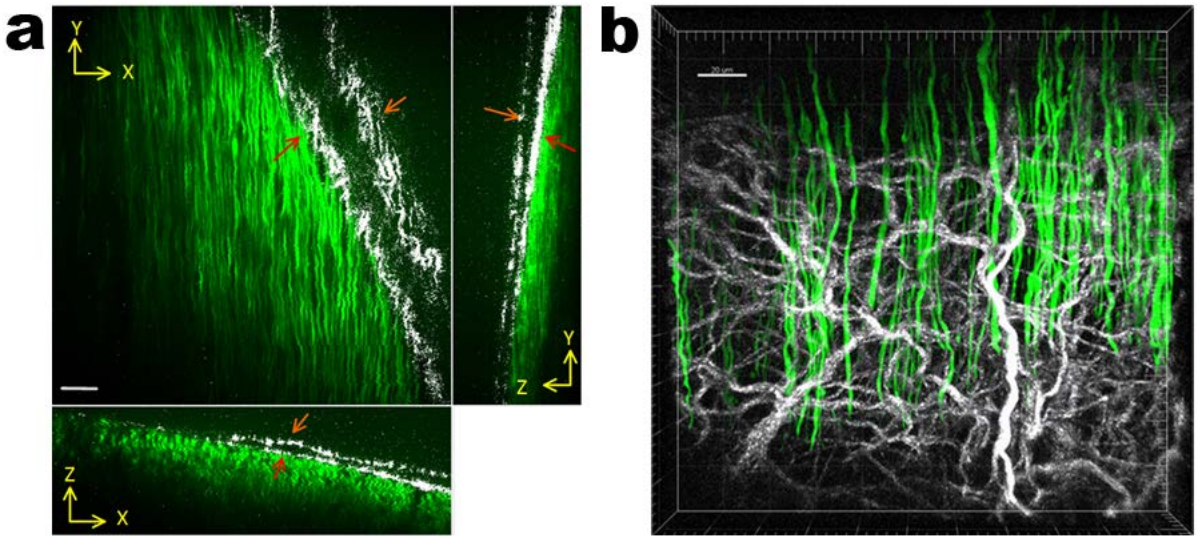

Figure 4-11. 3D SHG imaging revealed subarachnoid space and pia mater in dorsal column

a, SHG imaging with 20 μm-thick layer in dorsal column with a depth of 0.5 μm. XY image of collagen (white) and axons (green) showed the distribution of pia mater (red arrow) and subarachnoid space (between red and orange arrow). YZ and XZ images indicated by arrows showed the orientation of subarachnoid space and the superficial dorsal column wrapping by the pia mater. Scale bar = 10 μm. b, spatial resolution of collagen and pia mater was shown in maximum intensity projection. Scale bar = 20 μm

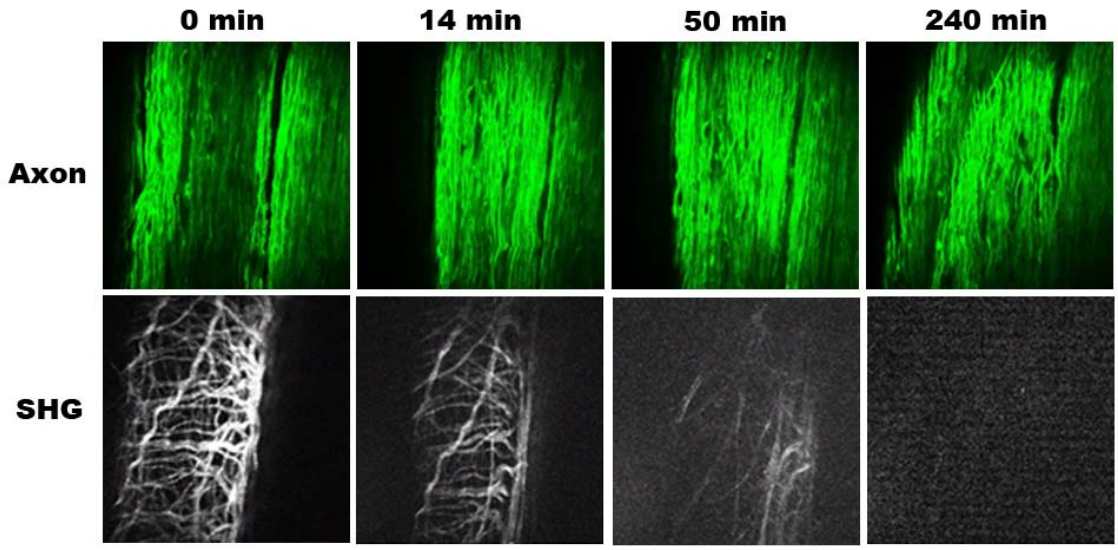

Figure 4-12. 3D time-lapse SHG imaging of collagen breakdown by collagenase in spinal cord explant

Each image contains a set of optical volume with 20 μm thickness and presented in maximum intensity projection. Top panel, axons (green) were not affected by the treatment of collagenase. The collagen structures (white) were digested by collagenase and eventually became undetectable by SHG imaging after 4 hours.

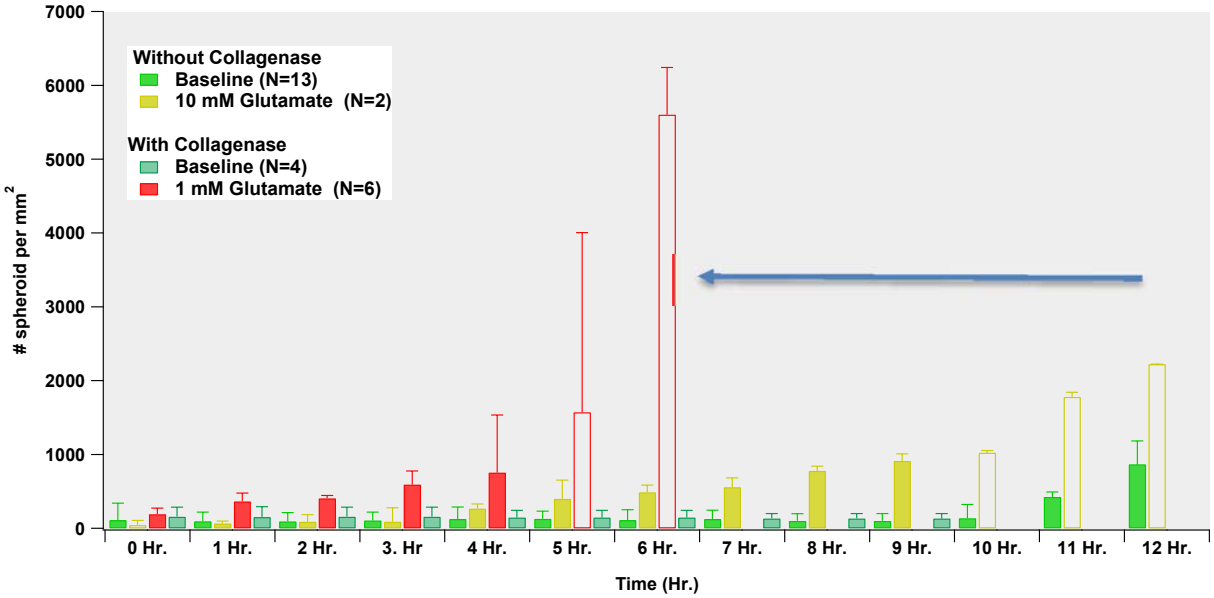

Figure 4-13. Glutamate-mediated excitotoxicity robustly induced ASF after the breakdown of diffusion barrier in spinal explant by collagenase

Two groups of spinal cord explants were used: with collagenase treatment and without collagenase treatment. Spinal cord explant with collagenase treatments were divided into two subgroups: control and 1 mM glutamate treatment. Spinal cord explant without collagenase treatments were also divided into two subgroups: control and 10 mM glutamate treatment. Spheroids formed after 7 hours of perfusion in spinal cord explant treated with 10 mM glutamate (without collagenase). Spheroid formation was observed as early as 2 hours in spinal cord explant treated with 1 mM glutamate (with collagenase).

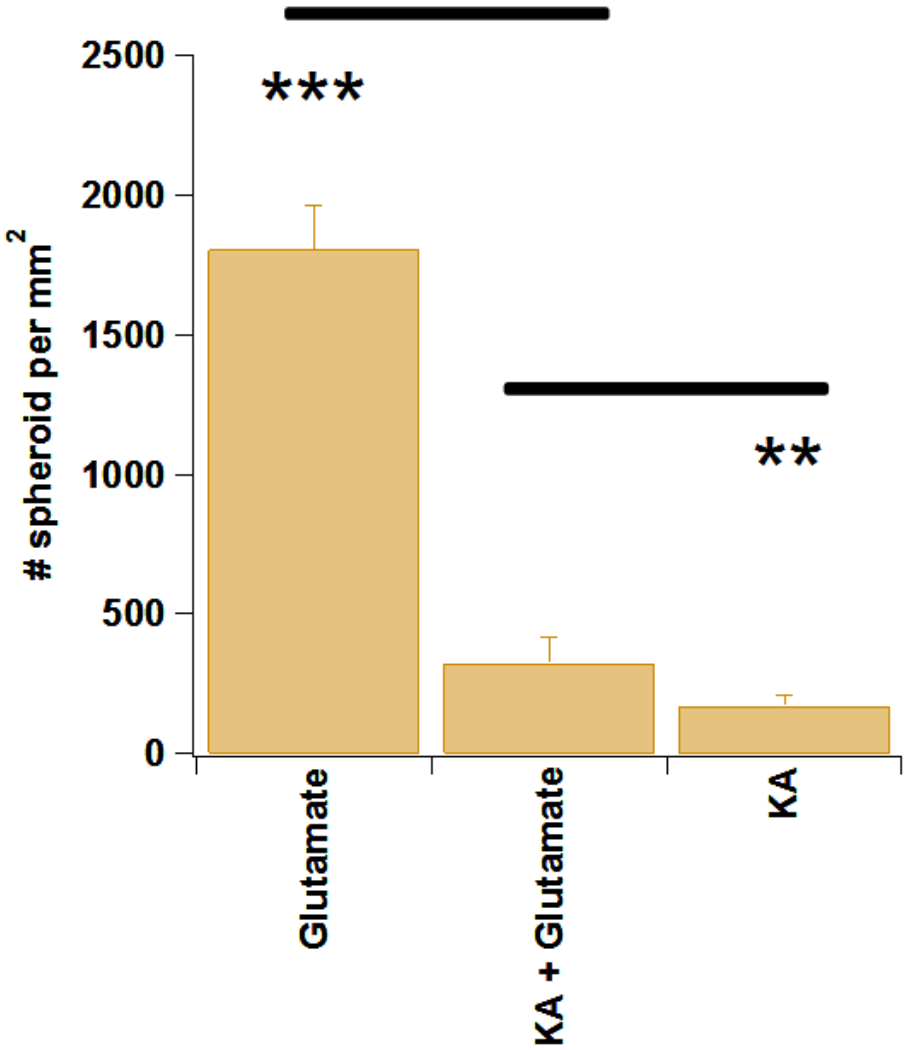

Figure 4-14. The excitotoxicity is due to the overactivation of ionotropic glutamate receptors

All the spinal cord explants were treated with collagenase. The explants were then incubated with 1 mM of glutamate, 1 mM of KA + 1 mM of glutamate, and 1 mM KA, fixed and counted after 5 hours (3 mice per group). KA alone was the control. Blocking the activation of ionotropic glutamate with KA significantly reduced ASF. $p < 0.05$ ** or $p < 0.001$ ***.

4.6.4 Calcium rise preceded ASF after glutamate treatment

The role of calcium in axonal injury by glutamate-mediated excitotoxicity has been studied[32,33], however ASF and transection has not been directly linked to this pathway, which is my underlying hypothesis. To determine whether activation of glutamate receptor induces calcium rise which was responsible for subsequent ASF and transection, live calcium imaging using transgenic mice expressing FRET-based calcium sensor troponin-C (cerTn-L15) was performed. Collagenase treatment was applied to remove diffusion barrier, FRET activity was measured during 1mM glutamate treatment from three transgenic mice. Within two hours, significant amount of calcium was detected in the axons (Figure 4-15a, $p < 0.05$, $N = 3$). This data are in agreement with others using exogenous calcium dyes to measure calcium activity[32,33]. Axons subsequently transected after 3 hours of treatment (Figure 4-15b).

In summary, the experiments support my hypothesis that axonal calcium rise during glutamate-mediated excitotoxicity. Calcium influx via over-activated glutamate receptors lead to focal ASF.

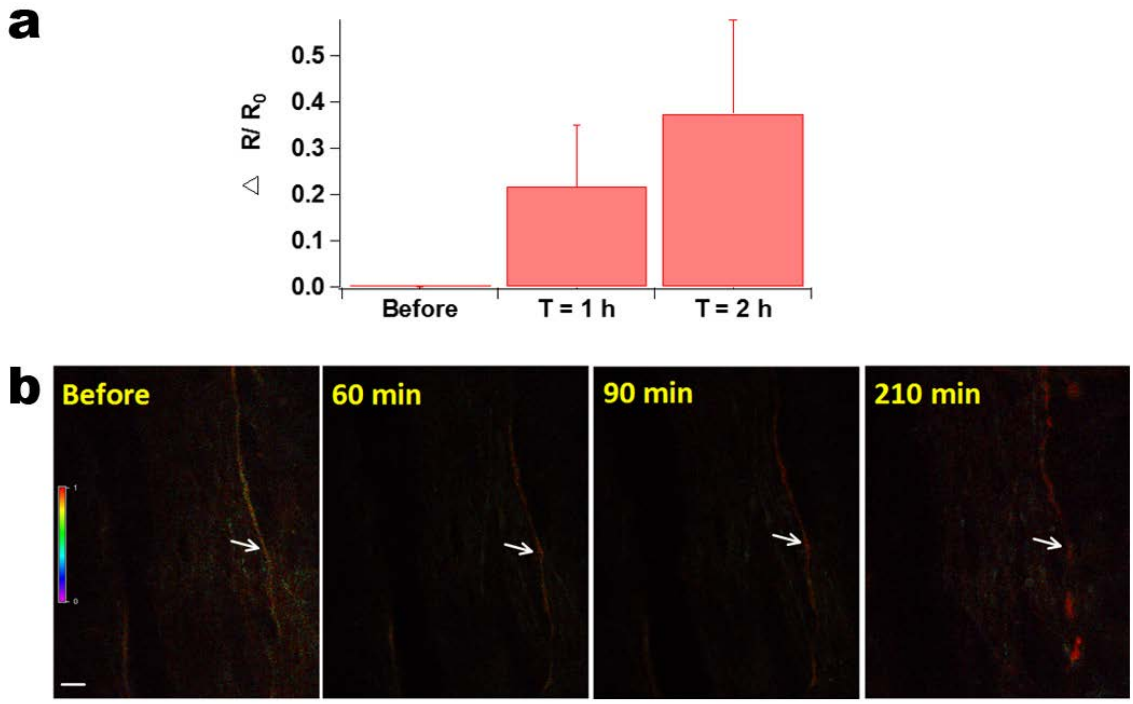

Figure 4-15. Calcium rise preceded axonal swelling and transection during glutamate treatment

a, the bar graph shows average calcium activity within two hours after glutamate treatment in collagenase treated dorsal column ($p < 0.005$, $N = 3$). b, pseudocolor ratio (acceptor over donor) images at four different time points over the course of glutamate treatment. At 60 minutes, calcium rise was detected in a axon (white arrow). At 90 minutes, the intenisty of FRET increased and after 210 minutes, ASF and trasection. Scale bar = 10 μm

4.6.5 Intracellular calcium release induced ASF

In most of the glutamate experiments, I frequently observed dark puncta devoid of YFP (Figure 4-16). Using deconvolution methods, I clearly showed that the submicron puncta were adjacent to the inner surface of axolemma (Figure 4-17). Previous studies showed that intracellular calcium release via overactivation of ryanodine receptors contributes to axon injury via axoplasmic reticulum (AR)[117]. AR has been shown in axon[216] and it is one of the largest axonal calcium storage organelles[217]. Intracellular calcium release may have caused reticulum stress[218], resulting in osmatic changes inside AR[219,220] and induced the submicron puncta. To address this, caffeine was used to release calcium through ryanodine receptors in YFP-tagged axons transgenic mice. Caffeine induced spheroids robustly compared to glutamate treatment (Figure 4-18, $p < 0.001$ at 1 hour, $N = 3$) and submicron puncta and micron puncta were observed (Figure 4-19).

Next, I applied ryanodine as an antagonist to block the ryanodine receptor and ASF decreased significantly (Figure 4-18). Using caffeine to induced ASF was more robust than glutamate, indicating intracellular calcium source was more potent than extracellular calcium. This was further demonstrated by the combination of glutamate and ryanodine treatment in which ASF was minimal. This study is in agreement with previous report using caffeine to induce spheroid formation in optic nerve[221].

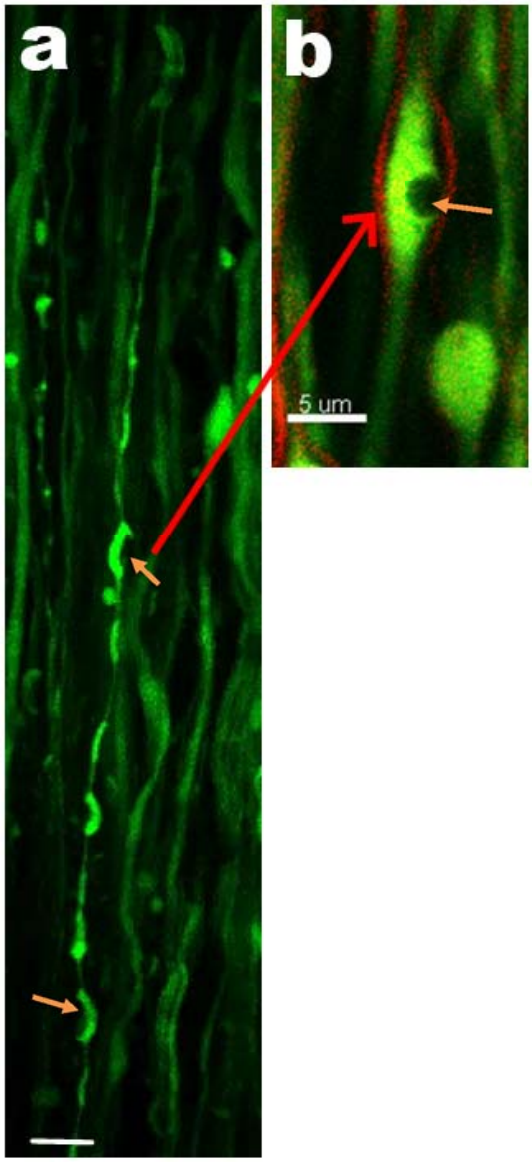

Figure 4-16. Dark puncta devoid of YFP found in the treatment of glutamate

a, glutamate-mediated excitotoxicity induced some spheroids partially devoid of YFP (orange arrow). Scale bar = 10 μm. b, magnification of a spheroid showing the exclusion of YFP (orange arrow). The myelin was stained by NR to demonstrate that the devoid of YFP was not part of the myelin sheaths.

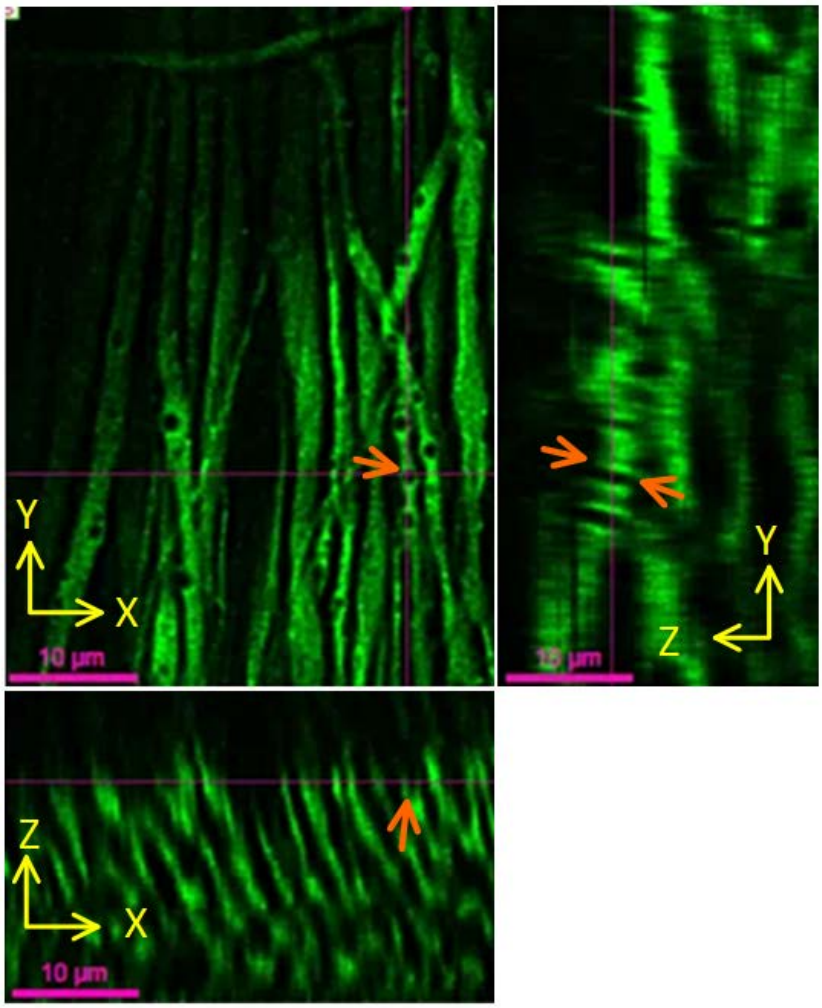

Figure 4-17. Submicron puncta formation during glutamate-mediated excitotoxicity treatment

Deconvolved images of axons showing submicron puncta after glutamate treatment. 3D imaging of a 20 µm-thick layer in dorsal column with a depth of 0.5 µm. A Z-stack image shows the location of submicron puncta along the lines in axons. YZ and XZ images along the corresponding lines indicated by arrows show the submicron puncta contact the inner surface of axolemma. These submicron puncta were examined using adaptive blind deconvolution.

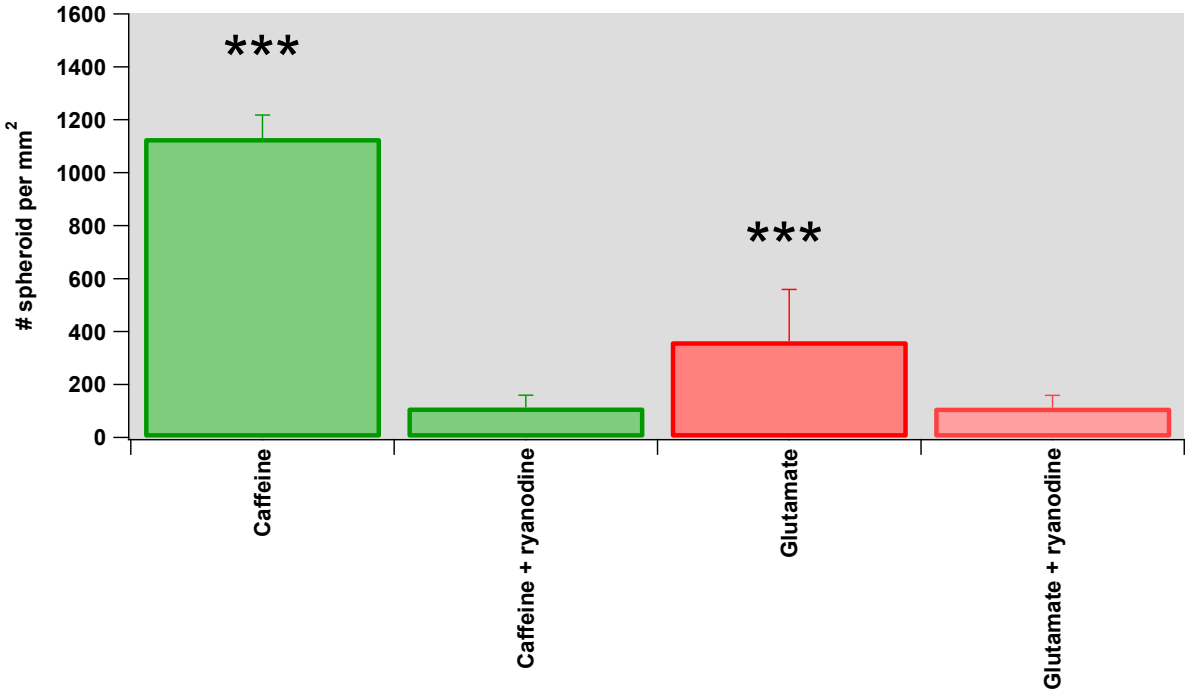

Figure 4-18. Caffeine-mediated intracellular calcium release induced ASF

Ex vivo dorsal columns were perfused in 4 different treatments: caffeine, caffeine with ryanodine, glutamate, glutamate with ryanodine. Ryanodine receptors were activated by caffeine promoting ASF, while caffeine with ryanodine treatment inhibited ASF. Glutamate treatment showed less than 50% of ASF by comparing to caffeine treatment. Combination of glutamate with ryanodine blocked ASF as well. $p < 0.001$ ***, $N = 3$.

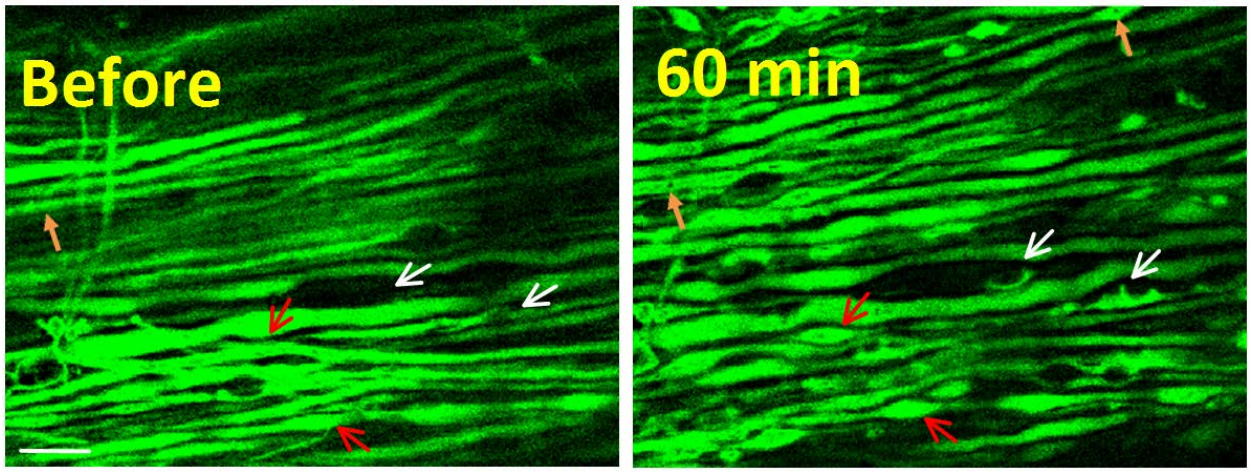

Figure 4-19. Caffeine induced ASF via intracellular calcium rise

Ex vivo spinal cord explant expressing YFP in axons treated by caffeine. Before caffeine treatment, there was absence of puncta in axons. After 60 min of caffeine treatment, puncta (white arrows) and submicron puncta (orange arrows) were detected. Red arrows indicate swollen axon without appearance of puncta. Scale bar = 10 µm

4.7 Discussion

4.7.1 Glutamate-mediated excitotoxicity in axonal injury

The results confirm and expand the findings of previously reported studies[13,32,33] in that I demonstrate that non-traumatically induced ASF and transection in central white matter are caused by glutamate-mediated excitotoxicity and the disruption of calcium homeostasis. During white matter injury via glutamate-mediated excitotoxicity, two key events have been reported: axonal calcium rise[32,33] and decreased compound action potential[13]. However, these events are insufficient to define irreversible axonal injury. ASF and transection is a major pathological process in MS, the result of irreversible axonal injury that causes permanent clinical disability. Here, my results show axonal calcium rise during glutamate-mediated excitotoxicity, followed by ASF and axonal transection, a cellular mechanism of white matter injury that might reassemble the progression of axonal pathology in MS. Axonal spheroids were induced in the absence of immune cells. Thus, axonal injury might support the hypothesis of cytodegeneration as a pathogenesis in MS. Unlike the conventional hypothesis of pathogenesis ("outside-in"), axons are the primary target of insults by cellular injury mechanism found in neurodegenerative disease, e.g. Alzheimer's disease, disruption of calcium homeostasis in axon[222]. In light of this, these axonal spheroids found in MS[9] can be viewed as the result of axonal degeneration rather than a secondary injury to axons from the inflammatory reaction. Even if the conventional hypothesis is true, immune cells have been shown to release glutamate at the lesion. Glutamate-mediated excitotoxicity might still be an important destructive mechanism in demyelinated axons within inflammatory lesions. Hence, blocking the overactivation of glutamate receptors could be a significant implication for the treatment of progressive MS by using glutamate antagonist such as KA to alleviate axonal degeneration.

4.7.2 The morphological behavior of axonal spheroids in intact spinal cord explant

Using *ex vivo* imaging model of spinal cord explant from several kinds of transgenic mice, ASF were found from energy deprivation-mediated axonal injury, glutamate-mediated excitotoxicity and caffeine-mediated calcium rise. Axon population is not uniform in response to these treatments. Certain axons appeared normal during the treatments while others deteriorated badly.

Transgenic mice expressing YFP have been widely used to study Wallerian degeneration[29,81,189,223,224] and energy deprivation[169,177], yet ASF with dark puncta devoid of YFP had not been reported and may involve ryanodine receptor activation in AR. These dark puncta were mainly observed in caffeine treatments, and glutamate-mediated excitotoxicity. The area of black voids could be the organelle swelling and AR might be a good fit to explain this phenomenon. This spheroid is devoid of YFP, indicating the YFP is blocked by the membrane of the organelle. The black voids appear distinctly intra-axonal, therefore they must be intra-axonal organelles. Among the organelles, axonal mitochondria and AR are most likely to cause such phenotype. The morphology of axonal mitochondria are elongated and not circles as shown in Figure 3-6j. Therefore, I argue that this phenotype is less likely mitochondria and more likely AR. AR is the largest single intracellular organelle[225] and a continuous endomembrane structure from the cell body[216,217], containing significant calcium stores[226,227]. In electron microscopy study, axonal AR is commonly located under the axolemma in close apposition[216], precisely where this phenotype appears to be located (Figure 4-16). Furthermore, using an inhibitor to block endoplasmic reticulum stress resulting lesser glutamate-mediated excitotoxicity, this also prevents the conformational changes of endoplasmic reticulum (ER) in rat brain[228]. Elevation of intracellular calcium that alters endoplasmic reticulum morphology has also been reported in cell

culture[229]. Thus, these notions might support my *ex vivo* data: using caffeine to induce calcium rise via activation of ryanodine receptors in AR (Figure 4-18). The swelling of ER might due to an increased osmotic pressure caused by an inward ionic current while releasing calcium.

4.7.3 The swelling of periaxonal space vs. axoplasmic reticulum

The partial exclusion of YFP from some swellings might also be the expansion of periaxonal space according to a recent report[230] where either physiological electrical stimulation or veratridine was applied to induce a similar phenotype in the PNS. EM examination shows that the expansion of the periaxonal space might have been caused by Na^+ returning to the extracellular space from the axon to maintain the intracellular Na^+ homeostasis. This report is different from my study of AR in which the YFP exclusion was also caused by calcium rise via ryanodine receptors. There is little evidence to indicate that activation of ryanodine receptors would disturb Na^+ homeostasis. Furthermore, my data show that the YFP exclusion was mainly situated at the internodal region of CNS axons (vs. paranodal regions in the published PNS study), and this phenotype would eventually result in axonal spheroid formation and transection. Though the YFP exclusion is morphologically similar to my data, these phenotypes are fundamentally different because the reported YFP exclusion appeared in PNS physiological condition whereas my data suggests that the YFP exclusion appeared in CNS pathological condition.

4.8 Conclusion

Here I showed the dynamic time course of spheroid formation in live CNS myelinated axons using a stable *ex vivo* model of white matter and high resolution two-photon microscopy. Axons

exhibited a stereotyped pathology in the form of focal swelling and spheroid formation in response to a variety of insults. Chemical anoxia predictably induced severe pathology, but in contrast, even high concentrations of glutamate caused only modest injury that was delayed by many hours. This was due to a combination of diffusion barriers such as the overlying meninges, and the ability of well-energized white matter to buffer even large quantities of exogenous excitotoxin. Even mild energy deprivation or interference with glutamate uptake, greatly exacerbated excitotoxin induced pathology, underscoring the energy dependence of active glutamate uptake to protect white matter axons from excitotoxicity. These findings have important implications for diseases such as MS, where relative energy deficits[139,202], increased sources of glutamate from inflammatory infiltration[129,231,232], and impaired glutamate homeostasis[176,233], have all been shown to exist. My data now show that such an environment may cause direct axonal pathology, with morphology identical to that found in human MS brain by conventional histopathology. This further underscores the fundamentally important role that white matter excitotoxic mechanisms play in the degeneration of this tissue in MS and other conditions as well. Finally, recent data have implicated internal axonal calcium stores in mediating axonal injury, a mechanism that may be as important as pathways mediating influx of extracellular calcium into the fiber[34,170]. I also show that direct release of calcium from axonal endoplasmic reticulum stores, also induced focal spheroid formation and axolemma pathology, independent of any excitotoxicity. Given the known interaction of these two signalling mechanisms in other cells[34,170], it is highly likely that both glutamate induced extracellular calcium influx into axons, together with internal calcium release from axonal calcium stores, conspire together to promote even more irreversible axonal degeneration. A more in-depth mechanistic understanding of these important interrelated mechanisms, paves the way for

improved pharmacological intervention to protect vital axonal connections in a variety of CNS white matter disorders.

Chapter Five: Spectral microscopy of myelin pathology using the solvatochromic probe-Nile red

5.1 Abstract

There are few tools available to study the physico-chemical makeup of intact, living myelin, or to track chemical changes as a function of injury. Fluorescent solvatochromism is the interesting property of a number of fluorophores whereby they undergo changes in their absorption and/or emission spectra in response to changes in the polarity of their local chemical environment. I used a solvatochromic dye - Nile red (NR) to probe myelin lipid chemistry. I hypothesize that myelin changes in early injury can be measured with NR. NR would respond with shifts of its fluorescence emission spectrum. NR not only chemically probes the polarity of myelin lipid in mice and human but also spatially details myelin. Furthermore, in order to quantify and compare the changes of lipid polarity among myelin populations, I introduced a novel methodology called Nile red solvatochromic shift assay (NRSSA). Using NRSSA, I identified and quantified the lipid polarity of physiological myelin. I further applied the method to study pathological changes in myelin by measuring lipid polarity alterations in demyelination and remyelination in animal and human samples from multiple sclerosis. In summary, NR is a powerful tool for exploring polarity changes in living tissue in response to injurious stimuli. Rapid staining and high spatial resolution imaging of live myelin makes NR well suited for *in vitro/ex vivo* and *in vivo* study of the fundamental mechanisms of demyelinating disorders.

5.2 Introduction

Myelin is a highly ordered, lipid-rich, multi-layered spiral of cell membrane that supports rapid and energy efficient saltatory conduction of action potentials in the central and peripheral nervous systems (CNS and PNS)[234]. The ratio of myelin lipid to protein dry weight is 70:30[235]. The functional and structural characteristics of myelin are critically dependent on its unique composition of biochemical lipids[18,236,237]. In particular, changes of lipid compositions in myelin are defining characteristics of development[238,239] in adult[128], aging rodents[238,240] and in primates[39,241]. Change of lipid orientation (e.g. phophatidylserine) from inner leaflet to outer leaflet in cell membrane is an indication of apoptosis[242]. Furthermore, lipid composition also changes in inflammatory demyelinating diseases like multiple sclerosis[235,243–250] (MS) and diseases affecting lipid metabolism in glial cells[236]. More recent studies using lipid microarray analysis suggest that lipids play an important antigenic role in modulating the immune cells to attack myelin in MS[251]. These studies led me to hypothesize that studying myelin lipids could provide insight into the mechanism of myelin injury and repair.

There are challenges in obtaining biochemical information in spatially resolved myelin from intact fixed or live myelin in animal models. The traditional methods to study myelin lipid chemistry require destruction of tissues[252,253]. For example, isolation of myelin from tissues for high-performance liquid chromatography (HPLC)[254] or quantitative electrospray ionization/mass spectrometry[255] requires tissue homogenization. Recent development of non-destructive, label-free myelin chemical imaging has been demonstrated by using Coherent anti-Stokes Raman Scattering[256]. The method requires extensive knowledge of nonlinear optics and the hardware is complicated to operate. Alternatively, fluorescent immunostaining can spatially resolved myelin

protein specific distribution, but it is usually done in fixed tissue and provides microstructural but no biochemical information. To overcome the shortcomings of these experiments, I developed a non-destructive, simple and rapid biochemical myelin staining method using solvatochromic polarity indicator - NR to probe the local environment of myelin.

5.2.1 Nile red as a solvatochromic dye

In general, excited fluorescent dyes emit specific spectra that are largely invariant and are not altered by local microenvironment. For example, the family of Alexa dye is one of the most common conjugated to antibody for immunolabeling[257]. However, some dyes do not exhibit fixed spectra. Their varying emission spectra are in accordance with their interaction with local physical chemical environment. This phenomenon is termed solvatochromism. NR is one of the solvatochromic dyes. NR shifts its fluorescent spectrum according to its local environment of solvent polarity and has been applied to study the changes in local environment of hydrophobic protein[258], in cellular[259] and membrane[260] cholesterol, in lipid droplet composition[261–265] and lysosomal phospholipid[266]. Quantitative study of lipid composition in NR-labeled porcine oocytes has also been demonstrated using spectral microscopy[267]. Additionally, due to its lipophilic property, NR has also proven useful for spatially labeling lipid-rich myelin sheath brightly in the CNS[268,269] and PNS[270]. Because of these properties, NR was selected for the study of solvatochromism in myelin.

5.2.2 General mechanism of solvatochromic shift

In solvatochromism, the interaction between solvatochromic dye and solvent molecules results in spectral shift. This spectral shift is determined by solvent polarity. NR's fluorescent emission

spectral shift reflects chemical polarity changes. For example, increase in the solvent polarity causes red shift to longer wavelength; a decrease in the solvent polarity causes blue shift to shorter wavelength. This phenomenon can be explained by Jablonski energy diagram, where the emission is created by the energy difference between the highest occupied molecular orbital and the lowest unoccupied molecular orbital[271] (Figure 5-1). During the energy transition of NR from excitation to emission, NR shows a typical fluorophore behavior in absorption, (e.g. 10^{-15} second of absorption, blue arrow in Figure 5-1) and with an intermediate stage (between 10^{-10} and 10^{-12} second[272], solvent relaxation stage in Figure 5-1) before the emission (e.g. 10^{-09} second). The intermediate stage determines the magnitude of the spectral shifts. After NR is excited to higher vibrational level of S_1, excessive excited energy is quickly lost to surrounding solvent molecules as the fluorophore slowly relaxes to the lowest vibrational energy level. While gaining vibrational energy, solvent molecules interact with NR by realigning their dipole orientation accordingly to NR's dipole moment (e.g. solvent's δ^+ attracts NR's δ^-), termed solvent relaxation. If the dipole of solvent molecule takes longer time to re-orient while interacting with NR, a further red shift can be observed. In contrast, if the solvent molecules do not interact with NR or take minimum relaxation time, the spectral emission shift of NR is minimal. Another solvatochromic property of NR is to increase or decrease quantum yield in less polar or more polar solvents, respectively. Increase in quantum yield results in brighter NR emission; decrease in quantum yield results in weaker NR emission.

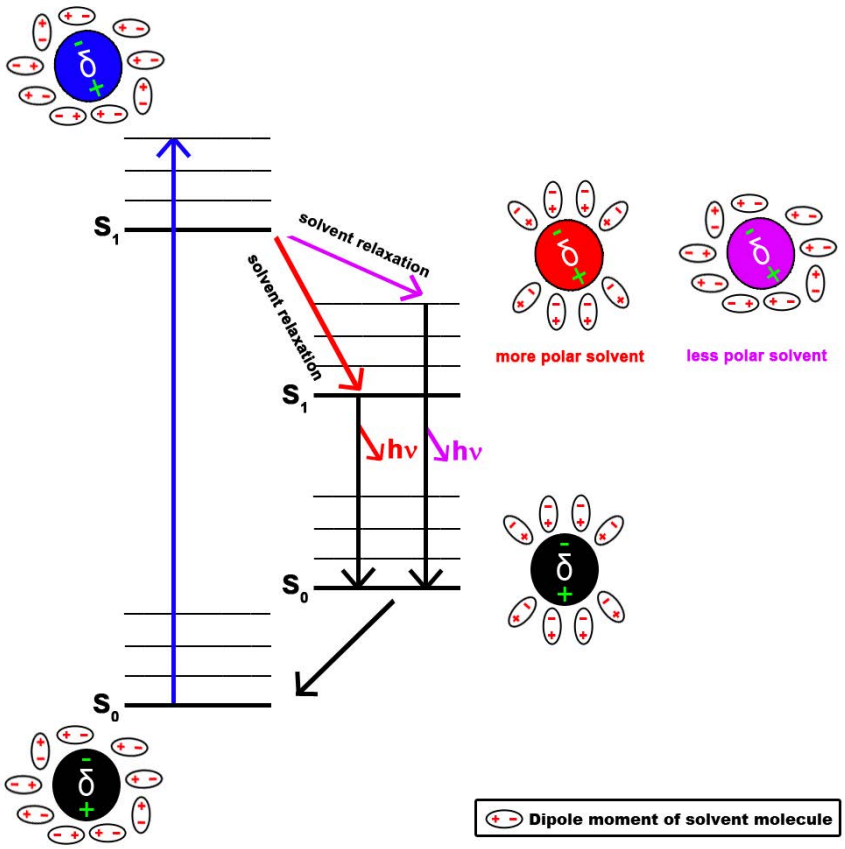

Figure 5-1. Schematic illustration of solvatochromic mechanism by a Jablonski energy diagram

Before excitation, the NR molecule and its surrounding solvent molecules are in the ground state. During excitation, NR's dipole moment increases and re-aligns as shown in blue ovoid. This happens in 10^{-15} second. NR then enters into the solvent relaxation stage (it usually take between 10^{-10} and 10^{-12} second and the range depends on the solvents[272]). The solvent molecules are attracted and their dipole moment realigns accordingly to NR's dipole moment direction. Red and violet ovoids of NR indicated their surrounding solvent molecules as polar and less polar respectively. In a polar solvent environment, NR's dipole moment showed longer relaxation time (red arrow at solvent relaxation state) compared to less polar solvent molecules (violet arrow at solvent relaxation state). The longer time a solvent remains in the relaxation stage, the more the spectrum of NR shifts to longer wavelengths. The shorter time solvent in relaxation stage, the spectrum of NR shifts minimally and returns to ground state.

5.2.3 Quantification of solvatochromic shift by generalized polarization

Traditionally, quantification of solvatochromic shift is done by the generalized polarization (GP) method with two channel fluorescence microscopy[272]. Fluorescence is collected by two detectors, each with specific band pass filters: one for the collection of red shift spectrum and the other for the collection of blue shift spectrum. GP is then measured by defining a wavelength-ratiometric parameter with the following formula,

$$GP = \frac{Ir - Ib}{Ir + Ib} \quad (3)$$

where Ir is the intensity of red shifted value, while Ib is the intensity of blue shifted value. This quantification has been shown in *in vitro* study of isolated phospholipid membranes[273] and intact cell membrane[274]. For my study, I improved this method by collecting the entire emission spectra of NR using confocal spectral microscopy.

5.3 Methods and Materials

5.3.1 Isolation of myelin and sub-fraction of total myelin

Myelin extraction was done according to standard method[275]. Five spinal cords of adult Long-Evans rats (200-250 gm each) were isolated and homogenized in 0.25 M sucrose to make 10% weight/volume solution. Homogenate was centrifuged at 500g for 10 minutes at 4°C. The supernatant was collected and recentrifuged at 11000g for 10 minutes. Supernatant was discarded and the pellet resuspended in 10 ml of 0.25 M sucrose. Then, 25 ml of 0.88 M sucrose was added to the bottom of the tube below the resuspended pellet. The supernatant was centrifuged at 11000g for 10 minutes to separate the mitochondria from the myelin. The myelin floated on the surface while the denser mitochondria pelleted at the bottom of the tube. The

upper myelin layer was removed and stored at 4°C. This was the total myelin. To isolate crude cholesterol and lecithin, I added 4 volumes of acetone into total myelin and blended the mixture for 1 minute at high speed. The crude cholesterol as supernatant was dissolved in acetone solvent while crude lecithin appeared at the bottom. For imaging myelin (total myelin, crude cholesterol and lecithin), I transferred 100 µl of each myelin sample on the glass slide and let it dry. 1 ml of phosphate buffered saline (PBS) containing 30 to 50 µM of NR was added to the sample and the sample was remixed at room temperature for 10 minutes, then semi-dry slides were taken for spectral imaging.

5.3.2 Immunolabeling of proteolipid protein (PLP) in isolated myelin

After obtaining isolated myelin from rat spinal cord, I separated myelin into three groups: myelin with primary and secondary antibody, myelin with secondary antibody and unstained myelin. Primary antibody monoclonal mouse anti-PLP (Millipore Cat#mab388, dilution 1:200) incubated for 30 minutes. Then, secondary antibody Alexa Fluor 405 (Life Technologies Cat#A-31553, dilution 1:200) was added to the primary antibody and incubated for 30 minutes. After that, I added 10 µM NR to these samples.

5.3.3 Spectral imaging solvents in capillary tube

To obtain the fluorescent emission spectrum of the solvents, hexane, toluene, chloroform, acetone, Dimethyl sulfoxide (DMSO), and methanol were mixed with 10 µM of NR in glass vials. Each solvent was loaded into 1 m x 75 mm of glass capillary tubes via capillary action. Then, the tubes were imaged by spectral confocal microscopy.

5.3.4 Animal handling

All the protocols for animal handling followed the Canadian Council on Animal Care (CCAC) guidelines and the animal procedures were approved by the University of Calgary Animal Care Ethics Committee. For the development and aging study of myelin, four groups of C57/B6 transgenic mice expressing yellow fluorescent protein in axon were used; each group consisted of three mice were divided into postnatal day 5 (P5), day 10 (P10), day 30-60 (adult) , and day 430 (old mice). To study PLP in solvatochromic effect, two PLP-null adult mice and three P_0-CNS mutant adult mice were obtained from the lab of Dr. Bruce Trapp at Cleveland Clinic, USA. The procedures for preparation spinal cord explants are described in Chapter 3.

5.3.5 LPC-induced spinal cord demyelination and remyelination

To study demyelination in mice, a double transgenic mouse model expressing yellow fluorescent protein (YFP) in axons and green fluorescent protein (GFP) in microglia was used in collaboration with the lab of Dr. V. Wee Yong. They performed the L-alpha-lysophosphatidyl choline (LPC) injection of the spinal cord. Four females CX_3CR_1-GFP/Thy1-YFP young adult (2-3 months) on a C57Bl/6 background were anesthetized with a mixture of ketamine (47.5 mg/kg) and xylazine (2.5 mg/kg). The spinal cord dorsal column was then exposed at the T3-T4 vertebra. A 1.0 µL solution of 1% D-lysophosphatidylcholine (lysolecithin; Sigma, St. Louis, MO) was slowly injected on top of the cord (subdurally) 1 minute using a $30^{1/2}$ gauge needle attached to a 2 µL Hamilton syringe. The needle was left in place for 2 minutes to prevent backflow of the lysolecithin out of the dorsal column. Mice were sacrificed at day 3 (N = 2) and day 36 (N = 2) post-LPC injection.

5.3.6 Delipidation of whole spinal cord tissue

Whole animals were fixed (N = 3) with 4% paraformaldehyde (PFA) via intracardiac perfusion. 1.2 cm cervical spinal cord was isolated and the tissues were fixed again with 4% PFA overnight in 4°C. The next day, the tissues were washed three times with 0.1 M PBS and submerged in chloroform and methanol (2:1 vol:vol) for 36 hours. They were then washed three times with 0.1 M PBS for 30 minutes and incubated overnight (12-17 hours) with 50 μM of NR at 4°C. For the treatment of Triton X-100, tissues were fixed with 4% PFA overnight. The next day, tissues were washed with 0.1 M PBS and resuspended in 5% (v/v) Triton X-100 in 0.1 M PBS buffer for 12 hours at 4°C. Then, tissues were washed five times with 0.1 M PBS and stained by 50 μM of NR for one hour before being mounted onto imaging chamber for spectral imaging.

5.3.7 Ex vivo spinal cord preparation

P5 and P10 mice were put on ice block as a way of anesthetization for 10 minutes, then a 3-5 mm of spinal cord was dissected out and submerged at 4°C with fixative 4% PFA. The next day, I stained the dorsal column with NR (30 μM) in PBS for 10 minutes. Adult and old mouse spinal cord explant preparation was described in Chapter 3.

5.3.8 Nile red solvatochromic shift assay for myelin chemical screening

One mM stock solution of NR (Life Technologies Cat#N-1142) was prepared in DMSO and stored at -20°C freezer. The range of 1 μM to 100 μM was used for myelin staining. The most appropriate concentration depends on the specimen size (slide vs. whole tissue), light source and transgene expression. In LPC-induced demyelination study, 476 nm laser was selected to simultaneously collect three non-saturated emission spectra (YFP/GFP/NR) in CX_3CR_1-

GFP/Thy1-YFP adult. However, 476 nm laser was not the optimal excitation wavelength for NR. To overcome this, higher concentration of NR was used to increase the signal. To verify the report about concentration dependent spectral shift[265], I tested a concentration of NR from 1μM to 100 μM in methanol and found no effect on spectral shift. To stain myelin (isolated myelin, fixed spinal cord myelin *in situ* and white matter from histology sections), a minimum of 10 minutes incubation was required. For staining live myelin in explant, a minimum of 30 minutes incubation was required. If live imaging takes more than 4 hours in perfusion system, it is recommended to add 10 μM NR directly into the artificial cerebrospinal fluid solution in the perfusion system in order to maintain signal.

5.3.9 Human samples

I collaborated with Dr. Jeroen Geurts from VU University, Amsterdam and obtained a brain section from a 73-year-old male patient with secondary progressive MS. Cause of death was urosepsis and renal insufficiency. The post mortem delay was 5:15 hours. Control brain tissue was obtained from a 74-year-old male and the cause of death was lung carcinoma. At autopsy, the brains of patients were cut into approximately twelve coronal slices of 10 mm thick. Subsequently, five slices were selected for MRI screening. The frontal slice was put directly into 10% formalin after MRI scanning and was used for this study. Based on MRI images of the frontal slice, the regions contained MRI and macroscopic visible rim of a white matter lesion, center of a white matter lesion, diffuse appearing white matter and normal appearing white matter were isolated and mounted on slide. Slides were then stained by 50 μM of NR in 1X PBS solution for 10 minutes and washed for 5 minutes two times with 1X PBS before spectral imaging.

5.3.10 Spectral confocal laser-scanning microscopy and data processing

All the experiments were done using 488 nm laser to excite NR unless otherwise noted. Fluorescence spectral images were recorded using up-right Nikon A1RMP (Nikon, Inc.) at room temperature or 35°C with an objective lens (NA 1.1). The spectral resolution was 10 nm with 32 channels ranging between 490 nm and 740 nm. To standardize data analysis, all the spectral data were converted into 400 data points with cubic spline interpolation, and each spectrum was then normalized for general comparison and used for spectral decomposition. The analysis was performed on imaging processing software, ImageTrak.

Two bracketing basis spectra were used to define the minimum and maximum range of polarity value in ImageTrak. To generate quantitative pseudocolor images, linear decomposition was done using the two selected bracketing spectra. Two channels were generated after linear decomposition: green index channel represents the total intensity of unmixed channels; red index channel represents the polarity value. To select ROI on the quantitative pseudocolor image for NRSSA analysis, I added a mask channel on the image. The mask area were selected by an adaptive threshold value above 90% of intensity[276] using green channel. Histogram was then generated based on red index channel. To make spectral profile comparable, spectral data were collected as follows:

1. The average intensity from any ROI must be 50-fold greater than background.
2. Irrelevant contaminating signals such as fluorescent protein, autofluorescence, and laser backscatter were removed by linear spectral decomposition.

5.3.11 Statistical analysis

Statistical significance was determined with IGOR Pro (WaveMetrics Inc., Oregon, CA, USA) using chi-square test., $p < 0.05$ is considered statistical significance. N is the number of animals used to repeat the experiment. NRSSA statistic of all the samples is available at Appendix C.

5.4 Results

5.4.1 Nile red solvatochromic shift assay (NRSSA)

The wide range of NR emission spectra shown in Figure 5-2a is due to varying polarity of the solvents used to dissolve the dye. I then devised a method to yield a single numerical index representing the degree of spectral shift, and therefore, the polarity of the medium NR is reporting from Figure 5-2b. Each pixel in the image contains an associated 32-point spectrum, which can then be numerically compared to the standard spectra obtained from known solutions as in Figure 5-2b. A polarity index was then calculated in accordance to how close each pixel spectrum was to each of the two extreme bracketing spectra, such that if a pixel spectrum closely matched the spectrum from hexane, it would be assigned an index of 0, and conversely, if it matched that from the more polar solvent methanol, it would be assigned an index of 1.0. Each pixel in the image was processed in this manner, and resulting indexes from all pixels plotted as a histogram and shown in Figure 5-3a. As expected the distributions are narrow because the emissions are expected to be very uniform from a homogeneous medium such as a NR solution. Moreover, the position of each peak of the histogram reveals how polar the solution is, and therefore, reflects its biochemistry. Because the algorithm used to calculate the polarity index of each spectrum between the two standard bracketing spectra is linear, as expected, there is a strong linear relationship when the six solvents were analyzed using this method (Figure 5-3b).

The same principle was then applied to the more complex and biochemically heterogeneous samples of myelin. Empirically, the two bracketing spectra shown in Figure 5-4 best captured the range of spectral pixels obtained from two selected populations from an isolated myelin samples (Figure 5-5). The greater sensitivity for subtle spectral changes of the NRSSA technique over mean spectrum is illustrated in Figure 5-6a. A spectral and pseudocolor image of isolated myelin stained with NR was analyzed with NRSSA method (Figure 5-6b and c). The index histogram clearly shows two lipid populations with different polarities compared to the single averaged emission spectrum (red plot in Figure 5-6a) which does not reveal the two distinct populations.

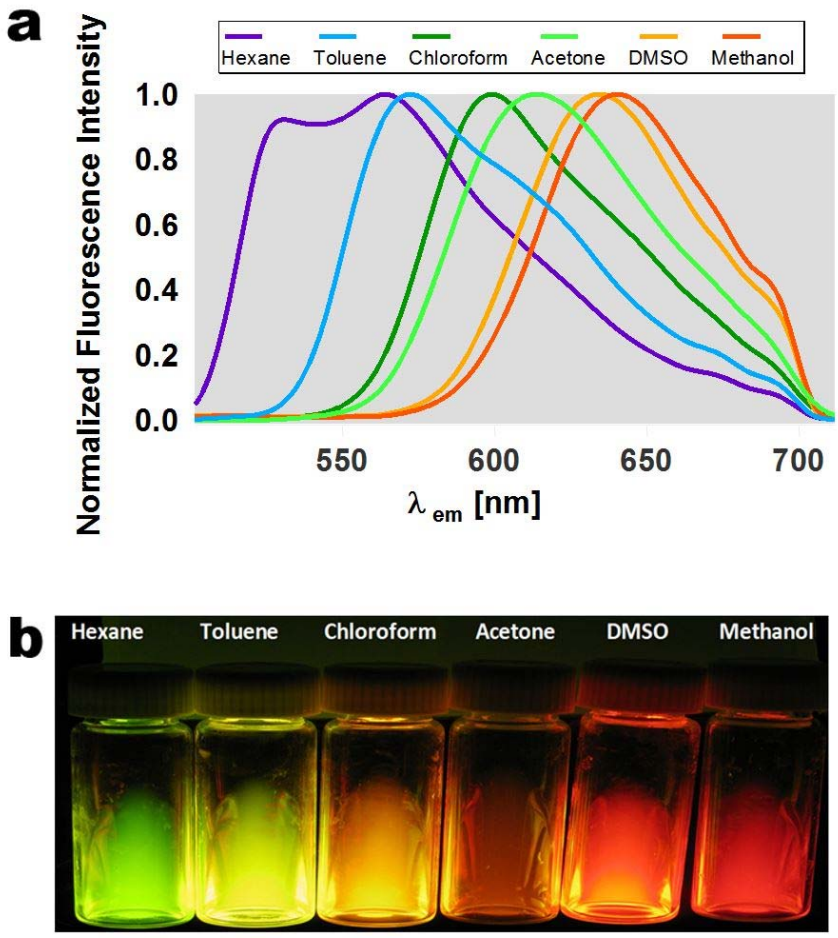

Figure 5-2. The principle of NR solvatochromism

a, the fluorescence spectra of NR in various solvents show a wide range (76 nm) of spectral shift. b, the polarity of each solvent was demonstrated by the emission of their fluorescent colors ("true-color") using excitation with near-UV light at 370 nm. Green fluorescent color presented by hexane is least polar whereas red fluorescent color presented by methanol is most polar among the solvents.

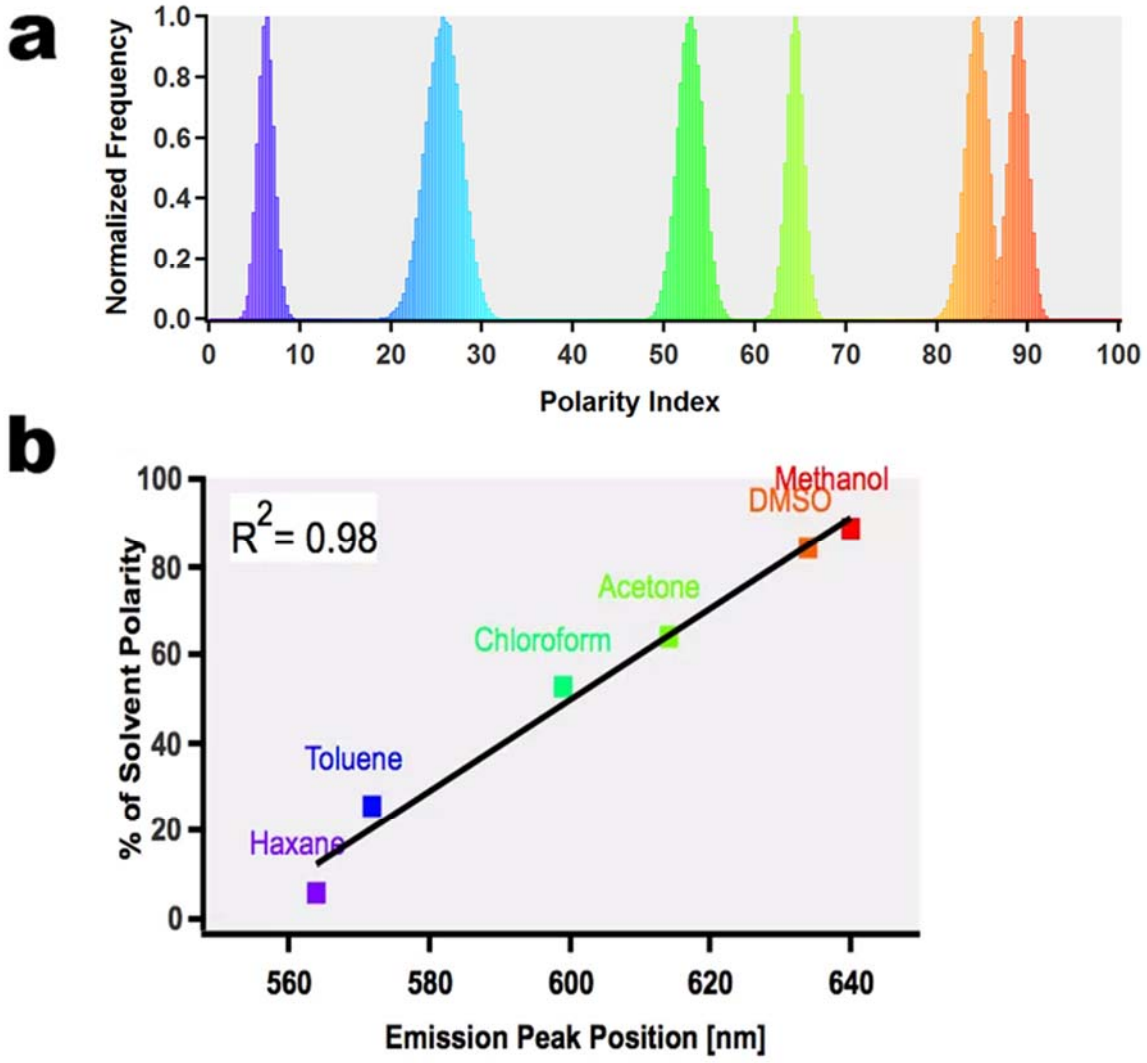

Figure 5-3. The method of NRSSA

a, presentation of each solvent as a population in histogram by the scale of their relative polarity index (1-100) vs. normalized frequency in NRSSA analysis. b, demonstration of the linear correlation between lambda and polarity index by plotting maximum peak of lambda and polarity index of each solvent.

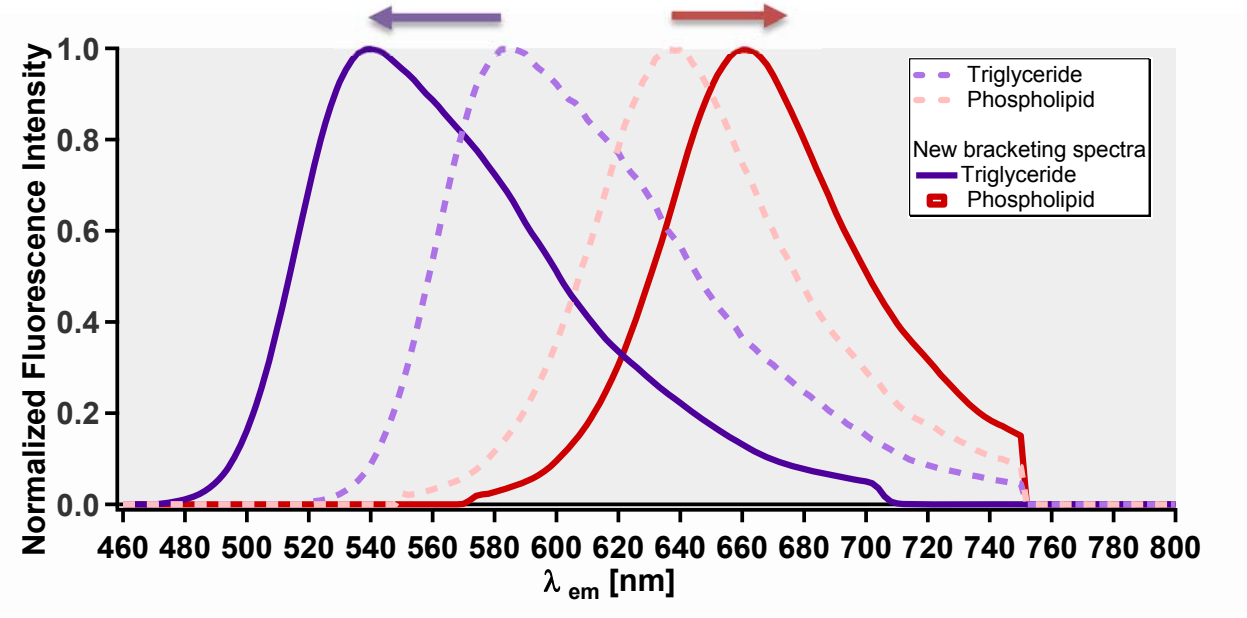

Figure 5-4. The design of the bracketing spectra for NRSSA

The bracketing spectra are used to define the scale of polarity index (0-100) in NRSSA method. Triglyceride and phospholipid are selected as the bracketing spectra for all the NRSSA analysis. The range between these two spectra is extended to allow all the solvents resolve on the scale of polarity index. The new bracketing spectra (solid lines) cover the range between 540 nm and 660 nm.

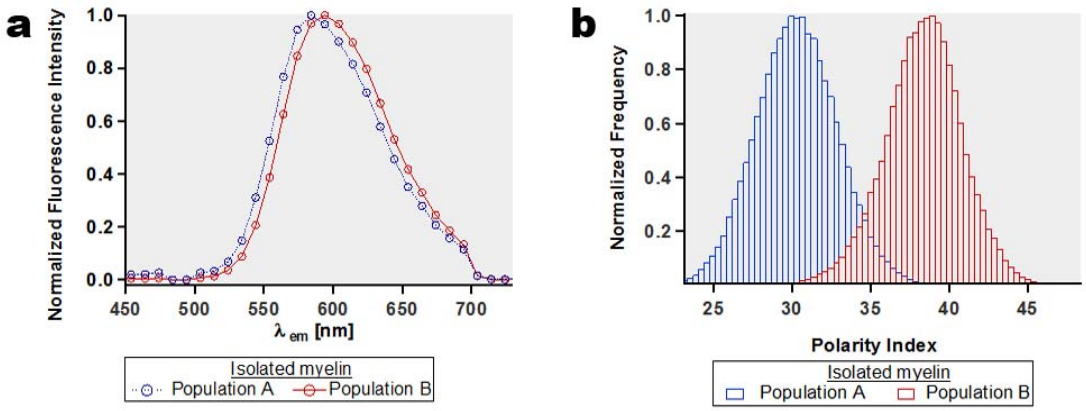

Figure 5-5. Validation of NRSSA in isolated myelin

a, a pair of lambda datasets shows 12 nm shift from two populations of isolated myelin. b, presentation of solvatochromic shift assay from (a), a roughly 9-point differences is obtained and unlike lambda, these two populations shows minimal overlapping area.

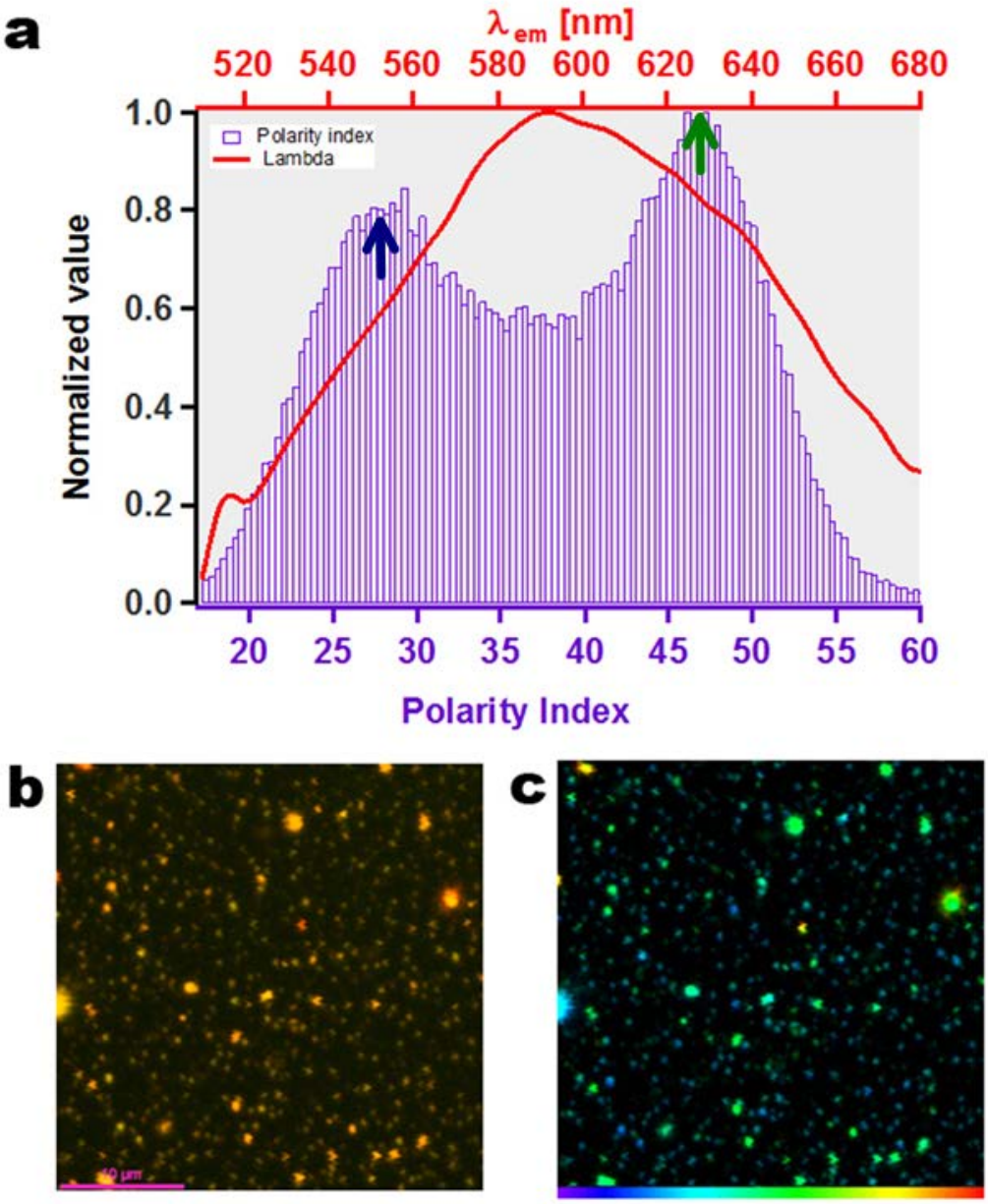

Figure 5-6. Sensitivity test of NRSSA analysis

a, the emission spectrum of sub-isolated myelin containing major crude cholesterol shown in lambda (red solid line). It contrasted with the result of NRSSA (purple histogram). NRSSA analysis shows two distinct population. The less polar population is at the peak index 27 (blue arrow) and the more polar one is at the peak index 47 (green arrow). b, spectral image of myelin globules from the sub-isolated myelin population containing major crude cholesterol. c, pseudocolor image (b).

5.4.2 Evidence of solvatochromic effects in isolated myelin fraction

I then used isolated myelin fractions to study the heterogeneity and distribution of spectral shifts (and therefore biochemistry) in this purified sample. Total myelin fraction from four adult rat spinal cords were isolated, dried on microscope slides and stained with NR. Myelin prepared in this manner clustered into globules on the slide, and stained brightly with NR. To exclude contamination from other CNS elements during isolation, the myelin origin of the samples was confirmed by PLP immunostaining (Figure 5-7a-d). Spectral analysis of the isolated total myelin fraction revealed considerable spectral variability between globules as illustrated by the pseudocolor image in Figure 5-7e. This variability might be due to their polarity with "like dissolves like" that leads to aggregation of globules. Spectra varied between 576 nm (less polar) and 640 nm (more polar) (Figure 5-7f, peak λ), with the blue-shifted components of the fraction exhibiting brighter fluorescence intensity (Figure 5-7g). The overall distribution of spectral positions/indexes from an entire image is shown in Figure 5-7h. The peak was centered at an index of ≈37. Note the distribution was considerably wider than from pure solvents reflecting the heterogeneity of polarities of the constituent myelin lipids. Chemical extraction of crude cholesterol and lecithin showed the expected spectral shifts to the left for cholesterol (less polar) and to the right for lecithin (more polar) (Figure 5-7h). Note that the histograms in this figure are normalized; in reality the absolute magnitudes of these two extracted components are much smaller than total myelin signal, and contribute to the wide "tails" of total myelin extending over a broad range of polarities.

Taken together, myelin can be seen as a complex "solvent" that induces solvatochromic effects in certain lipophilic dyes by virtue of its heterogeneous lipid composition. The NRSSA method

allows very sensitive and spatially-resolved analysis of biochemical lipid changes in myelin, and was then applied to the study of intact myelin under various physiological and pathological conditions.

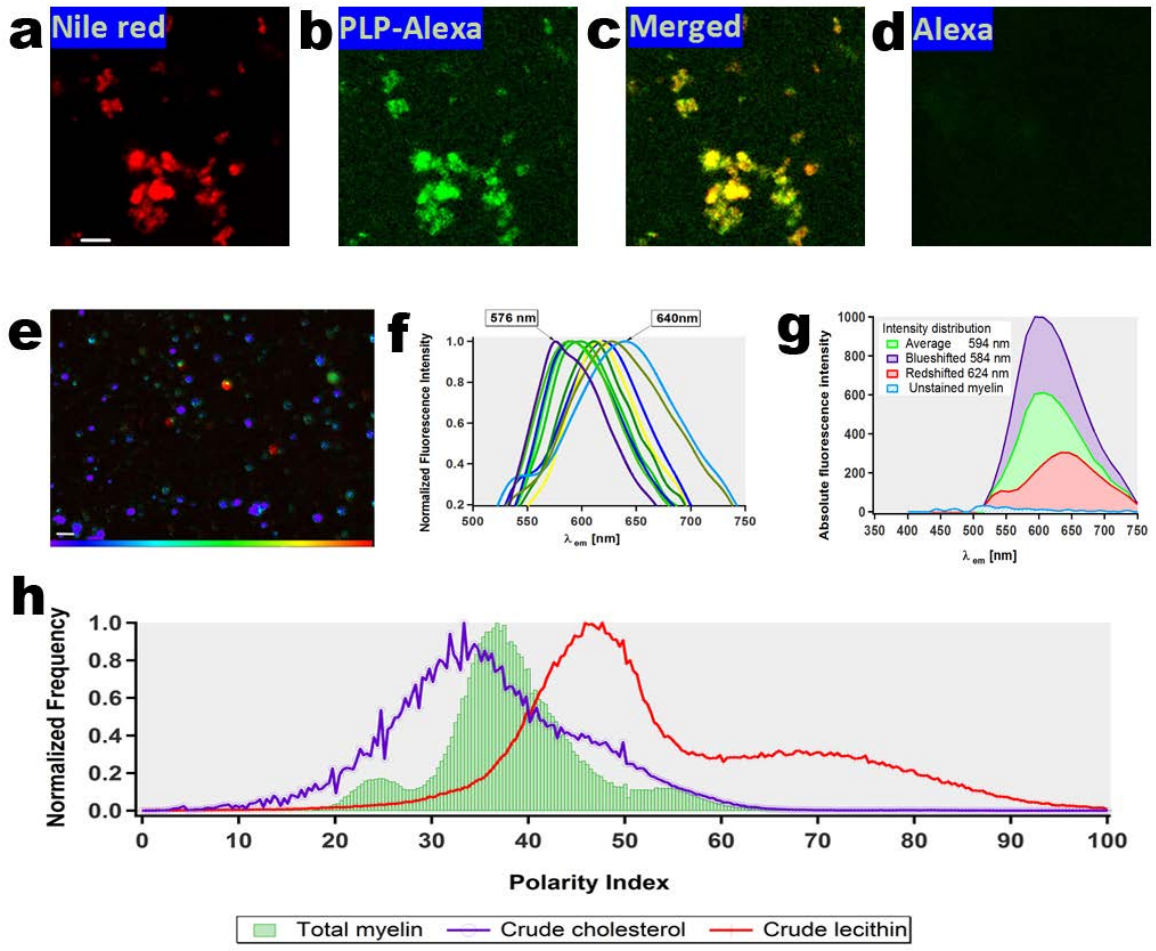

Figure 5-7. Characterization of isolated myelin fractions

a-d, immunostaining of PLP in isolated myelin showed co-localization with NR. Total isolated myelin stained with NR alone (a), PLP immunolabeling alone (b), NR and PLP immunolabeling (c), second antibody Alexa immunolabeling alone as negative control (d). e, pseudocolor image of total myelin. An average of 5 µm diameter myelin particles was collected via sucrose two-step gradient purification from rat spinal cord, and stained with NR on the slide for spectral confocal imaging. f, the graph shows the range of spectra among the population of myelin particles. g, intensity measurement of fluorescence spectra from myelin populations: red shifted, average, and blue shifted. The blue-shifted population of the fraction exhibited higher fluorescence intensity whereas the red-shifted population showed lower fluorescence intensity. h, NRSSA showed total myelin (green histogram) at index ≈37

with extended two “tails”. Crude cholesterol population is less polar than total myelin. In contrast, crude lecithin is more polar than total myelin. Scale bars = 5 μm

5.4.3 Solvatochromism of myelin in situ

I next asked whether myelin *in situ* from adult spinal cord explant can exhibit solvatochromic properties similar to myelin *in vitro* (isolation of myelin). Spinal cord explant was fixed and myelin sheaths were stained by NR (Figure 5-8a). *In situ* myelin was then compared to the isolated myelin using NRSSA analysis. Spectra from fixed myelin *in situ* were more homogeneous than isolated myelin with peaks ranging from 588-594 nm (Figure 5-8b). This was reflected in the distribution of polarity indexes which was narrower than from isolated myelin (Figure 5-8c), exhibiting a peak distribution at index = 34. Interestingly, this peak was shifted to a less polar index compared to isolated myelin (peak index = 37). This may be due to paraformaldehyde fixation which is known to crosslink proteins and some lipids, and to lower solubility of membrane phospholipids[277,278]. Next, I explored the role of myelin lipids in determining the polarity as measured by NR. Chloroform and methanol (2:1 vol:vol) were used to extract nonpolar and polar lipids (respectively) by the Folch method[279] from fixed mouse spinal cord. After 36 hours of exposure to these solvents, samples were stained with NR and spectral images acquired as before. Myelin morphology was not altered by lipid extraction (Figure 5-8d), which is not surprising given that the samples were already fixed in PFA. Removing myelin lipids by this method had a dramatic effect on overall polarity, which shifted from a peak index of 34 before extraction to 47 after lipid removal (Figure 5-8e). This is in line with expectations because solvents will remove the more labile less polar lipid components, leaving a more protein-rich water-soluble cytoplasmic matrix, which is more polar, and which also binds NR[280,281]. Treating spinal cord with the detergent Triton X-100 seemed to be even more effective at removing myelin lipids as the peak index was shifted to even higher values (≈51) than with chloroform and methanol (Figure 5-8e).

The shift of index to a less polar value in fixed intact myelin compared to isolated fractionated myelin was unexpected. I then explored the question whether fixation artifactually shifted the index, or whether myelin isolation was artifactually shifting the peak index to more polar values. Live mouse spinal cord was maintained and oxygenated in perfusion chamber at 35°C. The live myelin tissue was stained brightly with NR in perfusate containing 20 μM of NR. The NRSSA analysis of live myelin showed a peak index at 38 very close to that of isolated myelin fraction (37), and significantly different from PFA-fixed samples (Figure 5-9). This analysis therefore demonstrates that at a biochemical level, PFA fixation significantly alters the polarity of myelin lipids as reported by NR spectroscopy. As the live preparation was kept in the perfusion chamber, the peak index changed to progressively higher values indicating loss of nonpolar species (Figure 5-10a, chi-square test, $T = 0$ vs. $T = 8$: $p < 0.001$, $N = 3$). This change in spectroscopic index occurred despite little if any change in morphological myelin characteristics (Figure 5-10b). Together my data show that while *ex vivo* live preparations of my white matter tracts can be kept alive and morphologically intact for many hours, there are early biochemical changes that my method can reliably report. Therefore, my NRSSA analysis appears to be very sensitive for detecting biochemical changes in myelin, and was then used to study myelin changes under various conditions of development and pathology.

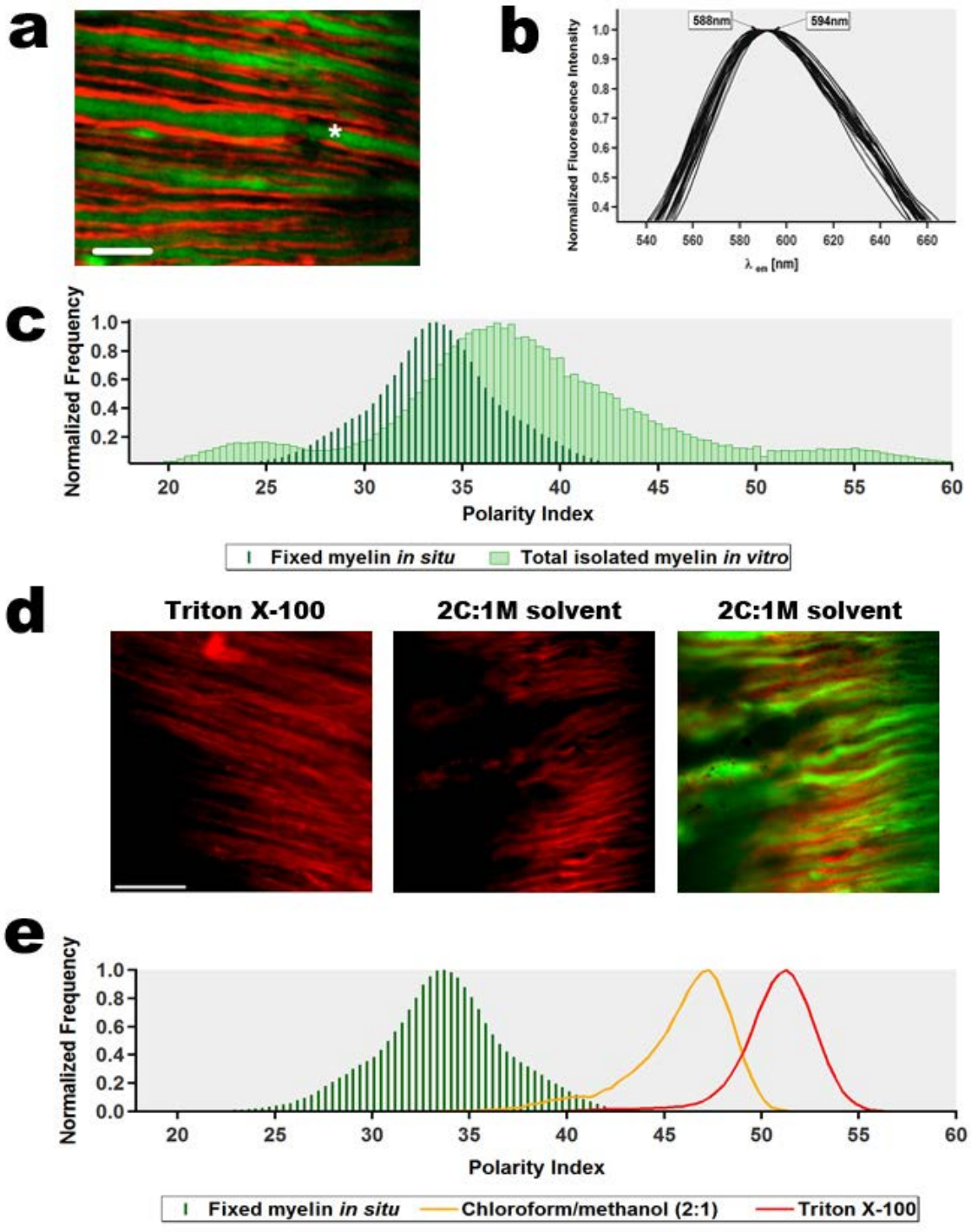

Figure 5-8. NRSSA analysis of fixed myelin *in situ*

a, dorsal column myelin was fixed by 4% PFA overnight. Multiple myelinated axons and a node of Ranvier (white asterisk) from adult mice dorsal column were shown with high spatial resolution. b, range of spectra shift (588-594

nm) among myelin *in situ* population was presented by maximum emission peak position (N = 10). c, comparison between myelin *in situ* and total isolated myelin *in vitro* fraction. The population of myelin *in situ* with peak index shifted to less polar and presented much narrow band. d, images of fixed myelin *in situ* after treatment with the solvents showed that intact myelin sheaths were still visible. e, 5% Triton X-100 and chloroform and methanol (2:1 vol:vol) were used to delipidate myelin in dorsal column. NRSSA analysis shows that both peak index shifted to more polar.

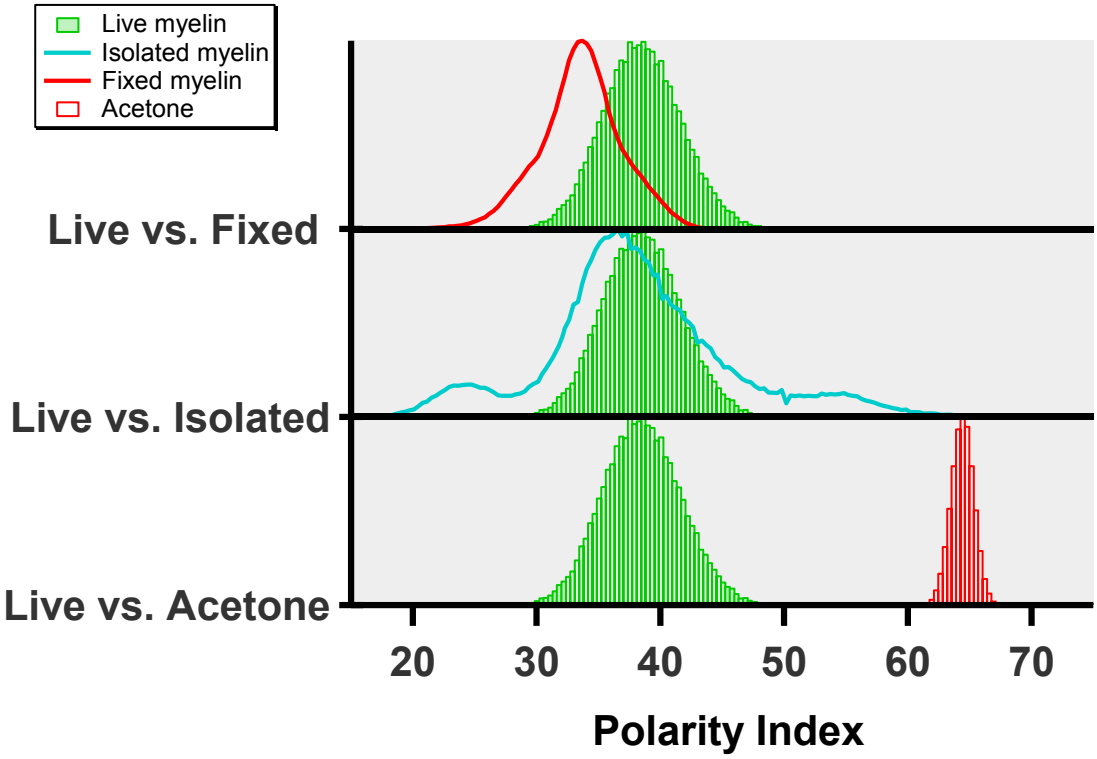

Figure 5-9. NRSSA analysis of live myelin *in situ*

Live myelin spinal cord explant was maintained and oxygenated in perfusion chamber at 35°C, then *ex vivo* spectral imaging of live myelin was performed. NRSSA analysis showed that live myelin is more polar compared to fixed myelin *in situ* (chi-square test, fixed myelin vs. live myelin: $p < 0.001$, fixed myelin, N = 10; live myelin, N = 3) and isolated myelin (chi-square test, isolated myelin vs. live myelin: $p < 0.001$, isolated myelin, N = 5; live myelin, N = 3) respectively. Pure acetone was also compared with the live complex myelin, and NRSSA showed that the sum and the range of acetone population is significantly smaller than myelin (sum: 6.58 vs. 22.2; range: 8.0 vs. 25.2), suggesting myelin is a complex solvent.

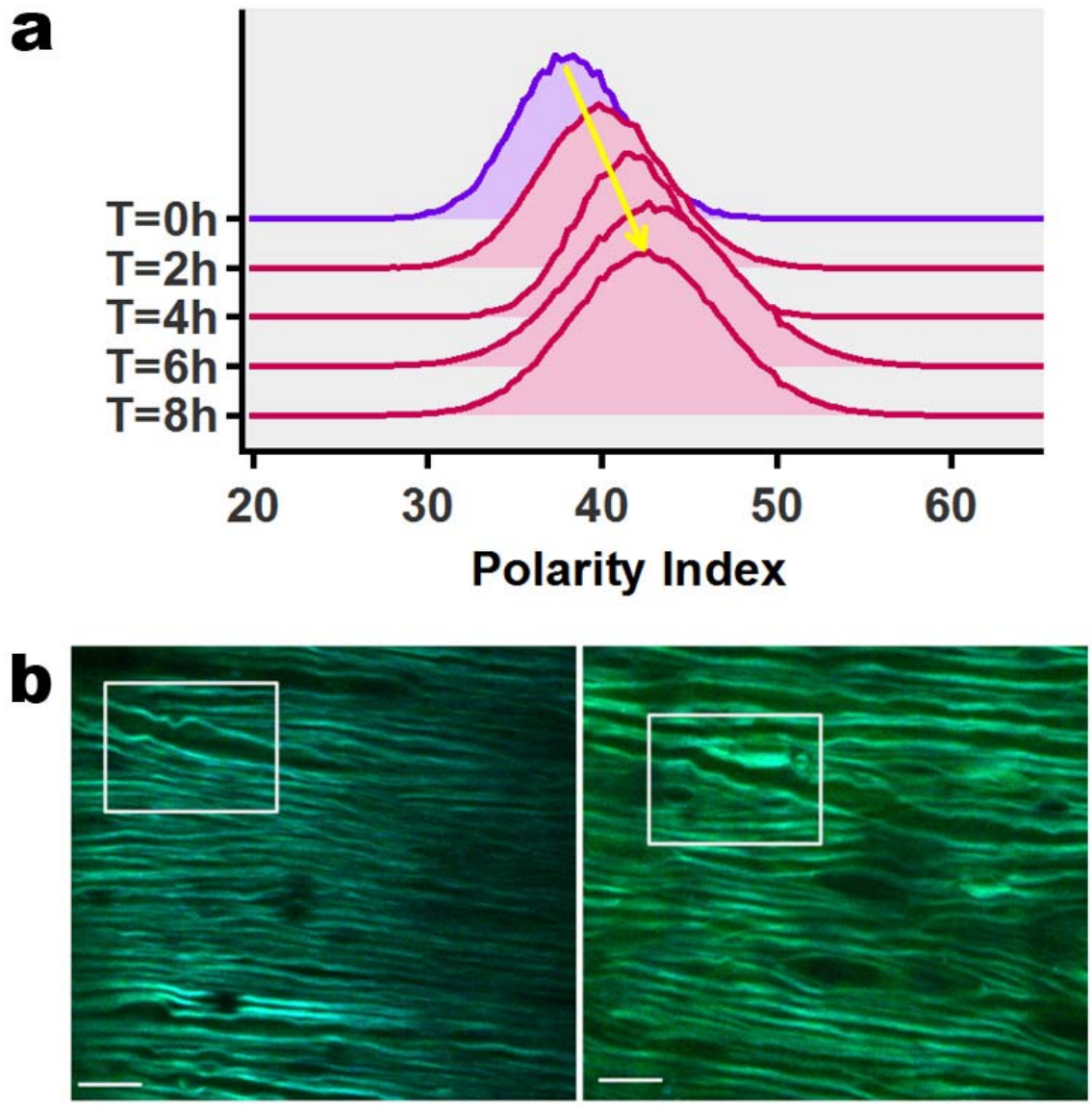

Figure 5-10. NRSSA analysis of *ex vivo* time-course imaging of live myelin sheaths

a, kymograph-like presentation of NRSSA over time. Yellow arrow indicates the population shifted from peak index 38 to 43. From each time point, the population that was above average baseline (purple) was labeled in red (N = 3). b, *ex vivo* myelin images before (left panel) and after (right panel) 8 hours of aCSF perfusion presented in pseudocolor using NRSSA. Scale bar = 10 µm

5.4.4 Biochemical myelin changes in PLP-null and P_0-CNS adult mutant mice

I asked whether mice whose myelin is missing the major myelin protein PLP would exhibit biochemical changes. These transgenics have normal myelination, normal oligodendrocyte development and no behavioural abnormalities, but only late axonopathy[282,283]. Only PFA fixed tissue was available to us for these studies, therefore comparisons were made with the fixed wild type (WT) samples (Figure 5-11a) and two transgenic mice (Figure 5-11b to d). Interestingly, despite swollen myelin (Figure 5-11c-d), my analysis revealed a subtle but statistically significant shift (chi-square, PLP-null vs. WT: $p < 0.05$, fixed myelin, N = 10; PLP-null, N = 2) in polarity index towards more polar values in the transgenics (Figure 5-11e). This might be explained by the role of cholesterol which is reduced by 40% in PLP-null mice[284]. Since the cholesterol imparts a nonpolar component to the distribution (Figure 5-7h), a reduction of this lipid would explain the shift to more polar values overall in the transgenic. Another myelin transgenic is the P_0CNS mutant, where PLP in CNS myelin is replaced by the peripheral myelin protein P_0[285]. In contrast to the PLP null transgenics, the P_0CNS mutant develop a paranodal pathology with swellings of the axon in myelin[285]. Staining with NR and imaging confirmed this focal pathology as evidenced by frequent focal dilatations of numerous fibers (Figure 5-11c and d). Spectroscopic analysis also showed that both pathological areas of swelling, and normal appearing non-swollen stretches of myelin, both exhibited polarity index shifts to more polar values, compared to fixed WT of controls (Figure 5-11e, chi-square test, P_0CNS vs. WT: $p < 0.001$, WT, N = 10; P_0CNS, N = 3). Taken together, these results show that the NRSSA analysis is very sensitive at detecting subtle biochemical changes in myelin independent of microscopic morphological abnormalities.

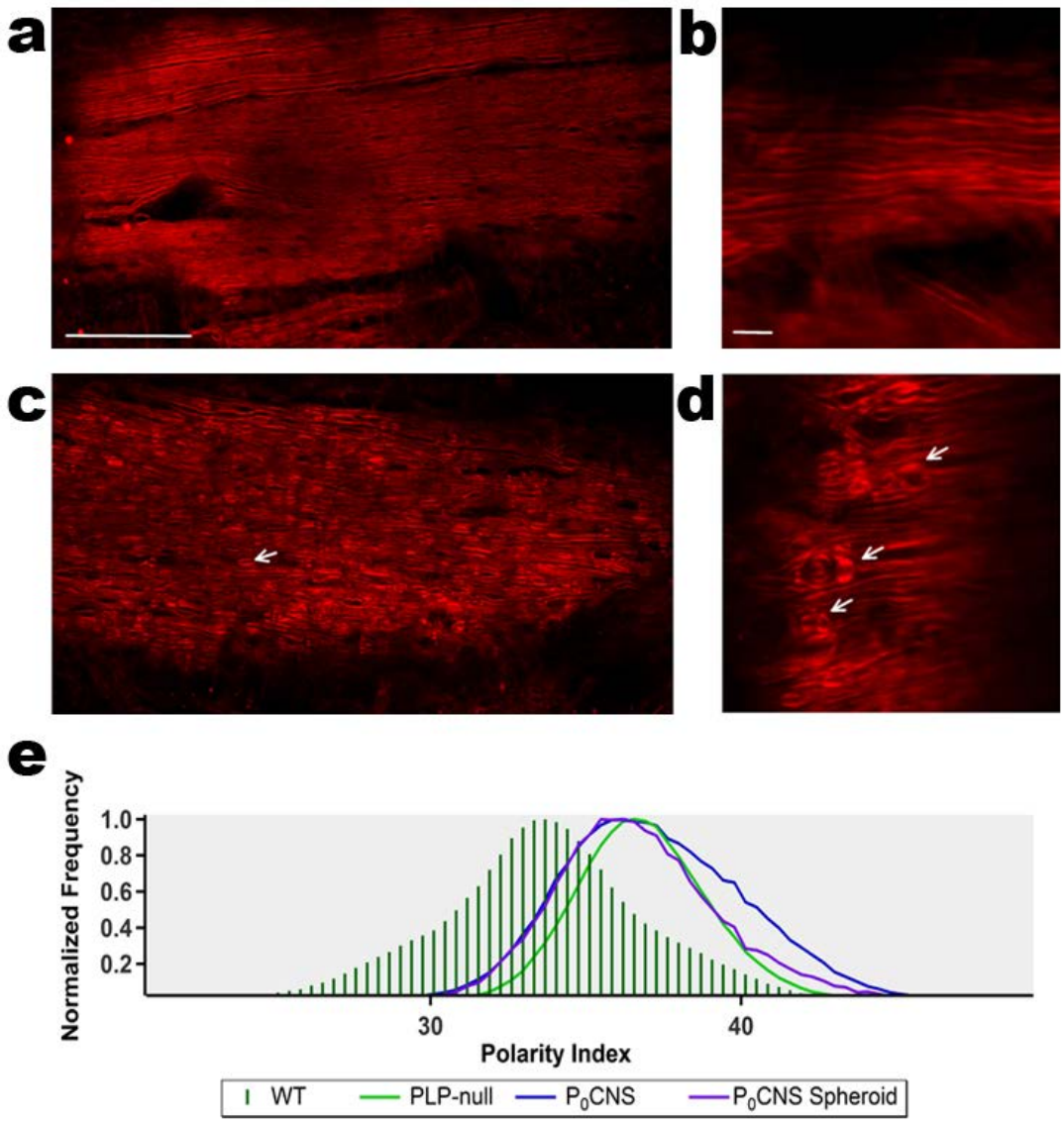

Figure 5-11. *In situ* imaging of myelin in dorsal column of adult transgenic mice PLP-null and P_0CNS

Transgenic mice of WT (a), PLP-null (b), P_0-CNS (c and d) were imaged and compared morphologically. PLP-null mice was morphologically same as WT. P_0-CNS showed myelin swellings (white arrows), presumably these were axonal spheroids[285]. e, polarity value in both PLP-null and P_0-CNS mice were slightly increased. In P_0-CNS mice, a sub-population of spheroid was less polar than non-swollen myelin. a and c, scale bar = 100 μm; b and d, scale bar = 10

5.4.5 Solvatochromic property in developing and aging myelin

Myelination follows a programmed sequence of developmental steps whereby the sheath undergoes significant morphological[286] and biochemical alteration[128,287,288]. In particular, cholesterol accompanies myelin growth[281], maturation[280] and aging[240,291]. I therefore examined whether the spectroscopic method was able to follow biochemical changes in myelin as a function of development. I compared four different groups of rodents at different ages – postnatal day 5 (P5), day 10 (P10), adult (P45), and old (P430) (Figure 5-12a). Isolated dorsal column from these groups was stained by NR after 12-17 hours of fixation with 4% PFA. Despite only minor morphological changes, and only at advanced age, there was a dramatic shift in the biochemistry of myelin as a function of age as reported by this spectroscopic method (Figure 5-12b). There was a monotonic and progressive decrease in polarity index from more polar (peak index 45 in very young P5 animals) to less polar (peak index 26) in the very aged animals. These results match what is previously known about lipid composition in myelin as a function of age. Using thin-layer chromatography (TLC), the production of cholesterol in P5 rat myelin is negligible[238], however at day 10, the level of cholesterol increases as much as fivefold[238] and continues to steadily increase throughout adulthood. In aging mice, the increase in cholesterol results from a slow turnover rate of cholesterol[292].

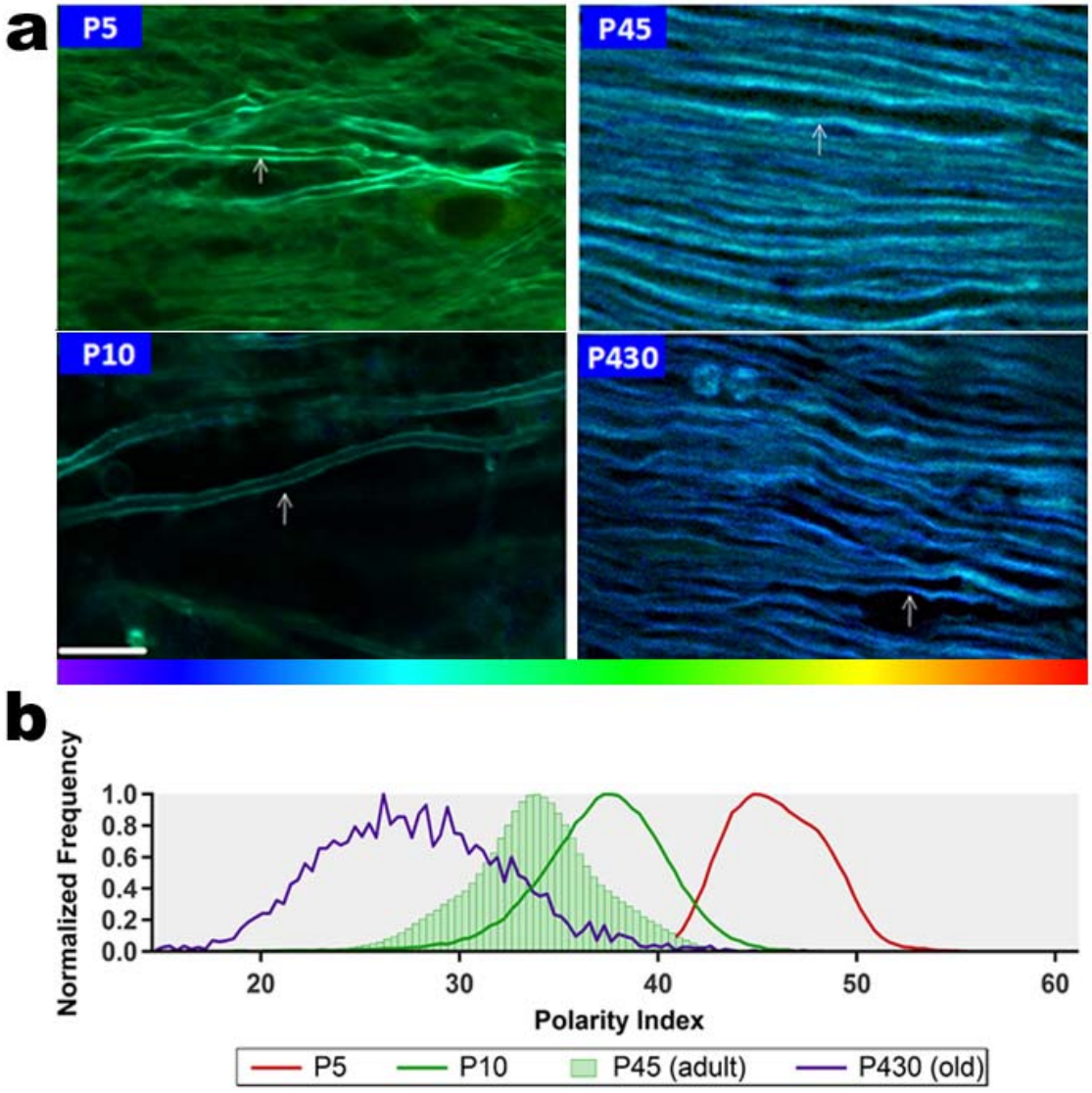

Figure 5-12. Myelin changes as a function of time

a, *in situ* imaging of myelin in dorsal column of P5, P10, P45, and P430 mice. Images were presented in pseudocolor of NRSSA. Over time, the diameter of myelinated axons in dorsal column became thicken (arrows) and stopped at adulthood while its chemical property continued to become less polar. b, NRSSA analysis revealed that as the mice became older (from P5 to P430), their myelin became less polar ($p < 0.001$). Scale bar = 10 μm

5.4.6 Myelin lipid photodamage

To further demonstrate the ability to detect chemical changes in myelin lipids, I performed photodamage on live myelin in dorsal column (Figure 5-13a) using 300 mW two-photon laser power at 800 nm. Radiation of tissue with high power of a femtosecond laser can induce photo damage in a very restricted volume. This is not so much due to local heating, as it is to generation of highly reactive free radicals[269]. This is exacerbated by the presence of a light absorbing material such as a fluorescence dye, which will efficiently absorb laser radiation, and generate free radicals when in the excited state[293,294]. These reactive oxygen species (ROS) will chemically interact with lipids leading to their oxidation[295]. After laser irradiation, myelin in the damaged area chemically shifted to lower polarity (Figure 5-13b, peak index ≈37; chi-square test, live myelin vs. photodamaged myelin: $p < 0.005$, $N = 3$) likely by the mechanism of lipid peroxidation[296]. During lipid peroxidation in myelin, phospholipids of the lipid bilayers are targeted by ROS[297] because polyunsaturated fatty acids in phospholipids are highly susceptible to oxidative attacks[298]. Hence, polar phospholipids are preferentially damaged and therefore overall lipids in myelin shifted to lower polarity.

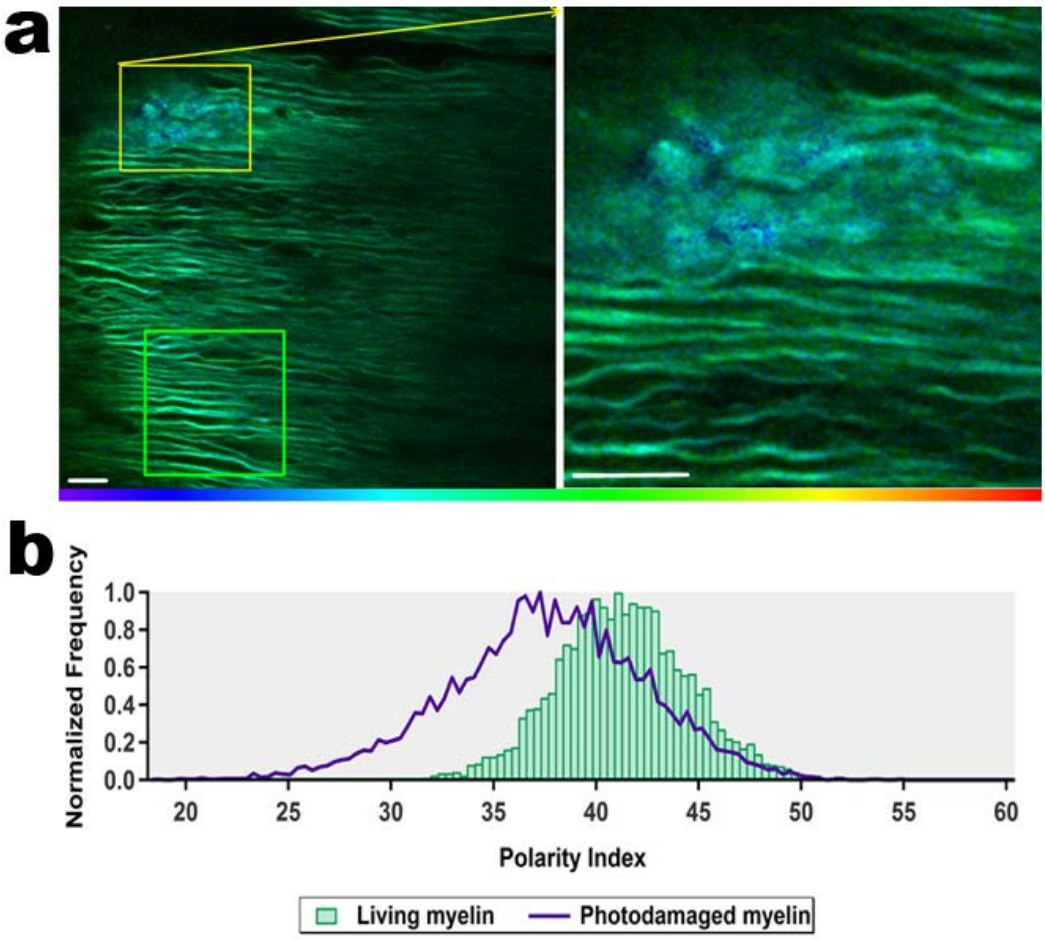

Figure 5-13. Solvatochromic effect on myelin injury induced by photodamage

a, pseudocolor images of NRSSA. The abnormal myelin (yellow box, left figure) was induced by photodamage using 300 mW two-photon laser power at 800 nm and compared to the normal myelin (green box, left figure). Close-up view of myelin injury (right figure). b, photodamaged myelin was less polar than control. Scale bars = 10 μm

5.4.7 Solvatochromic properties in an animal model of demyelination and remyelination

The above experiments were conducted to establish the reliability and sensitivity of the spectroscopic method to detect subtle biochemical changes in myelin. I then applied this technique to study demyelination and re-myelination in an established model using LPC injection to the dorsal column to induce demyelination[299] and remyelination[300] in mice. Four-week-old mice were injected with 5 µl of LPC into the dorsal column using a fine $30^{1/2}$ gauge needle. Sham controls were injected with 5 µl of saline. Animals were left to recover, then sacrificed at 5 and 28 days post LPC injection. Transverse cryosections of fixed dorsal column were stained with 10 µM NR and spectral images acquired, followed by NRSSA analysis as above. Spinal grey and white matter showed distinct polarities as shown by the pseudocolor images in Figure 5-14a (left figure), with the former more polar than the latter (Figure 5-15). This is in keeping with the relatively greater protein content of grey matter compared to lipid content which predominates in myelin-rich white matter. Importantly, the profile of uninjured white matter in this preparation was similar to normal longitudinal myelin sheaths previously, with a peak index of 33 vs. 34 (chi-square test, longitudinal myelin vs. transverse myelin: $p = 1$, longitudinal myelin, $N = 10$; transverse myelin, $N = 3$) (Figure 5-16). Samples were then divided into two regions: the area inside and outside the demyelinated lesions ("normal appearing" white matter) at day 5 and day 28. In the lesion area at day 5, I observed bright lipid droplets within cells in the lesion (Figure 5-14b, middle figure), these cells were foamy macrophages/microglia derived from activated monocytes[301]. To my surprise, the population in the lesion area at day 5 exhibited bimodal distribution with one area shared similar polarity with sham and the other was less polar than sham (Figure 5-17a, chi-square test, $p < 0.001$, $N = 3$). Accordingly, I traced the bimodal distribution from the spectral image. The subpopulation that was less polar than sham

was contributed by the old digested lipid droplets from myelin (Figure 5-14b, middle figure). As for the population that shared similar polarity with sham, it suggests that myelin was not affected by LPC agent. At day 28, remyelination appeared at this timepoint. In contrast to day 5, cells in the lesion now showed very few lipid droplets (Figure 5-14b, right figure). The distribution of the main population was now very similar to sham. However there remained a noticeable and persistent population at a very nonpolar index between 15 and 20, which was never evident in sham or earlier time points of demyelination (Figure 5-17a). The populations in white matter surrounding lesions were slightly different compared to sham at day 5 and day 28 (Figure 5-17b, chi-square test, $p = 1$, $N = 3$). In summary, my spectroscopic analysis had the sensitivity to show very subtle changes in biochemistry in the LPC demyelination model. The white matter surrounding lesions was slightly different compared to sham but not statistically significant. Remyelination was clearly shown to return to normal index values, and interestingly a persistent highly nonpolar population of pixels remained after near complete remyelination.

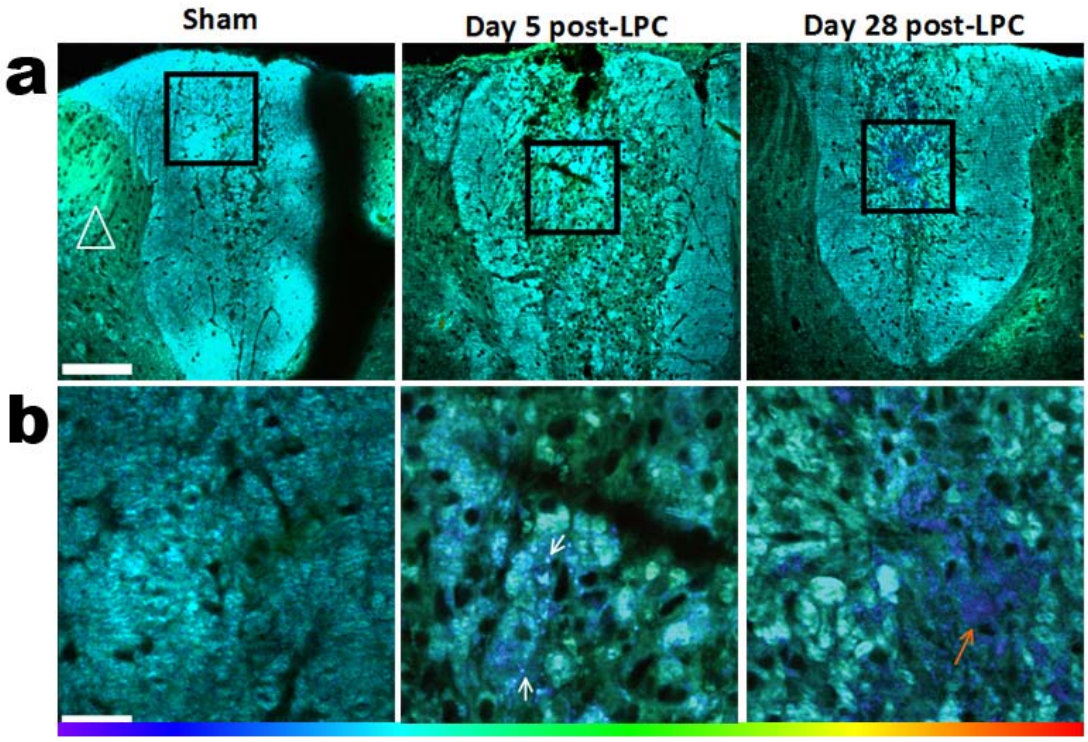

Figure 5-14. Pseudocolor images of sham and LPC induced demyelination and remyelination in an animal model

a, dorsal column cross-sectional slide showed the entire white matter and partial grey matter (white triangle area) with different pseudocolor. b, close-up view of the black box of (a). At day 5 post LPC injection, multiple puncta were observed around the lesion area (a, middle, black box); lipid droplets revealed by NR (b, middle, white arrows). At day 28 post LPC injection, lipid droplets were undetectable (orange arrow). The lesion was covered by purple pseudocolor, presumably it is the chondroitin sulfate proteoglycans[302] from glial scars[303]. a, scale bar = 100 µm; b, scale bar = 20 µm

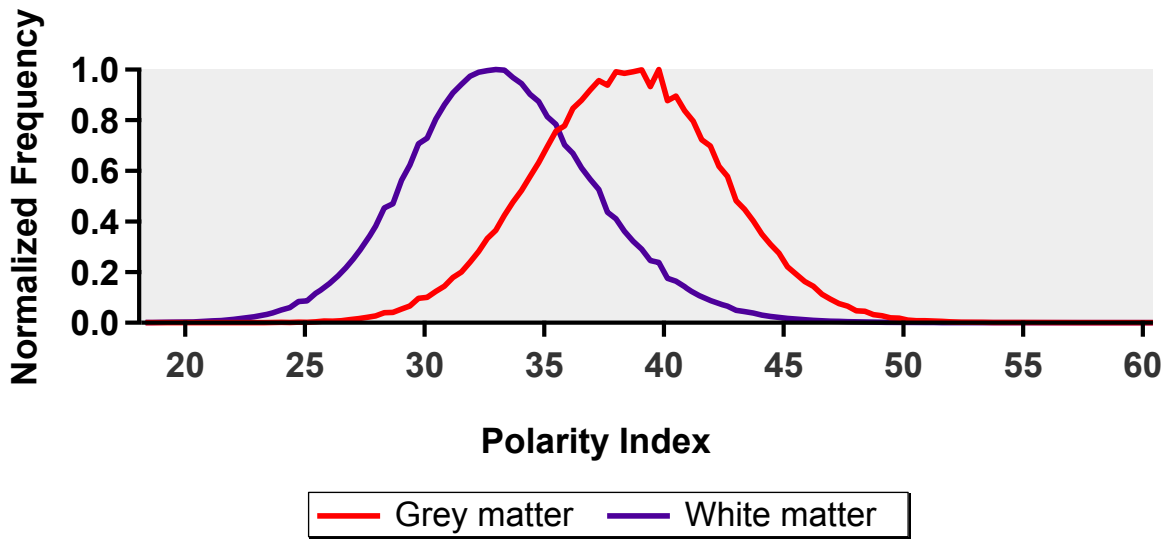

Figure 5-15. NRSSA analysis of transverse section of dorsal column white matter vs. grey matter

The areas of dorsal column white matter and dorsal horn grey matter were compared using NRSSA analysis. Grey matter was more polar than white matter (chi-square test, $p < 0.001$, $N = 3$).

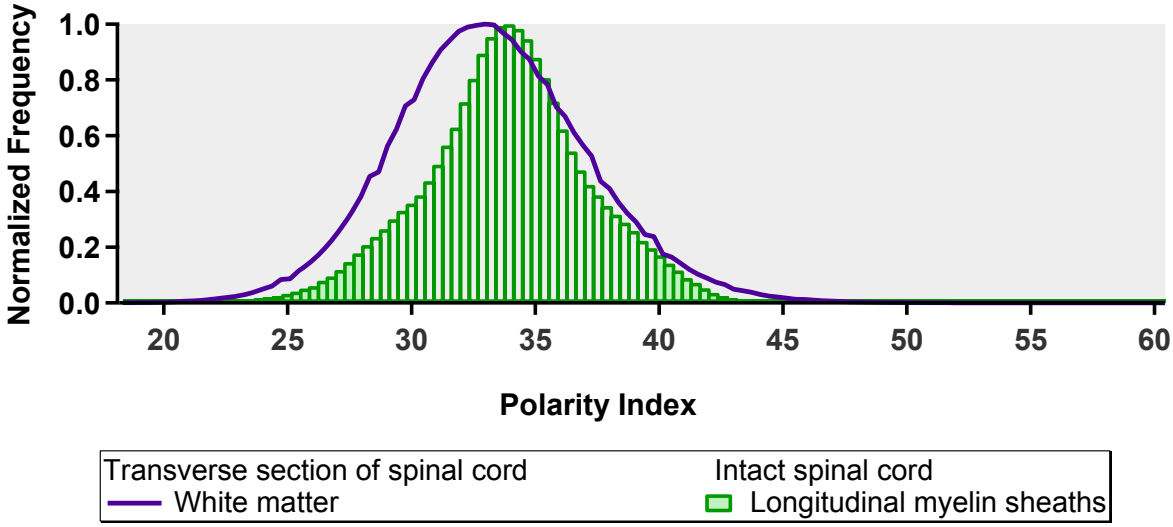

Figure 5-16. NRSSA analysis of transverse section of spinal white matter vs. longitudinal myelin sheaths

The area of transverse section white matter was compared to the area of longitudinal myelin sheaths. The readout of myelin sheaths compared to overall area of white matter shows slightly different distribution, but there is no significant difference statistically (chi-square test, transverse section of white matter vs. longitudinal myelin: $p = 1$, transverse section of white matter, $N = 3$; longitudinal myelin, $N = 10$).

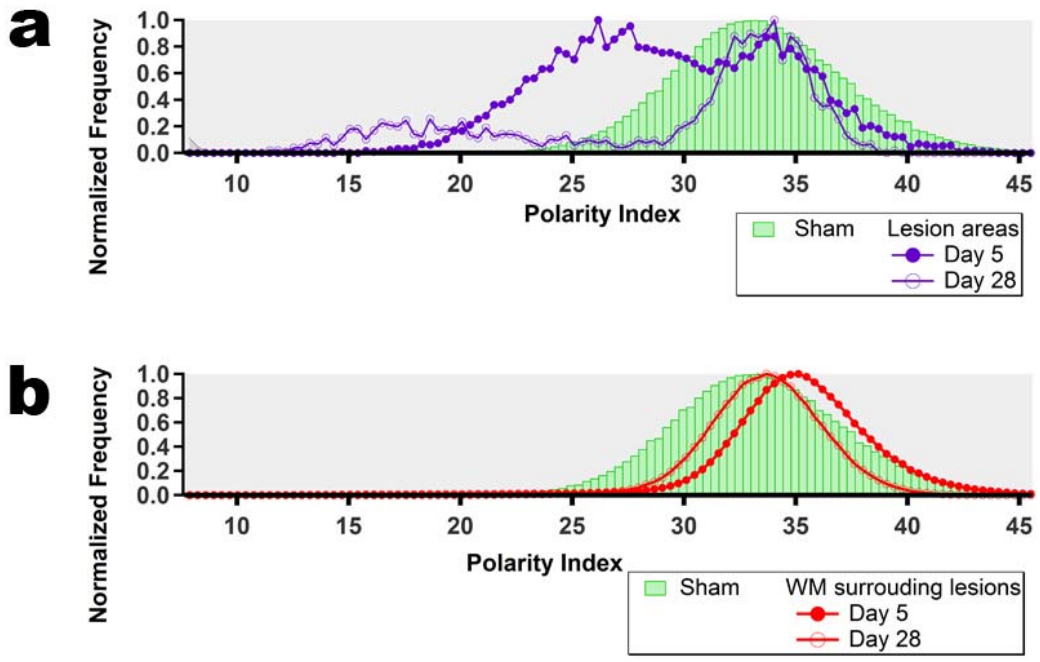

Figure 5-17 Characterization of the lesion and white matter surrounding the lesion by NRSSA analysis

At day 5, the population (a, purple solid circle) from the lesions areas was less polar than the area surrounding the lesion (b, red solid circle). At day 28, the major distribution of population at lesion areas (a, purple open circle) was similar to sham while the sub-population appeared less polar at peak index 17. Area surronding lesions (b, red open circle) was slightly different from sham.

5.4.8 Solvatochromic properties in ex vivo imaging of demyelination and remyelination via LPC injection

In the LPC experiment using transverse cryosections of fixed dorsal column, demyelination and remyelination can be detected in white matter by NRSSA. However, the above experiment cannot provide spatially resolved image of live longitudinal myelin sheaths. Live longitudinal myelin sheaths provide cellular features such as node of Ranvier and internode. These features help to recognize the myelin morphology during demyelination and remyelination. To address this issue, I combined the techniques used in LPC model and *ex vivo* imaging model of spinal cord. My goal was to image longitudinal myelin sheaths during demyelination and remyelination. I used double-transgenic mice expressing GFP in microglia/macrophages and YFP in axons at day 3 and day 36 post-LPC injection. Using fluorescent microscopy, the high intensity of GFP positive cells facilitates locating the injection site. Furthermore, the interaction between GFP positive cells and myelin sheaths defined injured myelin. Sham animals were injected with saline at day 7. The sham profile was similar to naive myelin with peak index of 38 vs. 40 (Figure 5-18, chi-square test, naive vs. sham: $p = 1$, naive, $N = 3$; sham, $N = 2$).

In general, demyelinating agent LPC induced widespread abnormalities in myelin sheaths at the lesion site 3 days post-injection. The lesion site was infiltrated by either microglial cells or/and macrophage/monocytes at day 3 consistent with previous reports[83,301]. These cells were highly phagocytic (Figure 5-19b, orange arrows), and were called “gitter cells” in lipid-laden macrophages[304]. I observed normal-appearing myelin surrounding the lesion site (Figure 5-19a yellow box); partially demyelinated axons (Figure 5-19b, long white arrows) adjacent to demyelinated axons (Figure 5-19b, short white arrows); immune cells engulfing myelin debris

(Figure 5-19c, short yellow arrows). I therefore selected these regions for NRSSA analysis. Normal-appearing myelin was less polar than sham (peak index 38 vs. 30). Comparing sham with partial demyelinated axon and immune cells engulfing myelin debris, peak index shifted 38 to 19 and 38 to 16 respectively. Interestingly, the morphology of these phenotypes that revealed a transition of myelin injury from normal-appearing myelin to immune cells engulfing myelin debris correlated to the decrease in peak index of these phenotypes based on NRSSA analysis. Polarity change in normal-appearing myelin was an indication of chemical change before exhibition of structural damage in myelin.

At day 36 post LPC injection, the injection site did not show appear and angiogenesis surrounded the scar. More importantly, myelinated axons surrounded the scar area were recognized very quickly. Their most distinct morphology showed short internodes ranges between 20 and 100 μm long (Figure 5-20). These myelinated axons were unambiguously identified as remyelination[305]. Using NRSSA analysis, a larger shift towards more polar (peak index 38 to 50) was identified (Figure 5-18, chi-square test, remyelination vs. sham: $p = 0$, remyelination, $N = 2$; sham, $N = 2$) by comparing sham and remyelination.

In sum, NRSSA showed strong contrast of polarity index in demyelination and remyelination by comparing to sham. Smaller polarity values were detected in injured myelin at day 3 whereas higher polarity values were detected during remyelination at day 36 Figure 5-18).

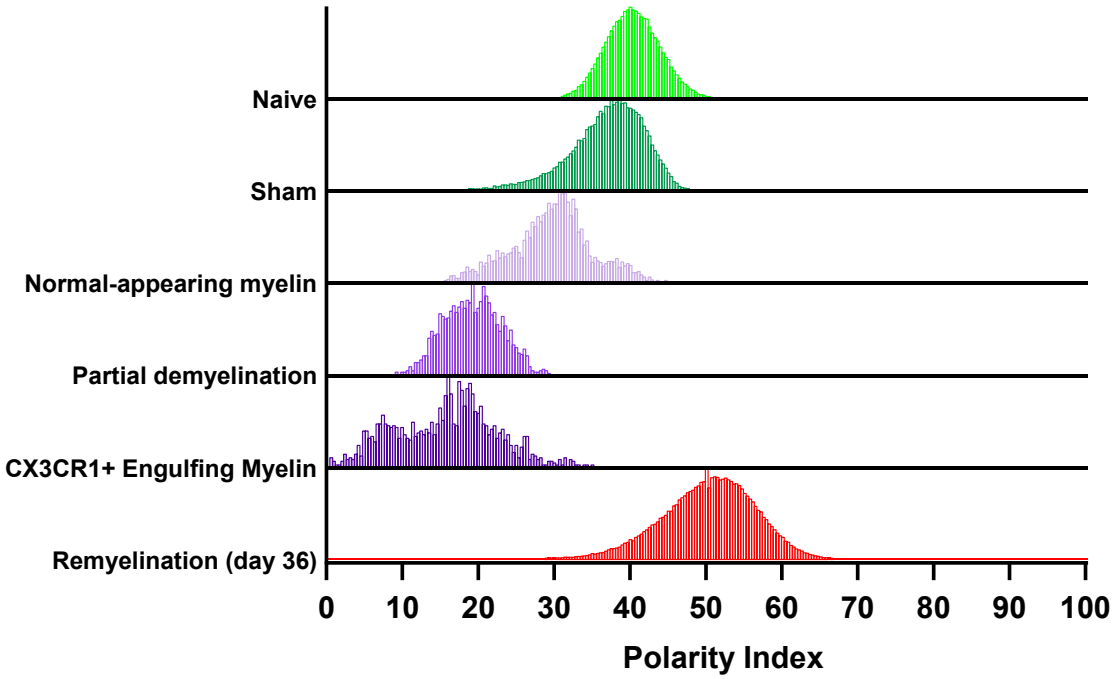

Figure 5-18. NRSSA analysis of injured myelin and remyelination in *ex vivo* dorsal column

Naive is baseline control live myelin (light green histogram). Abnormal myelin sheaths that were observed 3 days post LPC injection (three purple histograms) were less polar compared to sham (dark green histogram). Peak polarity value in normal-appearing myelin was lesser than sham. Peak polarity value of injured myelin (partial demyelination) was less polar than normal-appearing white matter. The population of myelin debris (engulfing myelin) was least polar among myelin populations. 36 days post LPC injection during the remyelination (red histogram) were more polar compared to sham.

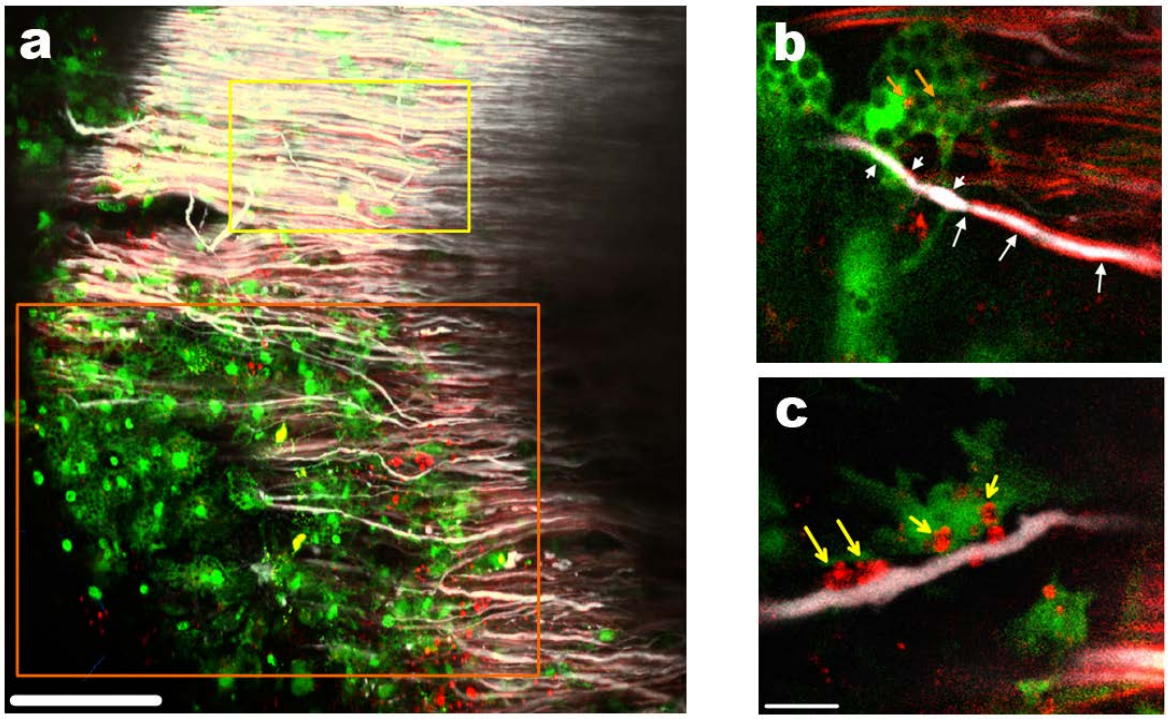

Figure 5-19. *Ex vivo* imaging of day 3 post LPC injection site in dorsal column

a, GFP-positive immune cells were at the lesion site (big orange box) and the region of normal appearing myelinated axons (yellow box) was selected for NRSSA analysis. These immune cells were lipid-laden macrophages-like shape at the lesion site. b, a partially demyelinated axon showed that a segmented myelinated axon (white long arrows) adjacent to demyelinating axon (short white arrows) was surrounded by myelin-engulfing immune cells (orange arrows). c, myelin debris (short yellow arrows) was engulfed by GFP positive cells. The axon gradually demyelinated, some abnormal myelin (long yellow arrows) was observed next to immune cells. Axon in white; monocyte in green; and myelin in red. a, scale bar = 100 μm; b and c, scale bar = 10 μm

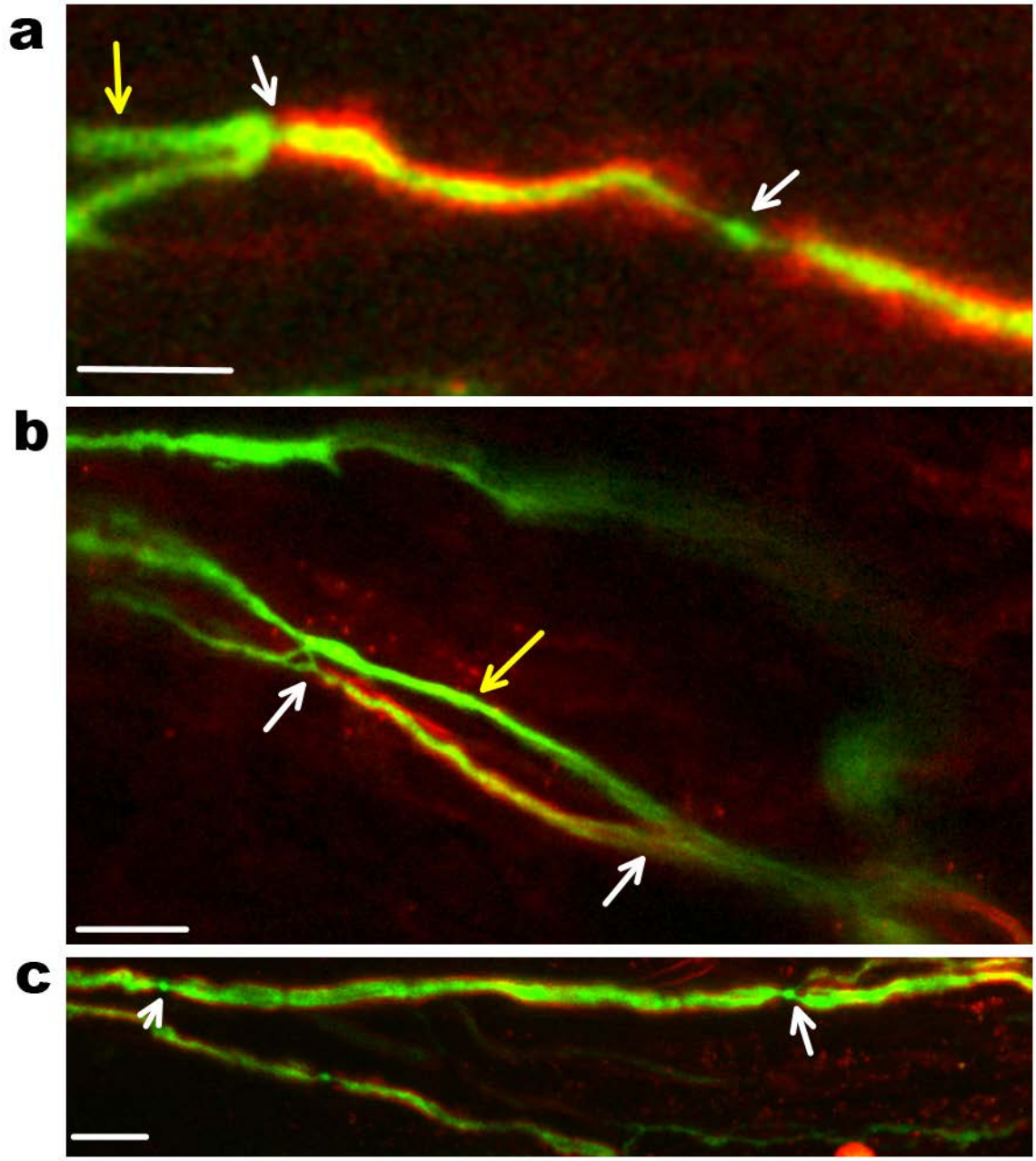

Figure 5-20. Area of remyelination with shorter internodes after day 28 post LPC injection in *ex vivo* dorsal column

Short internodes about 20 (a), 40 (b) and less than 100 µm (c) were shown (length between two white arrows) in dorsal column at the lesion site. Yellow arrows indicates demyelinated axons. Axons (green); remyelination (red); Scale bars = 10 µm

5.4.9 Solvatochromic properties in MS samples

NRSSA analysis has demonstrated the capability of detecting subtle myelin polarity changes during demyelination and remyelination in an animal model of chemical demyelination. I asked whether NRSSA could detect lipid composition changes in myelin of human MS tissue since this topic is controversial; numerous *in vitro* studies reported changes in lipid composition in myelin[235,244,247,250,306–309] while others did not[249,309,310].

Samples were taken from brain sections of patient with secondary progressive MS (Figure 5-21a-b) and patient without MS as control white matter (Figure 5-21d). In MS samples, four groups of myelin abnormality were categorized: hyper-intense rim (Figure 5-21e), diffusely-abnormal/dirty-appearing white matter (DAWM) (Figure 5-21f), normal appearing white matter (NAWM) (Figure 5-21g), and focal lesions (Figure 5-21h). Hyper-intense rim lesion defines an area where the chronic active lesion surrounded by major myelinated axons (Figure 5-21c and e). Within the lesion, many lipid-laden microphages (Figure 5-21c, yellow arrow) and axonal spheroids (Figure 5-21e) were observed. DAWM[311] are located in the poorly defined borders between focal lesion and NAWM[245], the region was identified by T2-weighted and proton density imaging. NAWM is a non-lesion white matter where myelin appeared normal. Focal lesions is an area that is completely filled with demyelinated plaques. NR easily stained all regions of myelin sheaths and focal lesions, pseudocolor images of four regions were generated using NRSSA (Figure 5-21e-h).

The lipid composition in control myelin between human and mice are different[312]. Thus, I compared myelin *in situ* between human control (74 years old) white matter and aged mice. The

human control white matter was more polar than aged mice control myelin (Figure 5-22). This might be due to the cholesterol content in normal human myelin that is twofold lower than the rodent myelin, and more phospholipid content in human than rodent[312]. I then analyzed MS tissues using NRSSA. DAWM showed a relatively homogeneous population with peak index 29, which was less polar compared to control white matter with peak index 42 (Figure 5-23). Hyper-intense rim shared similar profile with DAWM (peak index 28). NAWM exhibited bimodal distribution with peak index 13 and 28, revealing heterogeneity in myelin lipid, and showed the largest shift to less polarity among all MS samples. This is in agreement with others using MRI to identify the heterogeneous population in NAWM[313]. Focal lesions showed bimodal distribution as well (distributed with peak index 28). This suggests that the focal lesions is a lipid free environment exposed to polar environment with extracellular protein. Interestingly, the scar formation in 10 LPC-injected mouse dorsal column has almost identical polarity property as human focal lesion in MS (Figure 5-24). This might indicate that their polarity of extracellular proteins in the lesion area were similar.

Taken together, NRSSA is a powerful tool to distinguish myelin abnormality in MS. The abnormality of myelin was reflected by the decrease of polarity. The heterogeneous population in NAWM is an indication of biochemical alteration independent of the structural abnormality in myelin. This finding is potentially the breakthrough in MS clinical research study.

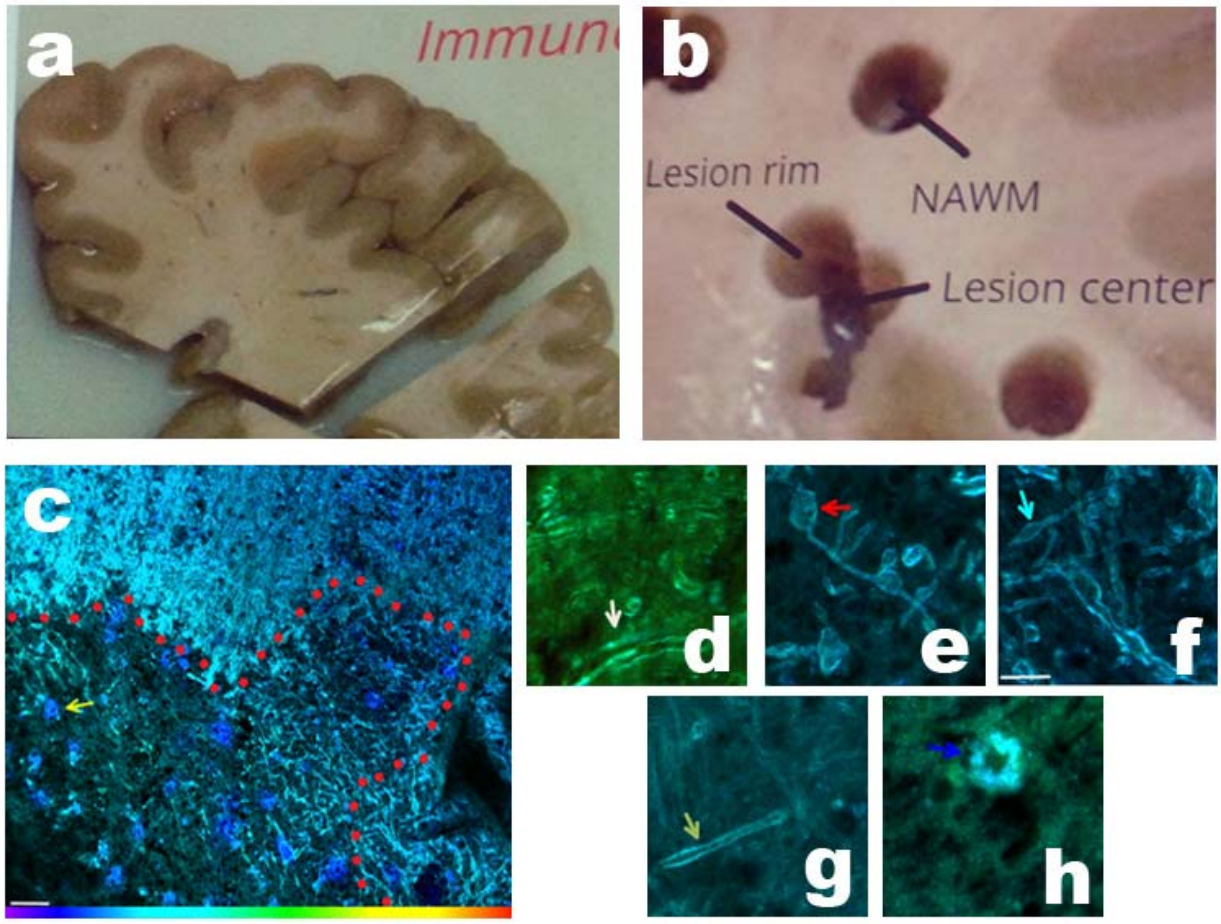

Figure 5-21. Pseudocolor images of MS lesions, brain section and punch autopsies

a and b, human brain section before (a) and after (b) performing punch autopsies. c, presentation of pseudocolor image of lesions from cross-section brain. The red dotted circle was the lesion with many lipid-laden macrophages (yellow arrow). d, myelin sheaths (white arrow) in control white matter. e, swollen myelin sheaths (red arrow) in lesion rims. f, myelin sheaths (cyan arrow) in diffusely abnormal white matter. g, myelin sheaths (green arrow) in normal appearing white matter. h, focal lesions (blue arrow). Scale bar = 50 μm

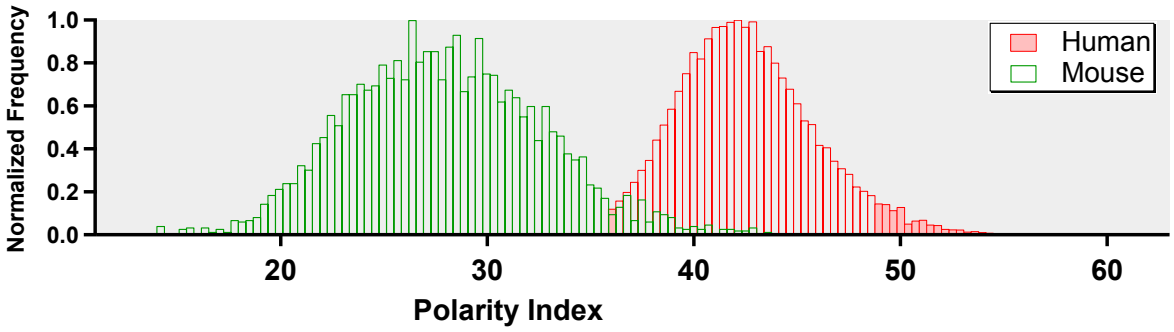

Figure 5-22. Mouse vs. Human

The comparison between fixed samples of aged mouse and human revealed that the human myelin is more polar than mouse myelin (chi-square, mouse vs. human: $p < 0.001$, mouse, $N = 2$; human, $N = 1$).

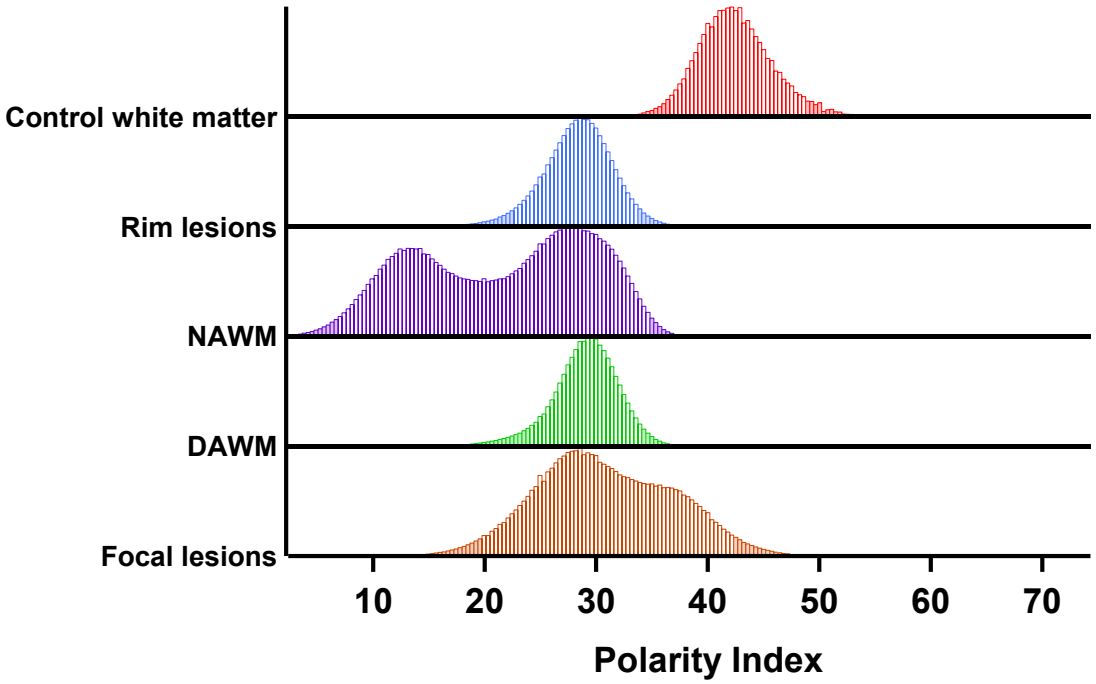

Figure 5-23. NRSSA analysis of MS tissue

Pathological changes in MS tissue: focal lesions, rim lesions, NAWM, DAWM and control white matter. Population of all MS tissues showed polarity values that were less polar than control white matter. Among the populations, NAWM and focal lesions showed bimodal distribution.

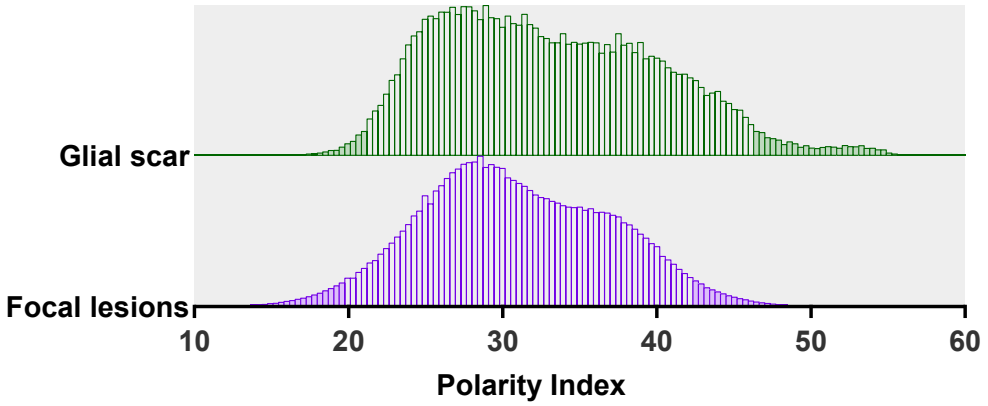

Figure 5-24. Comparison between focal lesion in MS and scar formation in day 10 LPC injected mouse dorsal column

Focal lesion in MS was very similar to the scar formation in mice after day 10 of LPC treatment (chi-square test, MS focal lesion vs. mouse scar: $p = 1$, MS focal lesion, $N = 1$; mouse scar: $N = 2$).

5.5 Discussion

In an attempt to understand myelin injury, destructive methods of analysis such as HPLC and TLC have been widely used. Electron microscopy and immunostaining are used to identify the morphology of myelin and myelin protein distribution respectively. Here I demonstrated that combining the *ex vivo* model that I described in Chapter 3 and NRSSA analysis, a novel method that cannot be achieved using traditional methods, allowed simultaneous tracking of the morphology and biochemistry of live myelin. NRSSA is a powerful method in many ways.

First, the staining procedure used in NRSSA is straightforward and can easily be achieved in the laboratory. NR is affordable and accessible commercially. In my study, NR brightly stained intact myelin and revealed the structural system of myelin in a spatially-resolved manner. This staining method requires only 30 minutes or less to stain intact spinal cord while the traditional method of immunostaining requires a much longer period of time to review the morphology of myelin[314]. Moreover, labeling is non-destructive and therefore less likely to introduce confounding variables[315] (e.g. stability of antibody and penetration of antibody) than conventional immuno-based methods.

Second, I asked whether NRSSA can serve as a global analysis tool in myelin research. I therefore applied NRSSA in various myelin samples: myelin *in vitro*, fixed myelin *in situ*, live *ex vivo* myelin, transverse sections of white matter and human myelin. NRSSA analysis revealed that the range of polarity values in these models can be resolved in the same scale of polarity index, indicating that the analysis was compatible for comparisons with various myelin samples. For example, in physiological condition, a globular form of isolated myelin shared similar profile

with intact live myelin (Figure 5-9); in pathological condition, focal lesion in MS shared similar profile with scar formation in mice treated with LPC (Figure 5-24).

Third, in MS tissue, NRSSA analysis was sensitive in distinguishing the control white matter from abnormal myelin even before myelin undergoes pathomorphological changes. For example, NAWM was morphologically "normal" compared to intact myelin but NRSSA detected a heterogeneous population of biochemistry in myelin (Figure 5-23). Indeed, NAWM has also been observed to precedes the lesion[316]; an early sign of MS. In addition, NRSSA detected the decrement in polarity value from sham to normal appearing myelin to injured myelin, and finally engulfed myelin (Figure 5-19c) in the animal model. The polarity shift (Figure 5-23) was in agreement with the morphological change of myelin. Furthermore, I showed that biochemistry profile in adult live myelin during remyelination was more polar than normal myelin (Figure 5-18) but similar to developing myelin, suggesting that new myelin sheaths generated during remyelination underwent a repair process similar to developing myelin but chemically immature compared to normal myelin. This finding is consistent with the recapitulation hypothesis[317] in that the process of remyelination converges with the process of developing myelin.

While the NRSSA method appears highly sensitive to subtle biochemical changes in various myelin conditions, it lacks specificity. NRSSA can only present the whole population of lipid composition. Nonetheless, NRSSA can serve as a sensitive indicator to detect early sign of demyelination and remyelination.

5.6 Conclusion

In combining detailed imaging of myelin with NRSSA analysis, not only can polarity changes be detected in early de- and re-myelination, but the dynamic biochemical polarity can also be traced from a single adult myelin sheath. NRSSA is a powerful technique that adds significant capabilities to the toolbox for *in vitro*, *ex vivo* and possibly *in vivo* imaging for the CNS (and potentially the PNS in the future) in animal models and human. NRSSA not only has great potential in the basic biomedical research, but also the clinical application to detect early signs of demyelination and remyelination in MS patients.

Chapter Six: General discussion

The goals of this thesis are to investigate the cellular mechanism and morphological change of axon spheroid formation (ASF) and the development of fluorescence-based tools to study myelin injury in the central nervous system (CNS).

6.1 The model

I used a live *ex vivo* adult mouse dorsal column model to study CNS white matter microscopically at high resolution. The mouse model offers a major advantage of allowing the study of various transgenic lines to address specific biological questions. In order to monitor fine structural as well as biochemical changes to small-diameter CNS axons and myelin over many hours, I had to make a number of optimizations. First, I custom-designed the tissue imaging holder to prevent direct physical contact with the dissected cervical spinal cord while at the same time holding the cord securely for microscopy. This seemingly trivial requirement was essential to reduce spatial drift over the many hours I needed for imaging of the same region of interest, and allowed me to follow structural changes of individual axons over time. The CNS is exceptionally sensitive to physical trauma; my apparatus not only provided excellent stabilization of the preparation, but also minimized any physical trauma to the fine dorsal column fibers that were imaged. Even after 8-10 hours, there was virtually no morphological injury to the axons under control conditions (Figure 4-3a). Second, I took advantage of selective axonal yellow fluorescent protein (YFP)-expression in the transgenic mouse combined with bright myelin labeling using lipophilic vital dyes to visualize fine details including nodes of Ranvier and subtle axo-myelinic pathology. The cervical region was chosen because the region of dorsal column is wider (around 200-300 μm) so that the peripheral nerves from dorsal roots can be

easily identified and excluded. The "Y" shape of the brainstem-cervical cord junction provided physical orientation of the proximal vs. distal segments of the cord. Third, use of intracardiac perfusion to flush blood vessels was necessary to improve optical clarity (Figure 3-1b). Taken together, I developed an optimized model for relatively long-term (many hours) high resolution imaging of fine structure of CNS axons and their myelin, where, in contrast to the true *in vivo* situation, precise environmental control (e.g. drug application) was possible to allow dissection of molecular mechanisms of various pathologies.

6.2 Glutamate-induced ASF

In Chapter 4, I demonstrated that overactivation of glutamate receptors induced ASF in myelinated dorsal column axons. Somewhat surprisingly, glutamate itself induced only modest pathology which was delayed, in agreement with previous studies[169]. My results showed that the blunting of axo-myelinic glutamate toxicity was in large part due to robust uptake of this transmitter by endogenous glutamate transporters; co-application of the selective glutamate transport inhibitor TBOA greatly exacerbated excitotoxic injury (Figure 4-8). Glutamate transporters are found in neuron[318], axons[204] and glial cells[319] and spinal cord white matter[12,320]. The function of glutamate transporters is to prevent glutamate toxicity by removal of extracellular glutamate into the intracellular compartment[211] so that the concentration of extracellular glutamate can be maintained between 0.5-5.0 μM level[321,322]. Transport systems necessary to maintain physiological neurotransmitter concentrations in the extracellular space require normal gradients of the major cations such as Na^+ and K^+[323]. These gradients in turn depend on ion pumps that require ATP[172]. Therefore I predicted that even modest impairments of energy production by sublethal concentrations of mitochondrial function inhibitors (e.g. 0.5 mM

NaN_3), concentrations that by themselves did not induce any structural white matter damage, would greatly increase the sensitivity of white matter to glutamate by virtue of partial compromise of transmitter uptake systems. This was indeed the case: on a background of sub-injurious chemical hypoxia, white matter axons became exquisitely sensitive to exogenous glutamate at concentrations that were same as control, where ASF only started to appear at 10 hours. This observation has major implications for our understanding of MS pathophysiology where 3 events will conspire to induce axonal injury: 1) it is known that glutamate levels are increased in MS brain[324], and will be particularly elevated in regions of acute inflammation[129,325] 2) glutamate transporters are reduced in the MS brain[130,176], and 3) the chronic MS brain exists in an environment of relative "virtual hypoxia"[24,139], because of impaired energy production from mitochondrial dysfunction[326,327] and increased energy demands due to chronically demyelinated and ionically leaky axons[328,329]. My experiments indicate that such an environment is particularly toxic to CNS axons and help to explain the progressive and widespread axonal degeneration seen in the early and progressive stages of this disease.

The leptomeninges also provided a substantial barrier to exogenous glutamate addition (Figure 4-13). Whether this is relevant *in vivo* is questionable because any source of excitotoxic substances would likely be behind the blood brain barrier[206] (e.g. from infiltrating immune cells). Nevertheless, this observation is an important methodological issue for *ex vivo* experiments such as mine where pharmacological agents are bath-applied.

My model faithfully reproduced the focal axonal swellings seen ubiquitously in MS and other CNS disorders affecting white matter[9,330]. Calcium influx through axonal glutamate receptors[32,33]

with subsequent overactivation of calcium-dependent enzymes such as calpains[331] with digestion of cytoskeletal proteins including neurofilament, microtubule and spectrin[332], was likely responsible. This has been shown in previous studies[189]. Interestingly, I frequently observed dark puncta devoid of YFP, adjacent to the inner surface of the axolemma. The exclusion of soluble YFP from these puncta indicates that they are membrane-bound organelles. Their configuration is not consistent with the elongated mitochondria that I imaged in axons (Figure 3-6j), but is most consistent with swollen subaxolemmal ER ("axoplasmic reticulum")[143,216]. ER is a well known calcium-containing organelle in many cells, including axons[216]. Previous data have shown that calcium release from this pool significantly contributes to axonal injury[183]. I therefore asked whether the glutamate-induced excitotoxic injury to dorsal column axons may have been caused in part by calcium release from axonal AR. Direct release of calcium from AR by caffeine[333] induced pronounced ASF which was blocked by ryanodine, an antagonist caffeine-induced, ryanodine receptor-mediated ER calcium release. This underscores the central role that axonal ER plays in the induction of axonal pathology. Most intriguing was my observation that ryanodine also blocked glutamate-induced ASF almost completely (Figure 4-18). While axonal glutamate receptors play a central role in ASF formation, and may permeate some calcium into the axon from the extracellular space, this unexpected finding implies that most of the injurious calcium originates from the axonal ER, not from influx across the axolemma. Exogenous glutamate may trigger this release through calcium-induced calcium release (whereby a small amount of calcium influx induces a much larger release from intra-axonal stores[33,334]) or via a non-canonical metabotropic mechanism[335,336]. This expanded understanding of excitotoxic axonal degeneration may have important implications for therapeutic design in MS where prevention of progressive axonopathy is of paramount importance.

6.3 Solvatochromism for the study of myelin pathology

In MS and other white matter disorders, detailed histopathology, together with specialized chemical and more recently immunochemical myelin stains, has been the mainstay for the study of myelin degeneration and demyelination[16,43]. These techniques are relatively insensitive to early myelin pathology where biochemistry may change first, before any evidence of overt structural change. Indeed, detailed ultrastructural examination reveals subtle changes in inner myelin loops in early MS lesions before frank demyelination is apparent[337,338], but tissue preparation and examination under electron microscopy is very labour-intensive and prone to artefact. On the other hand, detailed biochemical analysis on myelin has been done to examine changes during development and disease states[238,339]. For instance, immature myelin contains more polar lipids (mainly phospholipids[238,340]) and as myelin ages, its character becomes less polar as it accumulates relatively more nonpolar cholesterol and its esters[292]. A similar shift occurs during the early stages of demyelination[244,307]. While precise and quantitative, such biochemical analyses require that myelin be homogenized for high-performance liquid chromatography or mass spectrometry, destroying and spatial information or heterogeneity that may be highly informative in otherwise intact fixed tissue.

Lipophilic fluorescent probes are frequently used to stain cell membranes and given the high density of lipid-rich membrane wraps in compact myelin, brightly stain myelin sheaths in both CNS[268,269] (Figure 3-6, Figure 3-7) and peripheral nervous system[270] because of their large increase in quantum yield (and therefore brightness) when they partition into the much less polar environment of cell membranes[341,342]. In addition to quantum yield changes as a function of local

physico-chemical environment, some fluorescent probes additionally undergo changes in their absorption and emission spectra[343,344] (Figure 5-2a), a phenomenon termed solvatochromism[345].

Solvatochromism is a fairly common property of many fluorophores and chromophores; the commonly used histological dye eosin exhibits solvatochromic behaviour which accounts for the various hues it imparts to different cells and tissues during conventional staining[346,347]. I selected NR for detailed study because this lipophilic probe stains myelin brightly, and was predicted to undergo large shifts in emission spectrum in various environments based on published data[348]. I confirmed this using pure dye dissolved in solvents of various polarities (Figure 5-3a). By considering that myelin is the "solvent" when stained with these dyes, I further predicted that changes in myelin biochemistry, and therefore its physico-chemical properties such as viscosity and polarity (both of which strongly influence spectral properties of solvatochromic dyes[343,349]), would be reported by NR. This prediction was confirmed by various experiments, including aging myelin, transgenics targeting myelin protein makeup, and most interesting to MS research, early de- and re-myelination (Figure 5-19, Figure 5-20, Figure 5-21).

The major advantage of image-based spectral microscopy is the ability to acquire data in a spatially-resolved manner, maintaining normal spatial relationships between cells and tissue elements. Averaged spectral shifts from such images however, were not very sensitive at detecting subtle shifts that may be present in very localized regions. To increase sensitivity, I developed the Nile red solvatochromic shift assay (NRSSA) which extracts a histogram at pixel-by-pixel resolution of all the various spectral shapes emitted by the one probe from different locations in the image. This not only yields average spectral shape (peak of the histogram)

between two extreme bracketing spectra, but also the heterogeneity in spectral shapes reflected by the width of the histogram and possibly multiple peaks (Figure 5-6a), indicating two or more distinct chemical species in the image. This method has proven to be exquisitely sensitive at detecting even very subtle chemical shifts; for instance, the NRSSA method was able to clearly distinguish control white matter from morphologically intact normal-appearing white matter in human MS brain (Figure 5-23). This indicates that otherwise normal MS white matter had undergone fundamental biochemical change in areas well beyond and inflammatory lesions, supporting the hypothesis that MS is a widespread abnormality of the CNS white matter. These results are in line with data from specialized MRI sequences performed on MS patients that also suggest widespread diffuse abnormalities of otherwise intact CNS white matter[245,313]. Equally interesting was my observation that remyelinated myelin had a biochemical profile that was similar to immature myelin at early developmental stages (Figure 5-12, Figure 5-18), suggesting a reversion to early immature phenotypes during repair[317].

While the NRSSA method appears very sensitive to subtle biochemical changes in myelin development, injury and repair, it lacks specificity. Detailed biochemical analyses of homogenized samples yield precise compositions of a variety of known lipids[255,350]. The NRSSA method can only report changes in polarity (determined mainly by cholesterol and phospholipid composition in myelin), but cannot report proportions of the many lipid constituents. Nevertheless, the NRSSA technique can be used as a sensitive indicator of lipid chemical changes, and therefore can identify the earliest stages of myelin injury, while maintaining intact spatial relationships in tissue sections that can be very informative regarding potential

pathophysiological mechanisms (for instance, does myelin lipid biochemistry change early when an axon is engaged by an immune cell?). This will the subject of future experimentation.

6.4 Future directions

My data conclusively show the central role played by glutamate receptors in producing structural axonal injury. Future experiments can be designed to elucidate precisely which receptors are involved. Indeed, the unexpected major involvement of axonal calcium stores raises the possibility that metabotropic glutamate receptors also play a role[170], and this family of receptors, together with downstream pathways and protective pharmacology could be explored further.

I also showed that solvatochromism, together with custom post-processing of spectral micrographs, is a powerful method for detecting subtle biochemical changes in myelin. Major efforts are underway to develop repair strategies for MS by promoting remyelination either from intrinsic progenitors or extrinsic elements[50,351]. This method may be very powerful to detect and quantitate success or failure of various remyelination strategies in animal models.

6.5 Conclusion

This thesis demonstrated an *ex vivo* model for tracking axonal swelling/transection and the cardinal feature of irreversible white matter pathology. ASF is driven by glutamate-mediated excitotoxicity and local dysregulation of calcium homeostasis. This leads to focal structural changes in axons. Additionally, I established a novel tool using solvatochromic principle to investigate the lipid biochemistry in live myelin. The experiments proposed in the future direction section of my thesis together with data I have gathered will enable us to gain a better

understanding of the cellular and molecular mechanisms of axon and myelin injury, and importantly, define specific directions for future therapeutic design.

References

1. Lassmann, H. Axonal injury in multiple sclerosis. *J Neurol Neurosurg Psychiatry* **74,** 695–697 (2003).

2. Steinman, L. Multiple sclerosis: A coordinated immunological attack against myelin in the central nervous system. *Cell* **85,** 299–302 (1996).

3. Back, S. A. *et al.* Selective Vulnerability of Late Oligodendrocyte Progenitors to Hypoxia – Ischemia. **22,** 455–463 (2002).

4. McTigue, D. M. & Tripathi, R. B. The life, death, and replacement of oligodendrocytes in the adult CNS. *J. Neurochem.* **107,** 1–19 (2008).

5. Stys, P. Anoxic and ischemic injury of myelinated axons in CNS white matter: from mechanistic concepts to therapeutics. *J. Cereb. Blood Flow Metab.* **18,** 2–25 (1998).

6. Sarma, J. & Kenyon, L. Mechanisms of primary axonal damage in a viral model of multiple sclerosis. *J.* … **29,** 10272–10280 (2009).

7. Semba, S., Sawa, H. & Nagashima, K. Mechanism of white matter damage caused by virus infection. *Int. Congr. Ser.* **1251,** 139–147 (2003).

8. Medana, I. M. & Esiri, M. M. Axonal damage: a key predictor of outcome in human CNS diseases. *Brain* **126,** 515–530 (2003).

9. Trapp, B. D. *et al.* Axonal transection in the lesions of multiple sclerosis. *N. Engl. J. Med.* **338,** 278–85 (1998).

10. Pantoni, L., Garcia, J. H., Gutierrez, J. A. & Rosenblum, W. I. Cerebral White Matter Is Highly Vulnerable to Ischemia. *Stroke* **27,** 1641–1647 (1996).

11. Kraus, M. F. *et al.* White matter integrity and cognition in chronic traumatic brain injury: A diffusion tensor imaging study. *Brain* **130,** 2508–2519 (2007).

12. Li, S., Mealing, G. A., Morley, P. & Stys, P. K. Novel injury mechanism in anoxia and trauma of spinal cord white matter: glutamate release via reverse Na+-dependent glutamate transport. *J. Neurosci.* **19,** RC16 (1999).

13. Li, S. & Stys, P. Mechanisms of ionotropic glutamate receptor-mediated excitotoxicity in isolated spinal cord white matter. *J. Neurosci.* **20,** 1190–1198 (2000).

14. Tasaki, I. The electro-saltatory transmission of the nerve impulse and the effect of narcosis upon the nerve fiber. *Am. J. Physiol. Content* **127,** 211–227 (1939).

15. Stiefel, K. M., Torben-Nielsen, B. & Coggan, J. S. Proposed evolutionary changes in the role of myelin. *Front. Neurosci.* **7,** 202 (2013).

16. Waxman, S. *Multiple Sclerosis As A Neuronal Disease*. (Academic Press, 2005).

17. Peters, A., Palay, S. & Webster, H. deF. The fine structure of the nervous system: neurons and their supporting cells. (1991).

18. Brady, S., Siegel, G., Albers, R. & Price, D. *Basic neurochemistry: molecular, cellular and medical aspects*. (2005).

19. Bhat, M. A. *et al.* Axon-glia interactions and the domain organization of myelinated axons requires Neurexin IV/Caspr/Paranodin. *Neuron* **30,** 369–383 (2001).

20. Salzer, J. Polarized domains of myelinated axons. *Neuron* **40,** 297–318 (2003).

21. Blakemore, W. Schmidt-Lantermann incisures in the central nervous system. *J. Ultrastruct. Res.* **498,** 496–498 (1969).

22. Hall, S. M. & Williams, P. L. Studies on the 'incisures' of Schmidt and Lanterman. *J. Cell Sci.* **6,** 767–91 (1970).

23. Yin, X., Kidd, G. J., Nave, K.-A. & Trapp, B. D. P0 protein is required for and can induce formation of schmidt-lantermann incisures in myelin internodes. *J. Neurosci.* **28,** 7068–73 (2008).

24. Trapp, B. & Stys, P. Virtual hypoxia and chronic necrosis of demyelinated axons in multiple sclerosis. *Lancet Neurol.* **8,** 280–91 (2009).

25. Nave, K. Myelination and the trophic support of long axons. *Nat. Rev. Neurosci.* **11,** 275–283 (2010).

26. Cajal, S. y. Degeneration & regeneration of the nervous system. *New York; Harper Press* (1928).

27. Waller, A. Experiments on the section of the glossopharyngeal and hypoglossal nerves of the frog, and observations of the alterations produced thereby in the structure of their. *Philos. Trans. R. Soc. London* **140,** 423–429 (1850).

28. Ferguson, B., Matyszak, M. K., Esiri, M. M. & Perry, V. H. Axonal damage in acute multiple sclerosis lesions. *Brain* **120 (Pt 3,** 393–399 (1997).

29. Kerschensteiner, M. & Schwab, M. In vivo imaging of axonal degeneration and regeneration in the injured spinal cord. *Nat. Med.* **11,** 572–577 (2005).

30. Waxman, S., Black, J., Ransom, B. & Stys, P. Protection of the axonal cytoskeleton in anoxic optic nerve by decreased extracellular calcium. *Brain Res.* **614,** 137–145 (1993).

31. George, E., Glass, J. & Griffin, J. Axotomy-Induced Axonal Degeneration is mediated by calcium Influx Through Ion-Specific Channels. *J. Neurosci.* **75,** (1995).

32. Ouardouz, M. *et al.* Glutamate receptors on myelinated spinal cord axons: I. GluR6 kainate receptors. *Ann. Neurol.* **65,** 151–9 (2009).

33. Ouardouz, M. *et al.* Glutamate receptors on myelinated spinal cord axons: II. AMPA and GluR5 receptors. *Ann. Neurol.* **65,** 160–6 (2009).

34. Stirling, D. P. & Stys, P. K. Mechanisms of axonal injury: internodal nanocomplexes and calcium deregulation. *Trends Mol. Med.* **16,** 160–70 (2010).

35. FRIEDE, R. L. The relationship of body size, nerve cell size, axon length, and glial density in the cerebellum. *Proc. Natl. Acad. Sci. U. S. A.* **49,** 187–93 (1963).

36. Lobato, R. D. Historical vignette of Cajal's work 'Degeneration and regeneration of the nervous system' with a reflection of the author. *Neurocir.* **19,** 456–468 (2008).

37. Miller, D. J. *et al.* Prolonged myelination in human neocortical evolution. *Proc. Natl. Acad. Sci.* **109,** 16480–16485 (2012).

38. Peters, A. & Sethares, C. Aging and the Myelinated Fibers in Prefrontal Cortex and Corpus Callosum. *October* **291,** 277–291 (2002).

39. Kohama, S., Rosene, D. & Sherman, L. Age-related changes in human and non-human primate white matter: from myelination disturbances to cognitive decline. *Age (Omaha).* **34,** 1093–1110 (2012).

40. Marner, L., Nyengaard, J. R., Tang, Y. & Pakkenberg, B. Marked loss of myelinated nerve fibers in the human brain with age. *J. Comp. Neurol.* **462,** 144–52 (2003).

41. Peters, A. The effects of normal aging on myelin and nerve fibers: a review. *J. Neurocytol.* **31,** 581–93 (2003).

42. Haroutunian, V. *et al.* Myelination, oligodendrocytes, and serious mental illness. *Glia* 1–34 (2014). doi:10.1002/glia.22716

43. Peterson, J. W. & Trapp, B. D. Neuropathobiology of multiple sclerosis. *Neurol Clin* **23,** 107–29, vi–vii (2005).

44. World Health Organisation. *Atlas: Multiple Sclerosis Resources in the World*. *Vasa* (2008). doi:ISBN 978 92 4 156375 8

45. Mayr, W. T. *et al.* Incidence and prevalence of multiple sclerosis in Olmsted County, Minnesota, 1985-2000. *Neurology* **61,** 1373–1377 (2003).

46. Larsson, H. B. W. & Nordenbo, a. with Acute Attack of Multiple Sclerosis *. *Magn. Reson. Med* **11,** 337–348 (1989).

47. Noseworthy, J. H., Lucchinetti, C., Rodriguez, M. & Weinshenker, B. G. Multiple sclerosis. *N. Engl. J. Med.* **343,** 938–952 (2000).

48. Lublin, F. D. Clinical features and diagnosis of multiple sclerosis. *Neurol. Clin.* **23,** 1–15, v (2005).

49. Hawker, K. Progressive Multiple Sclerosis: Characteristics and Management. *Neurol. Clin.* **29,** 423–434 (2011).

50. Stys, P. & Zamponi, G. Will the real multiple sclerosis please stand up? *Nat. Rev.* … **13,** 507–514 (2012).

51. Stys, P. K. Pathoetiology of multiple sclerosis: are we barking up the wrong tree? *F1000Prime Rep.* **5,** 20 (2013).

52. Stys, P. General mechanisms of axonal damage and its prevention. *J. Neurol. Sci.* **233,** 3–13 (2005).

53. Statistics Canada. (2012).

54. SCI Facts | Spinal Cord Injury Canada. at <http://sci-can.ca/resources/sci-facts/>

55. Pickett, G. E., Campos-Benitez, M., Keller, J. L. & Duggal, N. Epidemiology of traumatic spinal cord injury in Canada. *Spine (Phila. Pa. 1976).* **31,** 799–805 (2006).

56. The Brain Injury Association of Canada. at <http://biac-aclc.ca/>

57. Schwartz, G. & Fehlings, M. G. Secondary injury mechanisms of spinal cord trauma: a novel therapeutic approach for the management of secondary pathophysiology with the sodium channel blocker riluzole. *Prog Brain Res* **137,** 177–190 (2002).

58. *Mechanisms of Secondary Brain Damage*. (Springer Vienna, 1993). doi:10.1007/978-3-7091-9266-5

59. MAXWELL, W. A mechanistic analysis of nondisruptive axonal injury: a review. *J.* … **14,** (1997).

60. Pettus, E. H. & Povlishock, J. T. Characterization of a distinct set of intra-axonal ultrastructural changes associated with traumatically induced alteration in axolemmal permeability. *Brain Res* **722,** 1–11 (1996).

61. Povlishock, J. T., Becker, D. P., Cheng, C. L. & Vaughan, G. W. Axonal change in minor head injury. *J. Neuropathol. Exp. Neurol.* **42,** 225–42 (1983).

62. Shi, R., Asano, T., Vining, N. C. & Blight, a R. Control of membrane sealing in injured mammalian spinal cord axons. *J. Neurophysiol.* **84,** 1763–9 (2000).

63. Bartzokis, G. Age-related myelin breakdown: A developmental model of cognitive decline and Alzheimer's disease. *Neurobiol. Aging* **25,** 5–18 (2004).

64. Bartzokis, G. Alzheimer's disease as homeostatic responses to age-related myelin breakdown. *Neurobiol. Aging* **32,** 1341–71 (2011).

65. Brun, a & Englund, E. A white matter disorder in dementia of the Alzheimer type: a pathoanatomical study. *Ann. Neurol.* **19,** 253–262 (1986).

66. Bozzali, M. White matter damage in Alzheimer's disease assessed in vivo using diffusion tensor magnetic resonance imaging. *J. Neurol. Neurosurg. Psychiatry* **72,** 742–746 (2002).

67. Teipel, S. J. *et al.* Progression of corpus callosum atrophy in Alzheimer disease. *Arch. Neurol.* **59,** 243–248 (2002).

68. Pak, K., Chan, S. & Mattson, M. Presenilin-1 mutation sensitizes oligodendrocytes to glutamate and amyloid toxicities, and exacerbates white matter damage and memory impairment in mice. *Neuromolecular Med.* **3,** 53–64 (2003).

69. Fusar-Poli, P. & Politi, P. Paul Eugen Bleuler and the birth of schizophrenia (1908). *Am. J. Psychiatry* **165,** 1407 (2008).

70. Knapp, M., Mangalore, R. & Simon, J. The global costs of schizophrenia. *Schizophr. Bull.* **30,** 279–293 (2004).

71. SCHIZOPHRENIA. *National Alliance on Mental Illness* (2011). at <http://www.schizophrenia.ca/learn_more_about_schizophrenia.php>

72. Goeree, R. *et al.* The economic burden of schizophrenia in Canada. *Can. J. Psychiatry* **44,** 464–472 (1999).

73. Flynn, S. W. *et al.* Abnormalities of myelination in schizophrenia detected in vivo with MRI , and post-mortem with analysis of oligodendrocyte proteins. 811–820 (2003). doi:10.1038/sj.mp.4001337

74. Hakak, Y. *et al.* Genome-wide expression analysis reveals dysregulation of myelination-related genes in chronic schizophrenia. *Proc. Natl. Acad. Sci. U. S. A.* **98,** 4746–4751 (2001).

75. Tkachev, D., Mimmack, M. L., Huffaker, S. J., Ryan, M. & Bahn, S. Further evidence for altered myelin biosynthesis and glutamatergic dysfunction in schizophrenia. *Int. J. Neuropsychopharmacol.* **10,** 557–63 (2007).

76. Vargas, M. E. & Barres, B. A. Why is Wallerian degeneration in the CNS so slow? *Annu Rev Neurosci* **30,** 153–179 (2007).

77. Oertle, T., Fritsche, J., Mckinney, R. A. & Bandtlow, C. E. Nogo-A and Myelin-Associated Glycoprotein Mediate Neurite Growth Inhibition by Antagonistic Regulation of RhoA and Rac1. **22,** 10368–10376 (2002).

78. Filler, A. The History, Development and Impact of Computed Imaging in Neurological Diagnosis and Neurosurgery: CT, MRI, and DTI. *Nat. Preced.* 1–76 (2009). doi:10.1038/npre.2009.3267.5

79. Greenberg, D. A., Aminoff, M. J. & Simon, R. P. *Clinical Neurology*. (2002).

80. Cree, B. a C. 2014 Multiple Sclerosis Therapeutic Update. *The Neurohospitalist* **4,** 63–5 (2014).

81. Misgeld, T. & Kerschensteiner, M. In vivo imaging of the diseased nervous system. *Nat. Rev. Neurosci.* **7,** 449–63 (2006).

82. Fern, R. F., Matute, C. & Stys, P. K. White matter injury: Ischemic and nonischemic. *Glia* **62,** 1780–9 (2014).

83. Gehrmann, J., Matsumoto, Y. & Kreutzberg, G. W. Microglia: intrinsic immuneffector cell of the brain. *Brain Res. Brain Res. Rev.* **20,** 269–87 (1995).

84. Fiacco, T. A., Agulhon, C. & McCarthy, K. D. Sorting out astrocyte physiology from pharmacology. *Annu. Rev. Pharmacol. Toxicol.* **49,** 151–74 (2009).

85. K, Helmutettenmann, B. R. R. *Neuroglia*. (Oxford University Press, 2005).

86. Faulkner, J. R. *et al.* Reactive astrocytes protect tissue and preserve function after spinal cord injury. *J. Neurosci.* **24,** 2143–55 (2004).

87. Nimmerjahn, A., Kirchhoff, F., Kerr, J. N. D. & Helmchen, F. Sulforhodamine 101 as a specific marker of astroglia in the neocortex in vivo. *Nat. Methods* **1,** 31–7 (2004).

88. Pawley, J. Fundamental limits in confocal microscopy. *Handb. Biol. confocal Microsc.* **Chapter 2,** 20–42 (2006).

89. Hell, S. Primer: fluorescence imaging under the diffraction limit. *Nat. Methods* **6,** 2008–2009 (2009).

90. Lippincott-Schwartz, J. & Manley, S. Putting super-resolution fluorescence microscopy to work. *Nat. Methods* **6,** 21–3 (2009).

91. Inoué, S. Foundations of Confocal Scanned Imaging in Light Microscopy. *Handb. Biol. confocal Microsc.* 1–19 (2006).

92. Feng, G., Mellor, R. & Bernstein, M. Imaging neuronal subsets in transgenic mice expressing multiple spectral variants of GFP. *Neuron* **28,** 41–51 (2000).

93. Mallon, B. S., Shick, H. E., Kidd, G. J. & Macklin, W. B. Proteolipid promoter activity distinguishes two populations of NG2-positive cells throughout neonatal cortical development. *J. Neurosci.* **22,** 876–85 (2002).

94. Jung, S. *et al.* Analysis of fractalkine receptor CX(3)CR1 function by targeted deletion and green fluorescent protein reporter gene insertion. *Mol. Cell. Biol.* **20,** 4106–14 (2000).

95. JAX Mice Database - 007967 B6.Cg-Tg(Thy1-CFP/COX8A)S2Lich/J. at <http://jaxmice.jax.org/strain/007967.html>

96. JAX Mice Database - 003257 FVB/N-Tg(GFAPGFP)14Mes/J. at <http://jaxmice.jax.org/strain/003257.html>

97. Ridsdale, A., Micu, I. & Stys, P. K. Conversion of the Nikon C1 confocal laser-scanning head for multiphoton excitation on an upright microscope. *Appl. Opt.* **43,** 1669–75 (2004).

98. Pawley, J. *Handbook of biological confocal microscopy*. (2010).

99. Waxman, S. & Bennett, M. Relative conduction velocities of small myelinated and non-myelinated fibres in the central nervous system. *Nature* (1972).

100. Hildebrand, C. & Hahn, R. Relation between myelin sheath thickness and axon size in spinal cord white matter of some vertebrate species. *J. Neurol. Sci.* **38,** 421–434 (1978).

101. Aggarwal, S., Yurlova, L. & Simons, M. Central nervous system myelin: structure, synthesis and assembly. *Trends Cell Biol.* **21,** 585–93 (2011).

102. Agrawal, S. K. & Fehlings, M. G. The effect of the sodium channel blocker QX-314 on recovery after acute spinal cord injury. *J. Neurotrauma* **14,** 81–88 (1997).

103. Feurer, D. J. & Weller, R. O. Barrier functions of the leptomeninges: a study of normal meninges and meningiomas in tissue culture. *Neuropathol. Appl. Neurobiol.* **17,** 391–405 (1991).

104. Reina, M. A. *et al.* Ultrastructural Findings in Human Spinal Pia Mater in Relation to Subarachnoid Anesthesia. *Anesth. Analg.* 1479–1485 (2004).

105. Shroff, S. *et al.* Paranodal permeability in 'myelin mutants'. *Glia* **59,** 1447–57 (2011).

106. Bonnici, B. & Kapfhammer, J. P. Spontaneous regeneration of intrinsic spinal cord axons in a novel spinal cord slice culture model. *Eur. J. Neurosci.* **27,** 2483–2492 (2008).

107. Krassioukov, A. V *et al.* An in vitro model of neurotrauma in organotypic spinal cord cultures from adult mice. *Brain Res. Brain Res. Protoc.* **10,** 60–8 (2002).

108. Rothstein, J. D., Jin, L. I. N., Dykes-hoberg, M. & Kuncl, R. W. Chronic inhibition of glutamate uptake produces a model of slow neurotoxicity. **90,** 6591–6595 (1993).

109. Steffens, H., Nadrigny, F. & Kirchhoff, F. In vivo two-photon imaging of neurons and glia in the mouse spinal cord. *Cold Spring Harb. Protoc.* **2012,** (2012).

110. Fenrich, K. K. *et al.* Long-term in vivo imaging of normal and pathological mouse spinal cord with subcellular resolution using implanted glass windows. *J. Physiol.* **590,** 3665–75 (2012).

111. Farrar, M. J. *et al.* Chronic in vivo imaging in the mouse spinal cord using an implanted chamber. *Nat. Methods* **9,** 297–302 (2012).

112. VAN HARREVELD, A. & HAWES, R. C. Asphyxial depolarisation in the spinal cord. *Am. J. Physiol.* **147,** 669–84 (1946).

113. News-letter, T. S. Spinal Cord Kept Alive. **55,** 276–277 (1949).

114. Eccles, R. M., Loyning, Y. & Oshima, T. Effects of hypoxia on the monosynaptic reflex pathway in the cat spinal cord. *J. Neurophysiol.* **29,** 315–31 (1966).

115. Stys, P. K., Ransom, B. R. & Waxman, S. G. compound action potential of nerve recorded by suction electrode: a theoretical and experimental analysis. *Brain Res.* **546,** 18–32 (1991).

116. Stys, P. K., Ransom, B. R., Waxman, S. G. & Davis, P. K. Role of extracellular calcium in anoxic injury of mammalian central white matter. *Proc. Natl. Acad. Sci. U. S. A.* **87,** 4212–6 (1990).

117. Ouardouz, M. *et al.* Depolarization-induced Ca2+ release in ischemic spinal cord white matter involves L-type Ca2+ channel activation of ryanodine receptors. *Neuron* **40,** 53–63 (2003).

118. Ravikumar, M., Jain, S., Miller, R. H., Capadona, J. R. & Selkirk, S. M. An organotypic spinal cord slice culture model to quantify neurodegeneration. *J. Neurosci. Methods* **211,** 280–288 (2012).

119. Nave, K.-A. Myelination and support of axonal integrity by glia. *Nature* **468,** 244–52 (2010).

120. Griffiths, I., Klugmann, M. & Anderson, T. Axonal swellings and degeneration in mice lacking the major proteolipid of myelin. *Science (80-.).* **280,** 1610–3 (1998).

121. Edgar, J. M. *et al.* Oligodendroglial modulation of fast axonal transport in a mouse model of hereditary spastic paraplegia. *J. Cell Biol.* **166,** 121–31 (2004).

122. Greenstein, B. & Ph, D. *Color Atlas of Neuroscience*.

123. Prickett, C. O. & Stevens, C. The polarized light method for the study of myelin degeneration as compared with the Marchi and Sudan III methods. *Am. J. Pathol.* **15,** 241–250.7 (1939).

124. Urabe, N., Naito, I. & Saito, K. Basement membrane type IV collagen molecules in the choroid plexus, pia mater and capillaries in the mouse brain. *Arch. Histol.* … (2002).

125. Engelhardt, B. & Ransohoff, R. M. Capture, crawl, cross: The T cell code to breach the blood-brain barriers. *Trends Immunol.* **33,** 579–589 (2012).

126. Engelhardt, B. & Coisne, C. Fluids and barriers of the CNS establish immune privilege by confining immune surveillance to a two-walled castle moat surrounding the CNS castle. *Fluids Barriers CNS* **8,** 4 (2011).

127. Benes, F. M. Myelination of cortical-hippocampal relays during late adolescence. *Schizophr. Bull.* **15,** 585–93 (1989).

128. Norton, W. T. & Poduslo, S. E. Myelination in rat brain: changes in myelin composition during brain maturation. *J. Neurochem.* **21,** 749–57 (1973).

129. Srinivasan, R., Sailasuta, N. & Hurd, R. Evidence of elevated glutamate in multiple sclerosis using magnetic resonance spectroscopy at 3 T. *Brain* **128,** 1016–1025 (2005).

130. Werner, P., Pitt, D. & Raine, C. S. Multiple sclerosis: altered glutamate homeostasis in lesions correlates with oligodendrocyte and axonal damage. *Ann Neurol* **50,** 169–180 (2001).

131. Newcombe, J. *et al.* Glutamate receptor expression in multiple sclerosis lesions. *Brain Pathol.* **18,** 52–61 (2008).

132. Pitt, D., Werner, P. & Raine, C. S. Glutamate excitotoxicity in a model of multiple sclerosis. *Nat. Med.* **6,** 67–70 (2000).

133. McDonald, J. W. & Sadowsky, C. Spinal-cord injury. in *Lancet* **359,** 417–425 (2002).

134. Dobkin, B. H. & Havton, L. A. Basic advances and new avenues in therapy of spinal cord injury. *Annu Rev Med* **55,** 255–282 (2004).

135. Ackerley, S. *et al.* Glutamate slows axonal transport of neurofilaments in transfected neurons. *J. Cell Biol.* **150,** 165–76 (2000).

136. Stone, J. R. *et al.* Impaired axonal transport and altered axolemmal permeability occur in distinct populations of damaged axons following traumatic brain injury. *Exp Neurol* **190,** 59–69 (2004).

137. Court, F. & Coleman, M. Mitochondria as a central sensor for axonal degenerative stimuli. *Trends Neurosci.* **35,** 364–72 (2012).

138. Wang, J. T., Medress, Z. a & Barres, B. a. Axon degeneration: molecular mechanisms of a self-destruction pathway. *J. Cell Biol.* **196,** 7–18 (2012).

139. Lassmann, H. Hypoxia-like tissue injury as a component of multiple sclerosis lesions. *J. Neurol. Sci.* **206,** 187–191 (2003).

140. Groom, A. J., Smith, T. & Turski, L. Multiple sclerosis and glutamate. *Ann. N. Y. Acad. Sci.* **993,** 229–75; discussion 287–8 (2003).

141. Griffin, J. W., Price, D. L., Engel, W. K. & Drachman, D. B. The pathogenesis of reactive axonal swellings: role of axonal transport. *J Neuropathol Exp Neurol* **36,** 214–227 (1977).

142. Friede, R. & Martinez, A. Analysis of axon-sheath relations during early Wallerian degeneration. *Brain Res.* **19,** 199–212 (1970).

143. Martinez, A. J. & Friede, R. L. Accumulation of axoplasmic organelles in swollen nerve fibers. *Brain Res.* **19,** 183–98 (1970).

144. Vial, J. D. The early changes in the axoplasm during wallerian degeneration. *J Biophys Biochem Cytol* **4,** 551–555 (1958).

145. Lubińska, L. Early course of Wallerian degeneration in myelinated fibres of the rat phrenic nerve. *Brain Res.* **130,** 47–63 (1977).

146. Lubinska, L. Early course of Wallerian degeneration in myelinated fibres of the rat phrenic nerve. *Brain Res* **130,** 47–63 (1977).

147. Conforti, L. *et al.* A Ufd2 ¯D4Cole1e chimeric protein and overexpression of Rbp7 in the slow Wallerian degeneration (Wld S) mouse. *Proc. Natl. Acad. Sci.* **97,** 11377–11382 (2000).

148. Mi, W., Beirowski, B. & Gillingwater, T. The slow Wallerian degeneration gene, WldS, inhibits axonal spheroid pathology in gracile axonal dystrophy mice. *Brain* **128,** 405–16 (2005).

149. Coleman, M. & Perry, V. Axon pathology in neurological disease: a neglected therapeutic target. *Trends Neurosci.* **25,** 532–7 (2002).

150. Charcot, J. Histologie de la sclérose en plaques. *Gaz. Hosp.* **141,** 554–558 (1868).

151. Bielschowsky, M. Zur Histologie der multiplen sklerose. *Neurol Cent.* **22,** 770–777 (1903).

152. Kornek, B. & Lassmann, H. Axonal pathology in multiple sclerosis. A historical note. *Brain Pathol.* **9,** 651–6 (1999).

153. Lampert, P. Electron microscopic studies on ordinary and hyperacute experimental allergic encephalomyelitis. *Acta Neuropathol.* **9,** 99–126 (1967).

154. Lampert, P. A Comparative Electron Microscopic Study of Reactive, Degenerating, Regenerating, and Dystrophic Axons. *J. Neuropathol. Exp. Neurol.* (1967).

155. Dutta, R. & Trapp, B. D. Mechanisms of neuronal dysfunction and degeneration in multiple sclerosis. *Prog. Neurobiol.* **93,** 1–12 (2011).

156. Ganter, P., Prince, C. & Esiri, M. M. Spinal cord axonal loss in multiple sclerosis: a post-mortem study. *Neuropathol Appl Neurobiol* **25,** 459–467 (1999).

157. Bitsch, A., Schuchardt, J., Bunkowski, S., Kuhlmann, T. & Bruck, W. Acute axonal injury in multiple sclerosis. Correlation with demyelination and inflammation. *Brain* **123 (Pt 6,** 1174–1183 (2000).

158. Bjartmar, C., Kidd, G., Mork, S., Rudick, R. & Trapp, B. D. Neurological disability correlates with spinal cord axonal loss and reduced N-acetyl aspartate in chronic multiple sclerosis patients. *Ann Neurol* **48,** 893–901 (2000).

159. Lovas, G. *et al.* Axonal changes in chronic demyelinated cervical spinal cord plaques. *Brain* **123 (Pt 2,** 308–317 (2000).

160. Bruck, W. The pathology of multiple sclerosis is the result of focal inflammatory demyelination with axonal damage. *J Neurol* **252 Suppl ,** v3–9 (2005).

161. Evangelou, N. *et al.* Regional axonal loss in the corpus callosum correlates with cerebral white matter lesion volume and distribution in multiple sclerosis. *Brain* **123 (Pt 9,** 1845–1849 (2000).

162. Bjartmar, C., Kinkel, R. P., Kidd, G., Rudick, R. A. & Trapp, B. D. Axonal loss in normal-appearing white matter in a patient with acute MS. *Neurology* **57,** 1248–1252 (2001).

163. Jones, M. V *et al.* Behavioral and pathological outcomes in MOG 35-55 experimental autoimmune encephalomyelitis. *J Neuroimmunol* **199,** 83–93 (2008).

164. Mathey, E. K. *et al.* Neurofascin as a novel target for autoantibody-mediated axonal injury. *J Exp Med* **204,** 2363–2372 (2007).

165. Huizinga, R., Gerritsen, W., Heijmans, N. & Amor, S. Axonal loss and gray matter pathology as a direct result of autoimmunity to neurofilaments. *Neurobiol. Dis.* **32,** 461–70 (2008).

166. Huizinga, R., Linington, C. & Amor, S. Resistance is futile: antineuronal autoimmunity in multiple sclerosis. *Trends Immunol* **29,** 54–60 (2008).

167. Nave, K. & Trapp, B. D. Axon-glial signaling and the glial support of axon function. *Annu. Rev. Neurosci.* **31,** 535–61 (2008).

168. Schlaepfer, W. W. & Bunge, R. P. Effects of calcium ion concentration on the degeneration of amputated axons in tissue culture. *J Cell Biol* **59,** 456–470 (1973).

169. McCarran, W. J. & Goldberg, M. P. White matter axon vulnerability to AMPA/kainate receptor-mediated ischemic injury is developmentally regulated. *J. Neurosci.* **27,** 4220–9 (2007).

170. Ouardouz, M., Malek, S., Coderre, E. & Stys, P. K. Complex interplay between glutamate receptors and intracellular Ca2+ stores during ischaemia in rat spinal cord white matter. *J. Physiol.* **577,** 191–204 (2006).

171. Stys, P. K., Waxman, S. G. & Ransom, B. R. Na(+)-Ca2+ exchanger mediates Ca2+ influx during anoxia in mammalian central nervous system white matter. *Ann. Neurol.* **30,** 375–80 (1991).

172. SKOU, J. C. The influence of some cations on an adenosine triphosphatase from peripheral nerves. *Biochim. Biophys. Acta* **23,** 394–401 (1957).

173. Imaizumi, T., Kocsis, J. D. & Waxman, S. G. Anoxic injury in the rat spinal cord: pharmacological evidence for multiple steps in Ca(2+)-dependent injury of the dorsal columns. *J Neurotrauma* **14,** 299–311 (1997).

174. Li, S. & Stys, P. K. Na(+)-K(+)-ATPase inhibition and depolarization induce glutamate release via reverse Na(+)-dependent transport in spinal cord white matter. *Neuroscience* **107,** 675–683 (2001).

175. Matute, C., Domercq, M. & Sánchez-Gómez, M.-V. Glutamate-mediated glial injury: mechanisms and clinical importance. *Glia* **53,** 212–24 (2006).

176. Vercellino, M. *et al.* Altered glutamate reuptake in relapsing-remitting and secondary progressive multiple sclerosis cortex: correlation with microglia infiltration, demyelination, and neuronal and synaptic damage. *J Neuropathol Exp Neurol* **66,** 732–739 (2007).

177. Underhill, S. & Goldberg, M. Hypoxic injury of isolated axons is independent of ionotropic glutamate receptors. *Neurobiol. Dis.* **25,** 284–290 (2007).

178. Stys, P. K. & Li, S. Glutamate-Induced White Matter Injury: Excitotoxicity without Synapses. *Neurosci.* **6,** 230–233 (2000).

179. Choi, D. W. Glutamate Neurotoxicity. 623–634 (1988).

180. Heim, N. *et al.* Improved calcium imaging in transgenic mice expressing a troponin C – based biosensor. *Nat. Methods* **4,** 2006–2008 (2007).

181. Mank, M. *et al.* A FRET-based calcium biosensor with fast signal kinetics and high fluorescence change. *Biophys. J.* **90,** 1790–6 (2006).

182. Selvatici, R. *et al.* Sodium azide induced neuronal damage in vitro: evidence for non-apoptotic cell death. *Neurochem. Res.* **34,** 909–16 (2009).

183. Stirling, D. P., Cummins, K., Wayne Chen, S. R. & Stys, P. Axoplasmic reticulum Ca(2+) release causes secondary degeneration of spinal axons. *Ann. Neurol.* **75,** 220–9 (2014).

184. Fill, M. & Copello, J. a. Ryanodine receptor calcium release channels. *Physiol. Rev.* **82,** 893–922 (2002).

185. Lichtman, J. W. & Conchello, J. Fluorescence microscopy. *Nat. Methods* **2,** (2003).

186. Houdebine, L. M. The methods to generate transgenic animals and to control transgene expression. in *Journal of Biotechnology* **98,** 145–160 (2002).

187. Heim, N. & Griesbeck, O. Genetically encoded indicators of cellular calcium dynamics based on troponin C and green fluorescent protein. *J. Biol. Chem.* **279,** 14280–6 (2004).

188. Chen, Y. & Mauldin, J. Characterization of spectral FRET imaging microscopy for monitoring nuclear protein interactions. *J.* … **228,** 139–152 (2007).

189. Beirowski, B., Nógrádi, A., Babetto, E., Garcia-Alias, G. & Coleman, M. P. Mechanisms of axonal spheroid formation in central nervous system Wallerian degeneration. *J. Neuropathol. Exp. Neurol.* **69,** 455–72 (2010).

190. Fern, R., Davis, P., Waxman, S. G. & Ransom, B. R. Axon conduction and survival in CNS white matter during energy deprivation: a developmental study. *J Neurophysiol* **79,** 95–105 (1998).

191. III, A. A. CNS energy metabolism as related to function. *Brain Res. Rev.* **34,** 42–68 (2000).

192. Malek, S. A., Adorante, J. S. & Stys, P. K. Differential effects of Na-K-ATPase pump inhibition, chemical anoxia, and glycolytic blockade on membrane potential of rat optic nerve. *Brain Res* **1037,** 171–179 (2005).

193. Jabaudon, D., Scanziani, M., Gähwiler, B. H. & Gerber, U. Acute decrease in net glutamate uptake during energy deprivation. *Proc. Natl. Acad. Sci. U. S. A.* **97,** 5610–5615 (2000).

194. Barger, S. W., Goodwin, M. E., Porter, M. M. & Beggs, M. L. Glutamate release from activated microglia requires the oxidative burst and lipid peroxidation. *J. Neurochem.* **101,** 1205–13 (2007).

195. David, S. & Kroner, A. Repertoire of microglial and macrophage responses after spinal cord injury. *Nat. Rev. Neurosci.* **12,** 388–99 (2011).

196. Brown, G. C. & Bal-Price, A. Inflammatory neurodegeneration mediated by nitric oxide, glutamate, and mitochondria. *Mol. Neurobiol.* **27,** 325–55 (2003).

197. Bezzi, P. *et al.* CXCR4-activated astrocyte glutamate release via TNFalpha: amplification by microglia triggers neurotoxicity. *Nat. Neurosci.* **4,** 702–10 (2001).

198. Matute, C. *et al.* The link between excitotoxic oligodendroglial death and demyelinating diseases. *Trends Neurosci* **24,** 224–230 (2001).

199. Takahashi, J. L., Giuliani, F., Power, C., Imai, Y. & Yong, V. W. Interleukin-1beta promotes oligodendrocyte death through glutamate excitotoxicity. *Ann. Neurol.* **53,** 588–95 (2003).

200. Bennett, M. C., Mlady, G. W., Kwon, Y. H. & Rose, G. M. Chronic in vivo sodium azide infusion induces selective and stable inhibition of cytochrome c oxidase. *J Neurochem* **66,** 2606–2611 (1996).

201. Schlaepfer, W. Effects of energy deprivation on Wallerian degeneration in isolated segments of rat peripheral nerve. *Brain Res.* **78,** 71–81 (1974).

202. Mahad, D. J. *et al.* Mitochondrial changes within axons in multiple sclerosis. *Brain* **132,** 1161–74 (2009).

203. Xu, G.-Y., Hughes, M. G., Ye, Z., Hulsebosch, C. E. & McAdoo, D. J. Concentrations of glutamate released following spinal cord injury kill oligodendrocytes in the spinal cord. *Exp. Neurol.* **187,** 329–36 (2004).

204. Arranz, A. M. *et al.* Functional glutamate transport in rodent optic nerve axons and glia. *Glia* **56,** 1353–1367 (2008).

205. Erber, U. G. Inhibition of uptake unmasks rapid extracellular turnover of glutamate of nonvesicular origin. **96,** 8733–8738 (1999).

206. Gueler, N., Kukley, M. & Dietrich, D. TBOA-sensitive uptake limits glutamate penetration into brain slices to a few micrometers. *Neurosci. Lett.* **419,** 269–72 (2007).

207. Hawkins, R. a. The blood-brain barrier and glutamate. *Am. J. Clin. Nutr.* **90,** 867S–874S (2009).

208. Aboul-Enein, F. & Lassmann, H. Mitochondrial damage and histotoxic hypoxia: a pathway of tissue injury in inflammatory brain disease? *Acta Neuropathol.* **109,** 49–55 (2005).

209. Rothstein, J. D. *et al.* Knockout of glutamate transporters reveals a major role for astroglial transport in excitotoxicity and clearance of glutamate. *Neuron* **16,** 675–86 (1996).

210. Lehre, K. & Danbolt, N. The number of glutamate transporter subtype molecules at glutamatergic synapses: chemical and stereological quantification in young adult rat brain. *J. Neurosci.* (1998).

211. Danbolt, N. Glutamate uptake. *Prog. Neurobiol.* **65,** 1–105 (2001).

212. Matute, C., Alberdi, E., Ibarretxe, G. & Sánchez-Gómez, M. V. Excitotoxicity in glial cells. *Eur. J. Pharmacol.* **447,** 239–46 (2002).

213. Federoff, S. & Vernadakis, A. Astrocytes: Development, Morphology and Regional Specialization of Astrocytes. (1986).

214. O'Kane, R. L., Martínez-López, I., DeJoseph, M. R., Viña, J. R. & Hawkins, R. A. Na(+)-dependent glutamate transporters (EAAT1, EAAT2, and EAAT3) of the blood-brain barrier. A mechanism for glutamate removal. *J. Biol. Chem.* **274,** 31891–5 (1999).

215. Sievers, J., Pehlemann, F. W., Gude, S. & Berry, M. Meningeal cells organize the superficial glia limitans of the cerebellum and produce components of both the interstitial matrix and the basement membrane. *J. Neurocytol.* **23,** 135–149 (1994).

216. Ellisman, M. & Porter, K. Microtrabecular structure of the axoplasmic matrix: visualization of cross-linking structures and their distribution. *J. Cell Biol.* **87,** (1980).

217. Droz, B., Rambourg, A. & Koenig, H. L. The smooth endoplasmic reticulum: structure and role in the renewal of axonal membrane and synaptic vesicles by fast axonal transport. *Brain Research* **93,** 1–13 (1975).

218. Xu, C., Bailly-Maitre, B. & Reed, J. Endoplasmic reticulum stress: cell life and death decisions. *J. Clin. Invest.* **115,** 2656–2664 (2005).

219. Honig, M. a & Rapuano, C. J. cell injury, cell death, and adaptations. 1–30

220. Brac, T. Intracellular polycationic molecules cause reversible swelling of the rough endoplasmic reticulum. *Tissue Cell* **15,** 365–373 (1983).

221. Ren, Y., Ridsdale, A., Coderre, E. & Stys, P. Calcium imaging in live rat optic nerve myelinated axons in vitro using confocal laser microscopy. *J. Neurosci. Methods* **102,** 165–176 (2000).

222. Berridge, M. J. Calcium hypothesis of Alzheimer's disease. *Pflugers Archiv European Journal of Physiology* **459,** 441–449 (2010).

223. Beirowski, B. *et al.* Quantitative and qualitative analysis of Wallerian degeneration using restricted axonal labelling in YFP-H mice. *J Neurosci Methods* **134,** 23–35 (2004).

224. Bareyre, F. M., Kerschensteiner, M., Misgeld, T. & Sanes, J. R. Transgenic labeling of the corticospinal tract for monitoring axonal responses to spinal cord injury. *Nat. Med.* **11,** 1355–60 (2005).

225. Verkhratsky, A. Physiology and pathophysiology of the calcium store in the endoplasmic reticulum of neurons. *Physiol. Rev.* **85,** 201–79 (2005).

226. Henkart, M., Reese, T. & Brinley, F. Endoplasmic reticulum sequesters calcium in the squid giant axon. *Science (80-.).* (1978).

227. Berridge, M. J. The endoplasmic reticulum : a multifunctional signaling organelle. **32,** 235–249 (2002).

228. Sokka, A.-L. *et al.* Endoplasmic reticulum stress inhibition protects against excitotoxic neuronal injury in the rat brain. *J. Neurosci.* **27,** 901–908 (2007).

229. Ribeiro, C. M., McKay, R. R., Hosoki, E., Bird, G. S. & Putney, J. W. Effects of elevated cytoplasmic calcium and protein kinase C on endoplasmic reticulum structure and function in HEK293 cells. *Cell Calcium* **27,** 175–185 (2000).

230. Trigo, D. & Smith, K. J. Axonal morphological changes following impulse activity in mouse peripheral nerve in vivo: the return pathway for sodium ions. *J. Physiol.* **4,** n/a–n/a (2015).

231. Pampliega, O. *et al.* Increased expression of cystine/glutamate antiporter in multiple sclerosis. *J. Neuroinflammation* **8,** 63 (2011).

232. Bolton, C. & Paul, C. Glutamate receptors in neuroinflammatory demyelinating disease. *Mediators Inflamm.* **2006,** 93684 (2006).

233. Vallejo-Illarramendi, A., Domercq, M., Pérez-Cerdá, F., Ravid, R. & Matute, C. Increased expression and function of glutamate transporters in multiple sclerosis. *Neurobiol. Dis.* **21,** 154–164 (2006).

234. Quarles, R., Macklin, W. & Morell, P. in *Basic neurochemistry: molecular, cellular and medical aspects* 51–72 (2006).

235. Norton, W. & Cammer, W. *Chemical pathology of diseases involving myelin*. *Myelin* (1984).

236. Chrast, R., Saher, G., Nave, K.-A. & Verheijen, M. H. G. Lipid metabolism in myelinating glial cells: lessons from human inherited disorders and mouse models. *J. Lipid Res.* **52,** 419–34 (2011).

237. Brien, J. S. O. Stability of the Myelin Membrane. 1099–1107

238. Cuzner, M. L. & Davison, A. N. The lipid composition of rat brain myelin and subcellular fractions during development. *Biochem. J.* **106,** 29–34 (1968).

239. Matthieu, J., Widmer, S. & Herschkowitz, N. Biochemical changes in mouse brain composition during myelination. *Brain Res.* **55,** 391–402 (1973).

240. Malone, M. & Szoke, M. Neurochemical studies in aging brain. I. Structural changes in myelin lipids. *J. Gerontol.* **37,** 262–267 (1982).

241. Johnson, a C., McNabb, a R. & Rossiter, R. J. Concentration of lipids in the brain of infants and adults. *Biochem. J.* **44,** 494–8 (1949).

242. Fadok, V. a, Bratton, D. L., Frasch, S. C., Warner, M. L. & Henson, P. M. The role of phosphatidylserine in recognition of apoptotic cells by phagocytes. *Cell Death Differ.* **5,** 551–562 (1998).

243. Cumings, J. & Goodwin, H. Sphingolipids and phospholipids of myelin in multiple sclerosis. *Lancet* (1968). at <http://www.sciencedirect.com/science/article/pii/S0140673668925105>

244. Wender, M., Filipek-Wender, H. & Stanisławska, J. Cholesteryl esters of the brain in demyelinating diseases. *Clin. Chim. Acta* **54,** 269–275 (1974).

245. Moore, G. R. W. *et al.* Dirty-appearing white matter in multiple sclerosis: preliminary observations of myelin phospholipid and axonal loss. *J. Neurol.* **255,** 1802–11, discussion 1812 (2008).

246. Laule, C. *et al.* Diffusely abnormal white matter in multiple sclerosis: further histologic studies provide evidence for a primary lipid abnormality with neurodegeneration. *J. Neuropathol. Exp. Neurol.* **72,** 42–52 (2013).

247. Yu, R. K., Ueno, K., Glaser, G. H. & Tourtellotte, W. W. Lipid and protein alterations of spinal cord and cord myelin of multiple sclerosis. *J. Neurochem.* **39,** 464–77 (1982).

248. Wilson, R. & Tocher, D. Lipid and fatty acid composition is altered in plaque tissue from multiple sclerosis brain compared with normal brain white matter. *Lipids* **26,** 9–15 (1991).

249. Alling, C., Vanier, M. R. S. E. & Svennerholm, L. Lipid alterations in apparently normal white matter in multiple sclerosis. **35,** 325–336 (1971).

250. Gerstl, B., Kahnke, M. & Smith, J. Brain lipids in multiple sclerosis and other diseases. *Brain* 310–319 (1961). at <http://brain.oxfordjournals.org/content/84/2/310.short>

251. Kanter, J. L. *et al.* Lipid microarrays identify key mediators of autoimmune brain inflammation. *Nat. Med.* **12,** 138–43 (2006).

252. Maier, O., Oberle, V. & Hoekstra, D. Fluorescent lipid probes: some properties and applications (a review). *Chem. Phys. Lipids* **116,** 3–18 (2002).

253. Hinman, J. D. & Abraham, C. R. What's behind the decline? The role of white matter in brain aging. *Neurochem. Res.* **32,** 2023–31 (2007).

254. Sastry, P. S. Lipids of nervous tissue: composition and metabolism. *Prog. Lipid Res.* **24,** 69–176 (1985).

255. Wheeler, D., Bandaru, V. V. R., Calabresi, P. a, Nath, A. & Haughey, N. J. A defect of sphingolipid metabolism modifies the properties of normal appearing white matter in multiple sclerosis. *Brain* **131,** 3092–102 (2008).

256. Wang, H., Fu, Y., Zickmund, P., Shi, R. & Cheng, J.-X. Coherent anti-stokes Raman scattering imaging of axonal myelin in live spinal tissues. *Biophys. J.* **89,** 581–91 (2005).

257. Panchuk-Voloshina, N. *et al.* Alexa dyes, a series of new fluorescent dyes that yield exceptionally bright, photostable conjugates. *J. Histochem. Cytochem.* **47,** 1179–88 (1999).

258. Sackett, D. L. & Wolff, J. Nile red as a polarity-sensitive fluorescent probe of hydrophobic protein surfaces. *Anal. Biochem.* **167,** 228–34 (1987).

259. Kucherak, O. a *et al.* Switchable nile red-based probe for cholesterol and lipid order at the outer leaflet of biomembranes. *J. Am. Chem. Soc.* **132,** 4907–16 (2010).

260. Mukherjee, S., Raghuraman, H. & Chattopadhyay, A. Membrane localization and dynamics of Nile Red: effect of cholesterol. *Biochim. Biophys. Acta* **1768,** 59–66 (2007).

261. Fowler, S. D. & Greenspan, P. Application of Nile red, a fluorescent hydrophobic probe, for the detection of neutral lipid deposits in tissue sections: comparison with oil red O. *J. Histochem. Cytochem.* **33,** 833–6 (1985).

262. Greenspan, P. & Fowler, S. Spectrofluorometric studies of the lipid probe, nile red. *J. Lipid Res.* **26,** 781–789 (1985).

263. Klinkner, A. M. *et al.* A novel technique for mapping the lipid composition of atherosclerotic fatty streaks by en face fluorescence microscopy. *J. Histochem. Cytochem.* **45,** 743–53 (1997).

264. Bonilla, E. & Prelle, a. Application of nile blue and nile red, two fluorescent probes, for detection of lipid droplets in human skeletal muscle. *J. Histochem. Cytochem.* **35,** 619–621 (1987).

265. Greenspan, P., Mayer, E. P. & Fowler, S. D. Nile red: a selective fluorescent stain for intracellular lipid droplets. *J. Cell Biol.* **100,** 965–73 (1985).

266. Brown, W., Sullivan, T. & Greenspan, P. Nile red staining of lysosomal phospholipid inclusions. *Histochemistry* 349–354 (1992).

267. Romek, M., Gajda, B. & Krzysztofowicz, E. New technique to quantify the lipid composition of lipid droplets in porcine oocytes and pre-implantation embryos using Nile Red fluorescent probe. *Theriogenology* **75,** 42–54 (2011).

268. Miklossy, J. & Van der Loos, H. The long-distance effects of brain lesions: visualization of myelinated pathways in the human brain using polarizing and fluorescence microscopy. *J. Neuropathol. Exp. Neurol.* **50,** 1–15 (1991).

269. Stirling, D. P. *et al.* Toll-like receptor 2-mediated alternative activation of microglia is protective after spinal cord injury. *Brain* **137,** 707–23 (2014).

270. Arnaud, E. SH3TC2/KIAA1985 protein is required for proper myelination and the integrity of the node of Ranvier in the peripheral nervous system. *Proc.* … **107,** 15305–15305 (2009).

271. Valeur, B. & Berberan-Santos, M. *Molecular fluorescence: principles and applications*. **8,** (2012).

272. Lakowicz, J. R. *Principles of Fluorescence Spectroscopy*. *Medicine* (2010).

273. Parasassi, T. *et al.* Quantitation of lipid phases in phospholipid vesicles by the generalized polarization of Laurdan fluorescence. **60,** 179–189 (1991).

274. Yu, W., So, P. T., French, T. & Gratton, E. Fluorescence generalized polarization of cell membranes: a two-photon scanning microscopy approach. *Biophys. J.* **70,** 626–36 (1996).

275. Heidcamp, W. H. Cell Biology Lab Manual: Membranes. *Biology Department, Gustavus Adolphus College* (1995). at <http://homepages.gac.edu/~cellab/chpts/chpt6/ex6-10.html>

276. Roysam, B., Lin, G. & Abdul-Karim, M. Automated three-dimensional image analysis methods for confocal microscopy. *Handb. Biol. confocal Microsc.* 316–337 (2006).

277. Hayat, M. *Fixation for electron microscopy*. (2012).

278. Kiernan, J. Histological and histochemical methods: theory and practice. *Shock* (1999).

279. Folch, J., Lees, M. & Sloane-Stanley, G. A simple method for the isolation and purification of total lipids from animal tissues. *J Biol chem* **226,** 497–509 (1957).

280. Vejux, A. *et al.* 7-Ketocholesterol favors lipid accumulation and colocalizes with Nile Red positive cytoplasmic structures formed during 7-ketocholesterol-induced apoptosis: Analysis by flow cytometry, FRET biphoton spectral imaging microscopy, and subcellular fractionati. *Cytom. Part A* **64,** 87–100 (2005).

281. Luby-Phelps, K. Cytoarchitecture and physical properties of cytoplasm: volume, viscosity, diffusion, intracellular surface area. *Int. Rev. Cytol.* **192,** 189–221 (2000).

282. Klugmann, M. *et al.* Assembly of CNS Myelin in the Absence of Proteolipid Protein. *Neuron* **18,** 59–70 (1997).

283. Rosenbluth, J., Nave, K.-A., Mierzwa, A. & Schiff, R. Subtle myelin defects in PLP-null mice. *Glia* **54,** 172–82 (2006).

284. Werner, H. B. *et al.* A critical role for the cholesterol-associated proteolipids PLP and M6B in myelination of the central nervous system. *Glia* **61,** 567–586 (2013).

285. Yin, X. *et al.* Evolution of a neuroprotective function of central nervous system myelin. *J. Cell Biol.* **172,** 469–78 (2006).

286. Simons, M. & Trotter, J. Wrapping it up: the cell biology of myelination. *Curr Opin Neurobiol* **17,** 533–540 (2007).

287. Eng, L. F. & Noble, E. P. The maturation of rat brain myelin. *Lipids* **3,** 157–162 (1968).

288. O'Brien, J. & Sampson, E. Lipid composition of the normal human brain : gray matter, white matter, and myelin. *J. Lipid Res.* **6,** (1965).

289. Saher, G., Quintes, S. & Nave, K. Cholesterol: a novel regulatory role in myelin formation. *Neuroscientist* **17,** 79–93 (2011).

290. Saher, G. *et al.* High cholesterol level is essential for myelin membrane growth. *Nat. Neurosci.* **8,** 468–75 (2005).

291. Lajtha, B. A., Toth, J., Fujimotot, K. & Agrawalt, H. C. Turnover of Myelin Proteins in Mouse Brain in vivo. 323–329 (1976).

292. Ando, S., Tanaka, Y., Toyoda, Y. & Kon, K. Turnover of myelin lipids in aging brain. *Neurochem. Res.* **28,** 5–13 (2003).

293. Dixit, R. & Cyr, R. Cell damage and reactive oxygen species production induced by fluorescence microscopy: effect on mitosis and guidelines for non-invasive fluorescence microscopy. *Plant J.* **36,** 280–290 (2003).

294. Song, L., Varma, C. A., Verhoeven, J. W. & Tanke, H. J. Influence of the triplet excited state on the photobleaching kinetics of fluorescein in microscopy. *Biophys. J.* **70,** 2959–2968 (1996).

295. Bongarzone, E. R., Pasquini, J. M. & Soto, E. F. Oxidative damage to proteins and lipids of CNS myelin produced by in vitro generated reactive oxygen species. *J. Neurosci. Res.* **41,** 213–21 (1995).

296. Halliwell, B. & Chirico, S. Lipid peroxidation: its mechanism, measurement, and significance. *Am. J. Clin. Nutr.* (1993). at <http://ajcn.nutrition.org/content/57/5/715S.short>

297. Wong-Ekkabut, J. *et al.* Effect of lipid peroxidation on the properties of lipid bilayers: a molecular dynamics study. *Biophys. J.* **93,** 4225–4236 (2007).

298. Wratten, M. L. *et al.* Structural and dynamic effects of oxidatively modified phospholipids in unsaturated lipid membranes. *Biochemistry* **31,** 10901–10907 (1992).

299. Hall, S. M. The effect of injections of lysophosphatidyl choline into white matter of the adult mouse spinal cord. *J. Cell Sci.* **10,** 535–46 (1972).

300. Blakemore, W. F., Eames, R. A., Smith, K. J. & McDonald, W. I. Remyelination in the spinal cord of the cat following intraspinal injections of lysolecithin. *J. Neurol. Sci.* **33,** 31–43 (1977).

301. Ousman, S. & David, S. Lysophosphatidylcholine induces rapid recruitment and activation of macrophages in the adult mouse spinal cord. *Glia* **104,** 92–104 (2000).

302. Lau, L. W. *et al.* Chondroitin sulfate proteoglycans in demyelinated lesions impair remyelination. *Ann. Neurol.* **72,** 419–32 (2012).

303. McKeon, R., Jurynec, M. & Buck, C. The chondroitin sulfate proteoglycans neurocan and phosphacan are expressed by reactive astrocytes in the chronic CNS glial scar. *J. Neurosci.* **19,** 10778–10788 (1999).

304. Kreutzberg, G. Microglia: a sensor for pathological events in the CNS. *Trends Neurosci.* **2236,** 471–474 (1996).

305. Powers, B. E. *et al.* Axonal thinning and extensive remyelination without chronic demyelination in spinal injured rats. *J. Neurosci.* **32,** 5120–5 (2012).

306. Cumings, J. Lipid chemistry of the brain in demyelinating diseases. *Brain* (1955).

307. Ramsey, R. & Davison, A. Steryl esters and their relationship to normal and diseased human central nervous system. *J. Lipid Res.* **15,** 249–255 (1974).

308. Mastronardi, F. G. & Moscarello, M. a. Molecules affecting myelin stability: a novel hypothesis regarding the pathogenesis of multiple sclerosis. *J. Neurosci. Res.* **80,** 301–8 (2005).

309. Navarro, X. & Segura, R. Plasma lipids and their fatty acid composition in multiple sclerosis. *Acta Neurol. Scand.* **78,** 152–7 (1988).

310. Fewster, M. E., Hirono, H. & Mead, J. F. Lipid composition of myelin in multiple sclerosis. *J. Neurol.* **213,** 119–31 (1976).

311. Laule, C. *et al.* Pathological basis of diffusely abnormal white matter: insights from magnetic resonance imaging and histology. *Mult. Scler.* **17,** 144–50 (2011).

312. Gopalakrishnan, G. *et al.* Lipidome and proteome map of myelin membranes. *J. Neurosci. Res.* **91,** 321–34 (2013).

313. Whittall, K. P. *et al.* Normal-appearing white matter in multiple sclerosis has heterogeneous, diffusely prolonged T(2). *Magn. Reson. Med.* **47,** 403–8 (2002).

314. Zukor, K. A., Kent, D. T. & Odelberg, S. J. Fluorescent whole-mount method for visualizing three-dimensional relationships in intact and regenerating adult newt spinal cords. *Dev. Dyn.* **239,** 3048–3057 (2010).

315. Siddiqui, S. & Rimm, D. L. Pre-analytic variables and phospho-specific antibodies: the Achilles heel of immunohistochemistry. *Breast Cancer Res.* **12,** 113 (2010).

316. Werring, D. J. *et al.* The pathogenesis of lesions and normal-appearing white matter changes in multiple sclerosis: a serial diffusion MRI study. *Brain* **123 (Pt 8,** 1667–1676 (2000).

317. Fancy, S. P. J., Chan, J. R., Baranzini, S. E., Franklin, R. J. M. & Rowitch, D. H. Myelin regeneration: a recapitulation of development? *Annu. Rev. Neurosci.* **34,** 21–43 (2011).

318. Velaz-Faircloth, M. *et al.* Characterization and distribution of the neuronal glutamate transporter EAAC1 in rat brain. *Am. J. Physiol.* **270,** C67–C75 (1996).

319. Lehre, K. P., Levy, L. M., Ottersen, O. P., Storm-Mathisen, J. & Danbolt, N. C. Differential expression of two glial glutamate transporters in the rat brain: quantitative and immunocytochemical observations. *J. Neurosci.* **15,** 1835–1853 (1995).

320. Todd, a. J. *et al.* The expression of vesicular glutamate transporters VGLUT1 and VGLUT2 in neurochemically defined axonal populations in the rat spinal cord with emphasis on the dorsal horn. *Eur. J. Neurosci.* **17,** 13–27 (2003).

321. Sibson, N. R. *et al.* Stoichiometric coupling of brain glucose metabolism and glutamatergic neuronal activity. *Proc. Natl. Acad. Sci. U. S. A.* **95,** 316–21 (1998).

322. Lerma, J., Herranz, a S., Herreras, O., Abraira, V. & Martín del Río, R. In vivo determination of extracellular concentration of amino acids in the rat hippocampus. A method based on brain dialysis and computerized analysis. *Brain Res.* **384,** 145–155 (1986).

323. Rose, E. M. *et al.* Glutamate transporter coupling to Na,K-ATPase. *J. Neurosci.* **29,** 8143–8155 (2009).

324. Sarchielli, P., Greco, L., Floridi, A., Floridi, A. & Gallai, V. Excitatory amino acids and multiple sclerosis: evidence from cerebrospinal fluid. *Arch. Neurol.* **60,** 1082–1088 (2003).

325. Piani, D., Spranger, M., Frei, K., Schaffner, a & Fontana, a. Macrophage-induced cytotoxicity of N-methyl-D-aspartate receptor positive neurons involves excitatory amino acids rather than reactive oxygen intermediates and cytokines. *Eur. J. Immunol.* **22,** 2429–2436 (1992).

326. Mahad, D., Ziabreva, I., Lassmann, H. & Turnbull, D. Mitochondrial defects in acute multiple sclerosis lesions. *Brain* **131,** 1722–1735 (2008).

327. Andrews, H. E., Nichols, P. P., Bates, D. & Turnbull, D. M. Mitochondrial dysfunction plays a key role in progressive axonal loss in Multiple Sclerosis. *Med Hypotheses* **64,** 669–677 (2005).

328. Hohlfeld, R. Ion channels boost axonal injury in multiple sclerosis. *Nat. Med.* **18,** 1743–5 (2012).

329. Young, E. A. *et al.* Imaging correlates of decreased axonal Na+/K+ ATPase in chronic multiple sclerosis lesions. *Ann. Neurol.* **63,** 428–35 (2008).

330. Tekkök, S. B., Faddis, B. T. & Goldberg, M. P. AMPA/kainate receptors mediate axonal morphological disruption in hypoxic white matter. *Neurosci. Lett.* **382,** 275–9 (2005).

331. Stys, P. K. & Jiang, Q. Calpain-dependent neurofilament breakdown in anoxic and ischemic rat central axons. *Neurosci. Lett.* **328,** 150–4 (2002).

332. Buki, A., Siman, R., Trojanowski, J. Q. & Povlishock, J. T. The role of calpain-mediated spectrin proteolysis in traumatically induced axonal injury. *J Neuropathol Exp Neurol* **58,** 365–375 (1999).

333. Thayer, S. a, Hirning, L. D. & Miller, R. J. The role of caffeine-sensitive calcium stores in the regulation of the intracellular free calcium concentration in rat sympathetic neurons in vitro. *Mol. Pharmacol.* **34,** 664–73 (1988).

334. Wray, S. & Burdyga, T. Sarcoplasmic reticulum function in smooth muscle. *Physiol. Rev.* **90,** 113–78 (2010).

335. Johnson, M. P. & Schoepp, D. D. Group II Metabotropic Glutamate Receptors (mGlu2 and mGlu3). 465–488

336. Saugstad, J. A. & Ingram, S. L. Group I Metabotropic Glutamate Receptors (mGlu1 and mGlu5). 387–463

337. Lassmann, H., Ammerer, H. P. & Kulnig, W. Ultrastructural sequence of myelin degradation. *Acta Neuropathol.* **44,** 91–102 (1978).

338. Rodriguez, M. & Scheithauer, B. Ultrastructure of multiple sclerosis. *Ultrastruct. Pathol.* **18,** 3–13

339. Cuzner, M. L. & Norton, W. T. Biochemistry of demyelination. *Brain Pathol.* **6,** 231–42 (1996).

340. Eng, L. F., Chao, F. C., Gerstl, B., Pratt, D. & Tavaststjerna, M. G. The maturation of human white matter myelin. Fractionation of the myelin membrane proteins. *Biochemistry* **7,** 4455–65 (1968).

341. Yablon, D. G. & Schilowitz, A. M. Solvatochromism of Nile Red in nonpolar solvents. *Appl. Spectrosc.* **58,** 843–7 (2004).

342. Jose, J. & Burgess, K. Benzophenoxazine-based fluorescent dyes for labeling biomolecules. *Tetrahedron* **62,** 11021–11037 (2006).

343. Reichardt, C. Solvatochromic dyes as solvent polarity indicators. *Chem. Rev.* **94,** 2319–2358 (1994).

344. Reichardt, C. & Welton, T. *Solvents and solvent effects in organic chemistry*. (2011).

345. Marini, A. & Munoz-Losa, A. What is solvatochromism? *J.* … 17128–17135 (2010). at <http://pubs.acs.org/doi/abs/10.1021/jp1097487>

346. Mohammad Reza, H., Mohammad Javad, C. & Maryam, Y. Solvatochromism effect of different solvents on UV-Vis spectra of flouresceine and its derivatives. *Iran. J. Chem. Chem. Eng.* **27,** 9–14 (2008).

347. Chakraborty, M. & Panda, A. K. Spectral behaviour of eosin y in different solvents and aqueous surfactant media. *Spectrochim. Acta - Part A Mol. Biomol. Spectrosc.* **81,** 458–465 (2011).

348. Lifetechnologies. Nile red in phospholipid. at <http://www.lifetechnologies.com/ca/en/home/life-science/cell-analysis/labeling-chemistry/fluorescence-spectraviewer.html>

349. Tajalli, H., Gilani, A., Zakerhamidi, M. S. & Tajalli, P. The photophysical properties of Nile red and Nile blue in ordered anisotropic media. *Dye. Pigment.* **78,** 15–24 (2008).

350. Fowler, S. D., Brown, W. J., Warfel, J. & Greenspan, P. Use of nile red for the rapid in situ quantitation of lipids on thin-layer chromatograms. *J. Lipid Res.* **28,** 1225–32 (1987).

351. Wootla, B., Eriguchi, M. & Rodriguez, M. Is multiple sclerosis an autoimmune disease? *Autoimmune Dis.* **2012,** 969657 (2012).

Appendix A

IGOR WaveMetrics code

```
#pragma rtGlobals=3             // Use modern global access method and strict wave access.
Menu "My Algorithms"
      "Multi-CPUs MSE & Peak", mThreadMSE_PEAK()
      "CleanUp_Tables",CleanupExperiment()
End
Function mThreadMSE_PEAK()
      variable xl
      variable xr
      prompt xl,"enter xl"
      Prompt xr,"enter xr"
      Doprompt "Enter values", xl,xr
      if (V_flag == 0)
            ThreadMSE_PEAK(xl, xr)
      endif
end

//////////////Mean square error calculation (batch with multicore support) ////////////////////////

Constant kNumDatasetsToProcess =20// Number of sample input waves to create and process
Constant kSampleWaveNumPoints = 1000   // Number of points in each sample input wave
Constant kPrintStartThreadMessage = 1
Constant kPrintGotThreadDFMessage = 1
Constant kSimulateVaryingComputationTime = 1
ThreadSafe Function ThreadWorker(wIn, wIn_control, waveIndex,xr,xl)
      variable xr,xl
      wave wIn
      WAVE wIn_control
      Variable waveIndex
      String NameWave = NameofWave(wIn)
      Wavestats/q/z wIn
      variable xPeak = V_maxloc
      Variable i,n=numpnts(wIn), massTimesX=0
      for(i=0; i<n; i+=1)
            massTimesX += wIn[i]*pnt2x(wIn,i)
      endfor
      Variable totalMass=sum(wIn)
      Variable centerOfMass= massTimesX/totalMass
      wave w1 = wIn_control
      duplicate/R=(xl, xr)/FREE w1, rw, bdw
      duplicate/R=(xl, xr)/FREE wIn, tdw
      rw = (bdw - tdw)^2 / numpnts(rw)
      Variable MeanSquare = sum(rw)
// This is used to simulate varying computation time
      if (kSimulateVaryingComputationTime > 0)
            Variable randomSecs = abs(enoise(kSimulateVaryingComputationTime))
            Sleep/S randomSecs
      endif
      NewDataFolder/S output
```

```
        Variable/G gMeanSquare = MeanSquare//centerOfMass
        Variable/G gxPeak = xPeak
       String/G gNameWave=NameWave
       Variable/G gPoint=numpnts(rw)
       Variable/G gxl=xl
        Variable/G gxr=xr
        // This tells the calling thread which wave was processed
        Variable/G gWaveIndex = waveIndex
        ThreadGroupPutDF 0, :        // Send data back to main thread
        return 0                     // Success
End
Function ThreadMSE_PEAK(xr,xl)
variable xr,xl
        if (IgorVersion() < 6.23)
                Abort "This demo requires Igor Pro 6.23 or later."
        endif
        Variable t0 = StopMSTimer(-2)          // Used to time the function
        DFREF originalDFR = GetDataFolderDFR()
        DFREF outputDFR = GetDataFolderDFR()
        Variable numDatasetsToProcess = kNumDatasetsToProcess
        Variable numDatasetsProcessed = 0
      Variable numPointsInSampleData = kSampleWaveNumPoints
        // Make output wave
        Make/O/D/N=(numDatasetsToProcess,2)  outputDFR:results = NaN
        wave results= outputDFR:results
        SetDimLabel 0,0,MeanSquareError,results
        SetDimLabel 0,1,SP_Peak,results
        make/O /T/N=(numDatasetsToProcess)  outputDFR:resultstext
        Wave/t resultstext = outputDFR:resultstext
        DoWindow /F OutputTable
        if (V_flag == 0)
                Edit /N=OutputTable /W=(466,49,906,652) results.ld
                Edit/N=OutputTableText resultstext
        endif
    DFREF inputDFR = :
        Variable numThreads = ThreadProcessorCount
        Variable threadGroupID = ThreadGroupCreate(numThreads)
        SetDataFolder inputDFR          // Needed for WaveRefIndexed
// Dispatch threads and collect output
Variable threadIndex
    Variable waveIndex  = 0
 //control
        wave wln_control =  WaveRefIndexed("", 0, 1)
        do
        // Start any free threads
                do
                        if (waveIndex >= numDatasetsToProcess)
                                break                           // No more input data to dispatch to a thread
                        endif
                        // Find a free thread
                        threadIndex = ThreadGroupWait(threadGroupID, -2)    // Requires Igor Pro 6.23
                        threadIndex -= 1        // Because ThreadGroupWait returns threadIndex+1
```

```
                if (threadIndex < 0)
                    break                   // No free threads
                endif
// Start thread
Wave wIn = WaveRefIndexed("", waveIndex, 1)
ThreadStart threadGroupID, threadIndex, ThreadWorker(wIn, wIn_control, waveIndex,xr,xl)
                if (kPrintStartThreadMessage)
                    Printf "Started thread %d\r", threadIndex       // For debugging only
                endif
                waveIndex += 1
            while(1)
            DFREF dfr = ThreadGroupGetDFR(threadGroupID, 0)
            if (DataFolderRefStatus(dfr) != 0)
                // Process results
                NVAR gMeanSquare = dfr:gMeanSquare
            NVAR gxPeak = dfr:gxPeak
                SVAR gNameWave= dfr:gNameWave
                NVAR gWaveIndex = dfr:gWaveIndex
              NVAR gPoint=dfr:gPoint
             NVAR gXr=dfr:gXr
             NVAR gXl=dfr:gXl
            results[gWaveIndex][0] = gMeanSquare
            results[gWaveIndex][1] = gxPeak
       resultstext[gWaveIndex][0] =gNameWave
                // Update the output table
                DoUpdate
                // For debugging only
                if (kPrintGotThreadDFMessage)
Printf "%d,%s,%g,%g,N=%g, Left=%g, Right=%g\r", gWaveIndex, gNameWave,gMeanSquare,
gxPeak,gPoint, gXl,Xr
                endif
//              print "N=",numpnts(bdw) // "WSFI=", WSFIvalue, rw
                numDatasetsProcessed += 1
                // This is a free data folder that would be killed automatically by Igor.
                // Nonetheless we explicitly kill it here and now.
                KillDataFolder dfr
            endif
      while(numDatasetsProcessed < numDatasetsToProcess)
      Variable dummy = ThreadGroupRelease(threadGroupID)
      Variable t1 = StopMSTimer(-2)
      Variable elapsedTime = (t1 - t0) / 1E6
      Printf "Finished ThreadMSE_PEAK in %.2f seconds.\r", elapsedTime
      SetDataFolder originalDFR
End
Function CleanupExperiment()    // We call this to prepare the experiment for shipping
      DoWindow /K OutputTable          // The table is recreated by the demo
      DoWindow/K OutputTabletext
      KillWaves/Z results                  // Output wave is recreated by the Demo
      KillDataFolder /Z root:SampleData        // Sample data is recreated by the demo
End


////////////////////////////Auto scale x-axis and normalization//////////////////////////////////
```

```
Menu "ScaX100_dup_Nor", dynamic
	TraceNameList ("",";",1), ScaX100_dup_Nor()
End
Function ScaX100_dup_nor()
	GetLastUserMenuInfo		// sets S_value, V_value, etc.
	ScaX100_dup_norValue(S_value)
end
Function ScaX100_dup_NorValue(tracename)
	String tracename
	WAVE w = TraceNameToWaveRef("", traceName)
	GetLastUserMenuInfo		// sets S_value, V_value, etc.
	wavestats/Q w
		Variable VyMax=V_max
		variable xpeak=V_maxloc
		String outputName= "n"+NameofWave($S_value)
		duplicate/O $S_value, $outputName
		SetScale/I x 0,100, $outputName
		wave output1 =$outputName
		output1= output1/VyMax
		removefromgraph $S_value
		AppendtoGraph output1
End

//////////////////////////////Copy and paste function of graph//////////////////////////
Menu "CopyPaste_Graph", dynamic
	TraceNameList ("",";",1), Copy_Paste_Graph()
End
Function Copy_Paste_Graph()
	GetLastUserMenuInfo		// sets S_value, V_value, etc.
	Copy_Paste_GraphValue(S_value)
end
Function Copy_Paste_GraphValue(tracename)
	String tracename

	WAVE w = TraceNameToWaveRef("", traceName)
	GetLastUserMenuInfo		// sets S_value, V_value, etc.
	//	WAVE/Z w= $S_value
	//wavestats/Q $S_value
	//	removefromgraph $S_value
	string nameGraph = ""
	Prompt nameGraph, "Type the name of graph to paste to"
	DoPrompt "Please enter the name of graph", nameGraph
		AppendtoGraph/w=$nameGraph, w
		//nr_fixedmyelin

End


//////////////////////////Central Mass //////////////////////

Function CMT(wfm)
	Wave wfm
	Variable i,n=numpnts(wfm), massTimesX=0
```

```
	for(i=0; i<n; i+=1)
		massTimesX += wfm[i]*pnt2x(wfm,i)
	endfor
	Variable totalMass=sum(wfm)
	Variable centerOfMass= massTimesX/totalMass
	printf "Center of Mass: %g", centerofMass
return centerOfMass
End

//////////////////////////////Mean square error//////////////////////
Function WSFIe(bw, tw, xl, xr)
	wave bw, tw
	variable xl, xr
	variable WSFIvalue
	duplicate/R=(xl, xr)/FREE bw, rw, bdw
	duplicate/R=(xl, xr)/FREE tw, tdw
	rw = (bdw - tdw)^2 / numpnts(bdw)
	WSFIvalue = sum(rw)
	 print "N=",numpnts(bdw), "WSFI=", WSFIvalue, rw
return WSFIvalue
end


Function SmoothAll()
	String list = TraceNameList("", ";", 1)
	String traceName
	Variable index = 0
	do
		traceName = StringFromList(index, list)
		if (strlen(traceName) == 0)
		break // No more traces.
		endif
		 SmoothAllFn(tracename)
		index += 1
	while(1)
end


////////////////32-point-data to 400-point-data conversion//////////////////
Function SmoothAllFn(tracename)
	String tracename
	WAVE w = TraceNameToWaveRef("", traceName)
	String outputName= NameofWave(w)+"s"
	duplicate/O w, $outputName
	Interpolate2/T=2/N=400/E=2/Y=$outputName w
	Appendtograph $outputName
	doupdate
	End
```

Appendix B

Spectral baseline line (without light source):

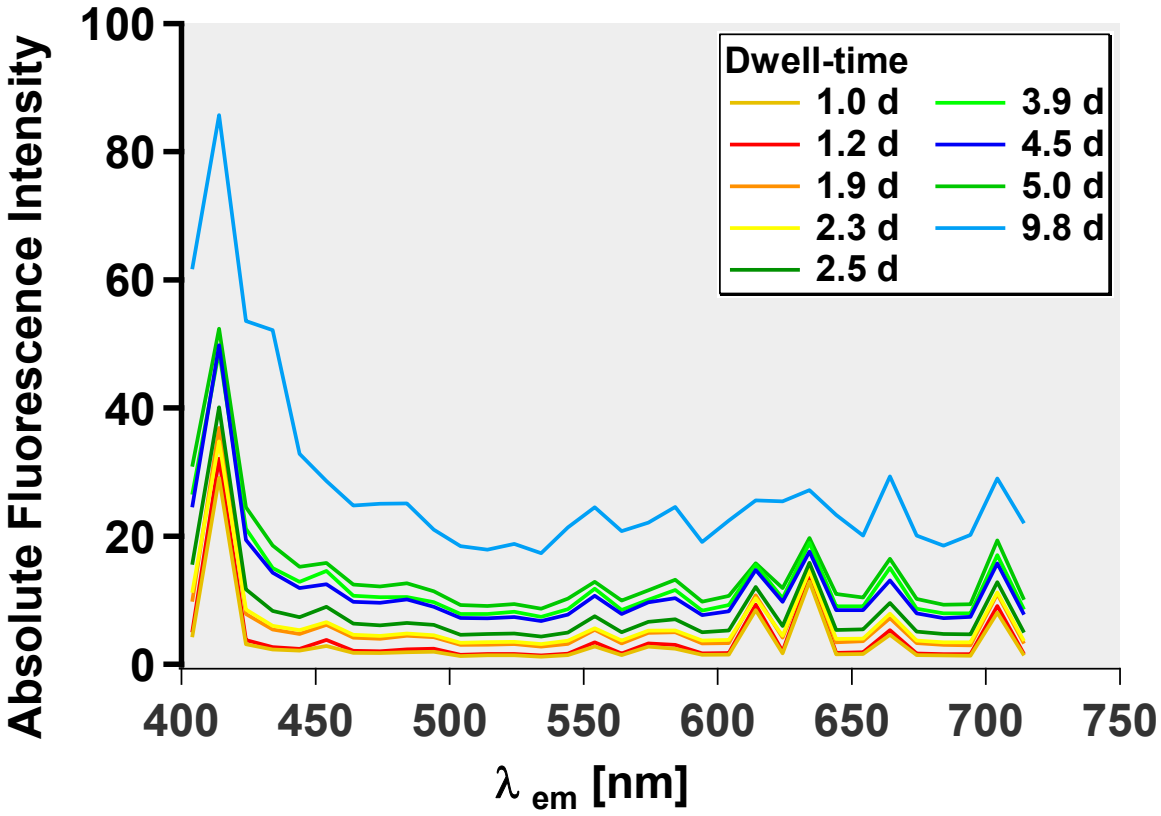

The parameter of dwell-time was used to study the baseline of spectral detector.

Appendix C

NRSSA summary of myelin samples

Population	Maximum Peak	Range (NF> 0.1)	Total size	Center of Mass	Mean Square Error	N (animal)
Total myelin fraction	37	21-56	35.7±0.2	38.3	N/A	5
Crude cholesterol	33	18-56	51.5±0.3	35.8	0.06 (20-56)	5
Crude lecithin	48	31-87	63.1±0.3	54.6	0.2 (20-56)	5
Myelin *in situ*	33.7	26-40	19.7±0.2	33.6	N/A	5
Delipidation (myelin *in situ*)	47	40-50	13.4±0.2	45.8	0.3(26-50)	3
Solubilized membrane protein	51	47-55	11.5±0.2	50.8	0.25 (26-55)	3
PLP-null	37	33-44	14.7±0.2	37.5	0.08 (26-44)	2
P_0-CNS	35	30-42	17.9±0.2	35.5	0.2 (26-44)	3
Cytoplasm (DC)	52	43-59	24.0±0.2	51.6	0.3(26-59)	5
P5	45	40-51	18.7±0.2	46.0	0.38(27-51)	2
P10	37	30-43	20.5±0.2	37.3	0.18(27-43)	2
P430	26	18- 38	28.6±0.2	27.7	0.22 (18-40)	2
Lipid droplets (M03.13)	30	23-39	23.5±0.2	31.6	0.12(23-40)	N/A
Lipid droplets (mOPC)	25	19-31	16.8±0.2	26.0	0.29(19-40)	N/A
Live myelin	41	33-50	28.3±0.3	41.5	N/A	3
T = 0 h	38	31-45	22.2±0.2	38.2	0.13(33-50)	3
T = 1 h	40	33-48	24.5±0.2	40.4	0.015(33-50)	3
T = 2 h	40	32-48	24.6±0.2	40.1	0.024(33-50)	3
T = 3 h	41	34-47	20.6±0.2	40.8	0.025(33-50)	3
T = 4 h	42	34-47	21.7±0.2	41.8	0.019(33-50)	3
T = 5 h	44	36-51	24.7±0.2	44.1	0.09(33-50)	3
T = 6 h	43	33-53	31.1±0.3	43.1	0.03 (33-50)	3
T = 8 h	43	33-52	29.7±0.3	42.6	0.02(33-50)	3
Lipid oxidation	37	27-47	28±0.2	37.4	0.26(27-50)	3
DC WM (slide)	33	25-42	26.2±0.2	33.2	0.02(26-47)	3
DC GM (slide)	40	30-47	27.3±0.2	38.5	0.21 (26-47)	3
Lipid-laden macrophages (DC WM slide)	28	19-33	21.3±0.2	26.8	0.3 (19-40)	3
Sham (DC WM slide)	33	25-41	26.2±0.2	33.2	N/A	3
Lesion day 5 (slide)	26	19-40	34.0±0.3	29.4	0.13(19-41)	3
Lesion day 28 (slide)	34	14-37	18.6±0.2	29.4	0.06(25-41)	3
NAWM day 5* (slide)	35	30-42	18.6±0.3	35.4	0.11(25-41)	3

Population	**Maximum Peak**	**Range (NF> 0.1)**	**Total size**	**Center of mass**	**Mean Square error**	N
NAWM day 28 (slide)	34	28-39	17.0±0.2	33.5	0.05(25-41)	3
LPC solvent	87	83-91	11.7±0.2	87.3	N/A	N/A
PBS sham	38	25-45	31.1±0.2	36	0 (25-45)	2
LPC day 3 (abnormality A)	30	17-41	28.3±0.2	29.5	0.22(17-45)	2
LPC day3 (abnormality B)	19	10-26	24.2±0.2	19.0	0.35(10-45)	2
LPC day 3 (abnormality C)	16	4-28	31.8±0.2	15.5	0.30(4-45)	2
Lipid-laden macrophages (LPC day 3)	14	4-25	31.4±0.2	15.1	0.32(4-45)	2
Remyelination (LPC day 36)	50	36-62	38.6±0.3	50.0	0.33(25-62)	2
Human myelin	42	35-50	22.2±0.2	42.3	N/A	1
DAWM	29	22-35	19±0.2	28.7	0.34(21-50)	1
NAWM*	28	6-35	52.6±0.3	21.5	0.42(6-50)	1
Rim lesions	28	21-35	20.3±0.3	28.1	0.23(35-50)	1
Focal lesions*	28	18-44	40.8±0.3	30.6	0.35(21-50)	1

*Bimodal histogram, NF = Normalized Frequency